University of Nebraska - Lincoln
DigitalCommons@University of Nebraska - Lincoln

Civil Engineering Theses, Dissertations, and Student Research

Civil Engineering

7-2011

Using Laser Scanning Cytometry to Investigate the Transport of Nano-Scale Particles in Porous Media

Ryan May
University of Nebraska – Lincoln, ryan.may@huskers.unl.edu

Follow this and additional works at: http://digitalcommons.unl.edu/civilengdiss

Part of the Civil Engineering Commons, and the Environmental Engineering Commons

May, Ryan, "Using Laser Scanning Cytometry to Investigate the Transport of Nano-Scale Particles in Porous Media" (2011). *Civil Engineering Theses, Dissertations, and Student Research*. 27.
http://digitalcommons.unl.edu/civilengdiss/27

This Article is brought to you for free and open access by the Civil Engineering at DigitalCommons@University of Nebraska - Lincoln. It has been accepted for inclusion in Civil Engineering Theses, Dissertations, and Student Research by an authorized administrator of DigitalCommons@University of Nebraska - Lincoln.

USING LASER SCANNING CYTOMETRY TO INVESTIGATE THE TRANSPORT OF NANO-SCALE PARTICLES IN POROUS MEDIA

By

Ryan May

A THESIS

Presented to the Faculty of
The Graduate College at the University of Nebraska
In Partial Fulfillment of the Requirements
For the Degree of Master Of Science

Major: Civil Engineering

Under the Supervision of Professor Yusong Li

Lincoln, Nebraska

July 2011

USING LASER SCANNING CYTOMETRY TO INVESTIGATE THE TRANSPORT OF NANO-SCALE PARTICLES IN POROUS MEDIA

Ryan May, M.S.

University of Nebraska, 2011

Advisor: Yusong Li

The increased production of nanomaterials in recent years has been unprecedented. Given their potential toxicity, understanding the mechanisms controlling the transport of nanoparticles in the subsurface is important. In this study, a technique was developed for using a Laser Scanning Cytometer (LSC) to visualize and quantify the stable attachment of nano-scale particles. Experiments using three different size particles, 510 nm, 210 nm and 57 nm, in conjunction with a flow cell system containing saturated glass beads under varied injection duration, solution chemistry, Darcy velocity and solids content were performed. A technique for using the LSC data to develop spatial distributions of attached particles was developed. The ability to provide quantifiable data and a spatial distribution of nanoparticle attachment at the pore-scale is unique and provides direct insight into the fundamental mechanisms governing nanoparticle transport.

The experimental results show attachment decreases with decreasing particle size. The increase in injection duration for the 510 nm particles indicates a likely maximum retention capacity (S_{max}). Blocking effects are observed for the 57 nm particles in which attached particles block the available attachment sites and slow the rate of attachment.

Secondary minimum attachment plays a minor role for the attachment of both the 510 nm and 57 nm particles and is independent of particle size. Only about 10% of the attachment is attributed to secondary minimum attachment. Change of Darcy velocity has no profound influence on the attachment of the 57 nm particles indicating diffusion-dominated attachment. Diffusion control is further confirmed by the spatial distributions of attached 57 nm particles showing attaching on downstream glass bead areas. Investigations of initial solids content reveal the importance of particle (aqueous) - particle (attached) interactions. For the 510 nm and 210 nm particles, there exists a critical initial solids content above which the attachment decreases with increasing initial solids content. This trend does not occur for the 57 nm particles which exhibit increasing attachment with increasing solids content due to much weaker repulsive interaction energy.

Acknowledgment

I would like to express my very sincere appreciation and gratitude to my advisor, Dr. Yusong Li, Assistant Professor of Civil Engineering, for her assistance, guidance, encouragement and patience during the process of this study.

Sincere thanks are also due to my committee members, Dr. David Admiraal and Dr. Xu Li, for their support.

Thanks also to Dr. Maciej Skotak and Dr. Raffet Velarde as well as the Biomechanics, Biomaterials and Biomedicine Instrumentation Facility (BM^3) for their support and facility use.

I would also like to thank my fellow research group members Chunmei Bai and Megan Seymour for their help and support.

Table of Contents

List of Figures

List of Tables

Notation

Symbol/Variable	Description
LSC	Laser Scanning Cytometer
η_0	Single collector efficiency
α	Attachment efficiency factor
DLVO	Derjaguin-Landau-Verwey-Overbeek
S_{max}	Maximum retention capacity
k_{att}	Attachment rate
NOM	Natural organic matter
MWNT	Multi-walled nanotube
SWNT	Single-walled nanotube
DLS	Dynamic Light Scattering
PCS	Photon Correlation Spectroscopy
QLES	Quasi-elastically Scatter Light
PALS	Phase Analysis Light Scattering
ELS	Electrophoretic light scattering
EPM	Electrophoretic mobility
PV	Pore volume
PMT	Photomultiplier tube

Chapter 1

Introduction

1.1 Project Overview

The increased production and widespread application of nanomaterials in recent years has been unprecedented. This has inevitably led to the release of nanoparticles into the environment. Given their potential toxicity, understanding the fate and transport of nanoparticles in the natural environment is important. Little is currently known about the fate and transport of nanoparticles in the subsurface environment; thus, research on the fundamental mechanisms governing the transport of nanoparticles in the subsurface is necessary. The foundation of such research is investigating the physical and chemical factors controlling their transport at various scales.

The common approach to investigate the fate and transport of nanoparticles in porous media is through column-scale experiments. In these experiments, nanoparticle suspensions are pumped into glass columns (typically 10 cm long and 3 cm in diameter) packed with glass beads or Ottawa sand for a specific time period. Typically, this is followed by pumping a nanoparticle-free background solution through the column. The nanoparticle concentration in the effluent is usually monitored to generate effluent breakthrough curves. Following the completion of the experiment, the column may be segmented and a method for measuring the average concentration of nanoparticles in each section may be used. Column experiments have been used to investigate the influences of several factors, including ionic strength, electrolyte concentration and composition, flow velocity, grain surface roughness and particle sizes, on the mobility of engineered nanoparticles in porous media.

The column experiments provided invaluable information on nanoparticle transport and mobility; however, such research has some limitations. The biggest limitation of column experiments is the inability to make direct observations of the mechanisms governing the transport of nanoparticles. Average concentrations of retained nanoparticles within each column section can be measured following the completion of the experiment, but the actual spatial distribution of the attached nanoparticles and direct observation of the attachment relative to collector surfaces are unattainable at the column-scale. Thus, only inferences can be made about the mechanisms controlling the transport.

A more mechanistic approach to investigate the transport and retention of nanoparticles in the subsurface is through the utilization of micromodels to directly observe attachment at the pore-scale. This technique involves the injection of nanoparticle suspensions into a flow cell under a microscope operating in conjunction with an image capturing device. Microscope-based imagining devices may then be used to directly observe the transport and attachment of nanoparticles to collector surfaces. Some techniques may also be used to quantify and record the attachment.

Pore-scale experiments do provide a way to directly observe and visualize the transport and retention of nanoparticles, but such experiments have limitations. The first is the resolution restriction which may preclude application to nano-scale particles. Widely-used visualization techniques, such as visible light imaging, magnetic resonance imaging and synchrotron x-ray tomography, work best at the micro-scale. A second limitation of pore-scale experiments is the capability to obtain data that is quantifiable. In order to achieve high resolution, most available visualization techniques are only able to focus on a very small area (a single pore space several microns in length). Considering the high uncertainty and complexity of porous media, several high resolution pictures in several pore spaces can typically only provide some qualitative information. Techniques with applications beyond just visualization are novel. Quantitative data such as the number of attached particles allows researchers the opportunity to mathematically model the results. If such pore-scale models are validated, insight into the fundamental mechanisms governing nanoparticle transport may be revealed.

One pore-scale experimental technique involves using Laser Scanning Cytometry. Laser Scanning Cytometry uses laser-based opto-electronics and automated analysis capabilities to visualize, quantify and record fluorescent matter. The Laser Scanning Cytometer (LSC) is a micro-scope based instrument that incorporates fluorescent microscopy, image analysis and flow cytometry technologies. The advantages of using the LSC is the ability to observe a large scan area (up to several centimeters), quantifiable data is obtained, a spatial distribution of particles is generated and the pore-scale provides direct insight on the mechanisms governing transport. It is reasonable to assume this technique will allow researchers the ability to work with nanoparticles smaller than 100 nm and obtained quantitative information on their attachment and distribution in porous media. An LSC-based technique such as this has not been used before. This study represents the first use of Laser Scanning Cytometry to investigate nanoparticle transport and retention.

1.2 Project Goals and Objectives

The main purpose of this study is to explore the feasibility of using an LSC to investigate the transport of nano-scale particles in porous media. This study is oriented by two specific goals:

1. Develop an LSC-based technique to visualize and quantify the transport of nano-scale particles in a flow cell system.
2. Use the developed technique to investigate the mechanisms controlling the transport and retention of particles of different sizes in glass bead porous media under varied injection duration, solution chemistry, Darcy velocity and solids content.

Chapter 2

Literature Review

2.1 Introduction

In this chapter, literature on the production and environmental impact of nanoparticles, the fundamental mechanisms governing nanoparticle transport in the subsurface, previous experiments and Laser Scanning Cytometry is discussed.

2.2 Engineered Nanomaterials

2.2.1 Engineered nanomaterial production

Engineered nanomaterials are referred to as manufactured materials that have at least one dimension less than 100 nm. The *EPA Nanotechnology White Paper* further defines nanotechnology as, "…research and technology development at the atomic, molecular, or macromolecular levels using a length scale of approximately one to one hundred nanometers in any dimension; the creation and use of structures, devices and systems that have novel properties and functions because of their small size; and the ability to control or manipulate matter on an atomic scale." Figure 2.1 illustrates the scale of several nano-scale objects [1].

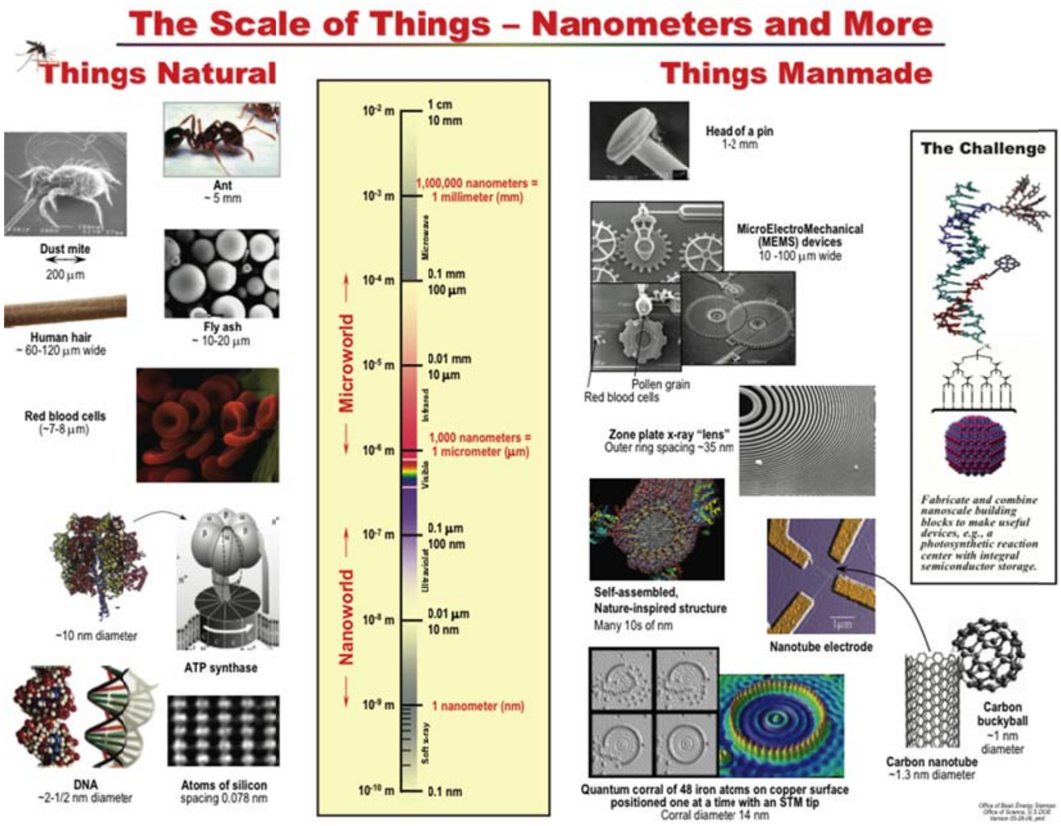

Figure 2.1 Diagram depicting relative scale of several nano-scale objects [1]

Nanomaterials often possess unique and enhanced properties compared to similar larger-scale materials. Possessing distinct electronic, photoactive, thermal and optical properties has resulted in the application of nanomaterials in various industries. An example is the use of nanomaterials in the transportation industry to produce lightweight materials without sacrificing the strength of the material. A few other examples of nanotechnology applications are smart roofs, solid-state lighting and fuel additives. The unique properties of nanomaterials also lead to appealing environmental applications. Large surface area to mass ratios and enhanced reactivity are just two of the properties of nanomaterials making it beneficial to use them for remediation. Environmental remediation and nanosensors to detect contaminants are two examples.

The revenue projections for nanotechnology-enabled products are expected to reach $25 billion in 2015 [2]. To date, it has been reported that more than 1,300 manufacturer-identified nanotechnology-enabled consumer products have been introduced in the marketplace [3].

2.2.2 Environmental impact of nanoparticles

Because the environment is exposed to intentionally produced nanomaterials, it is important for research to investigate likely exposure pathways. Environmental fate of nanomaterials includes fate in air, soil and water. Given the various uses of nanomaterials, it is clear there are several pathways for nanomaterials to enter the environment besides direct application. A few examples of how engineered nanomaterials may enter the subsurface environment are industrial releases, directly leaching from landfills, wastewater reuse, biosolids containing engineered nanomaterials used in agriculture and recharge of groundwater from a water source containing engineered nanomaterials. Figure 2.2 depicts several of these exposure pathways. It has been shown that silver nanoparticles, currently the most commonly used engineered nanomaterials in consumer products [4], can be released from cloth, toothpaste, shampoo, detergent, towel and toys during washing processes [5, 6, 7]. Direct evidence [8] has shown that synthetic TiO_2 nanoparticles from urban applications are released in significant amounts to the aquatic environment.

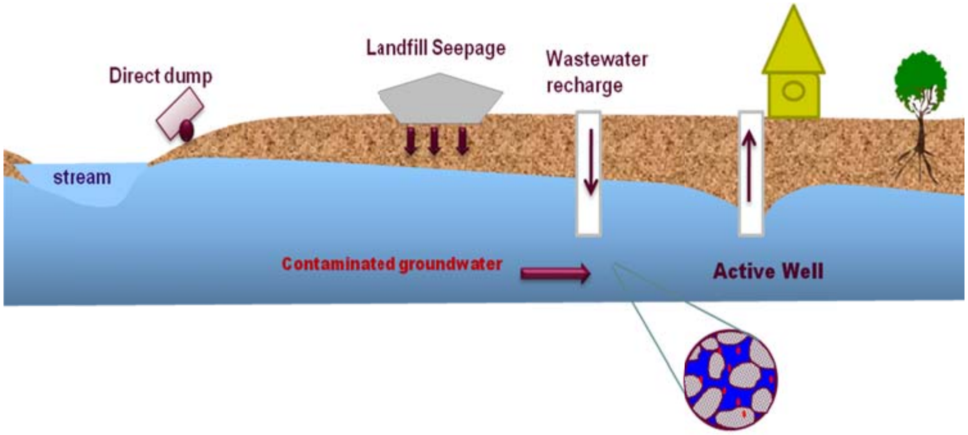

Figure 2.2 Exposure pathways for engineered nanomaterials to reach the subsurface

After entering the environment, the fate and transport of nanoparticles is dependent on the properties of the nanoparticles themselves as well as the surrounding environment. The size, shape and surface characteristics of nanoparticles influence their fate in the natural environment. Once nanoparticles have entered the subsurface, several environmental characteristics such as the solution chemistry (pH, ionic strength, etc.) and hydrodynamics (flow velocity, turbidity, etc.) impact their behavior. Studies have shown engineered nanomaterials may interact with natural organic matter (NOM) and undergo surface transformation resulting in very stable aggregates which are capable of traveling extreme distances with the potential to reach drinking water resources. Consequently, it is extremely important to understand the fate and transport of engineered nanomaterials in the subsurface.

Several studies have shown potential human health effects, aquatic toxicity and antimicrobial properties of engineered nanomaterials [9]. The release of Ag+ from nano-silver may increase its potential toxicity [10]. A recent study found that exposure to nano-silver between 5 and 46 nm resulted in increased mortality, heart malformation and other developmental deformities in zebrafish at concentrations as low as 5 μg/mL [11]. 50,400 tons of TiO_2 was produced in 2010 and that number is projected to increase to 201,500 tons by 2015 [12]. TiO_2 has been reported to cause oxidative stress in microglial cells [13], inflammation in rats and mice [14], cytotoxicity and genomic instability towards cultured WIL2-NS human lymphoblastoid cells [15] and DNA damage to goldfish skin cells, GFSk-S1 [16]. It has also been reported that a typical water treatment process, coagulation followed by sedimentation at an alum dosage of 60 mg/L, removed less than 40% of the influent TiO_2 nanomaterials, which are widely used in sunscreen [17].

Clearly, with wide-spread production and inevitable exposure of nanoparticles to the environment, specifically the subsurface, it is important that extensive research on nanoparticles be performed to investigate potential exposure pathways, fate and transport, environmental impacts and risk assessment. The focus of this study falls into the fate and transport aspect of nanoparticle research focusing on the influence of several environmental conditions and nanoparticle properties on particle attachment at the pore-scale.

2.3 Understanding Fate and Transport of Nanoparticles

2.3.1 Theories for nanoparticle transport and retention

Particle transport is influenced by many physical and chemical processes. The mechanisms contributing to the fate and transport of particles in the subsurface are advection, dispersion, physicochemical filtration, straining, inactivation and dilution. Advection is the movement of the nanoparticles along the fluid flow paths within the porous media. The process of advection leads to dispersion of the particles due to tortuosity and non-homogeneity of the fluid flow paths. Physical mechanisms also play a significant role in the transport of particles. The physical mechanisms influencing the attachment of particles include physicochemical filtration and straining. Straining is the trapping of particles in pore throats too small to allow their passage. Physicochemcial filtration, depicted in Figure 2.3, involves three main mechanisms: interception, Brownian diffusion and gravitational sedimentation. Brownian diffusion is expected to play a significant role in the transport of nanoparticles in the subsurface due to their high diffusivity resulting in frequent collisions with collector surfaces.

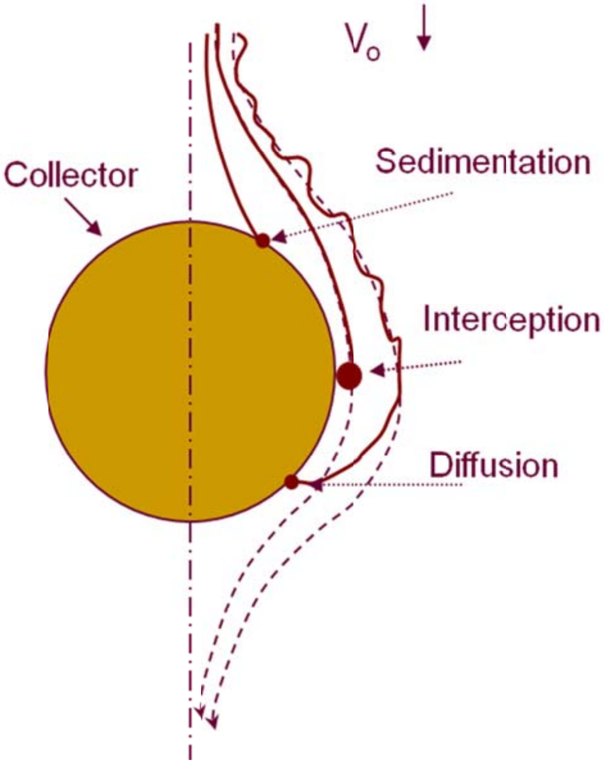

Figure 2.3 Physicochemical filtration removal mechanisms

Clean-bed filtration theory [18] has been most often used to model nanoparticle transport. The removal rate of particles is expressed in terms of a single collector efficiency (η_0) and attachment efficiency factor (α). The first step is the transport of particles to the vicinity of the collector surface which is controlled by physical factors including flow velocity, porosity and surface area. The frequency of collisions between particles and collectors is represented by η_0 and is used to describe this step. η_0 is typically calculated by correlations reflecting interception, sedimentation, diffusion and van der Waals interaction processes. Figure 2.4 illustrates the relative importance of these processes for particles with sizes ranged from 1 nm to 100 μm.

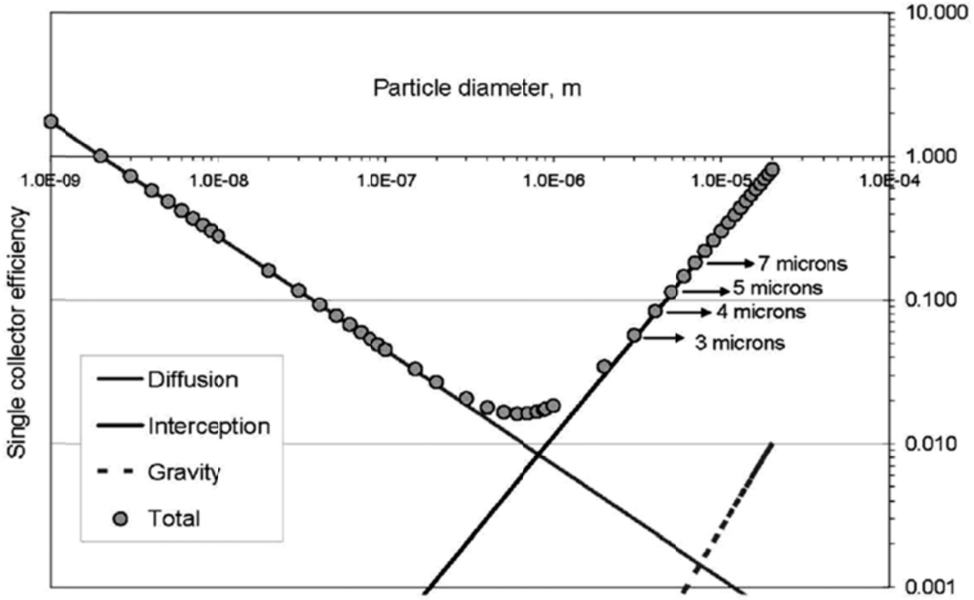

Figure 2.4 Single-collector efficiencies as a function of colloid size [9]

The second step is the attachment of the particle to the collector surface which is controlled by chemical factors including ionic strength and electrolyte types. This step is described by α, defined as the fraction of collisions resulting in attachment. Currently there is no reliable way to predict α. However, Derjaguin-Landau-Verwey-Overbeek (DLVO) [20] theory is typically used to help analyze the interaction energy between particles and sand surfaces.

DLVO theory states that the interactions between a colloidal particle and a collector surface can be expressed as the sum of the attractive van der Waals and electrostatic double layer interactions. These interactions can be either attractive or repulsive. When the particle and porous medium surfaces are like-charged, the electrostatic double layer force is repulsive and a typical DLVO energy profile is characterized by a deep attractive well (the primary minimum) at a small separation distance, a maximum energy barrier and a shallow attractive well (the secondary minimum) at a larger distance. An example energy profile is illustrated in Figure. 2.5.

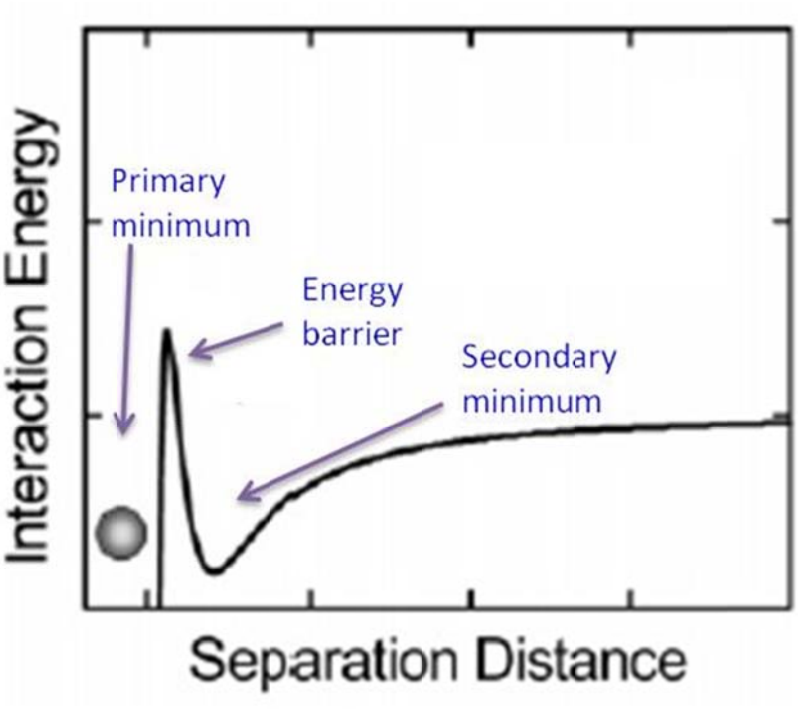

Figure 2.5 Example energy profile

Li et al. [21] analyzed the accuracy of modeling nC_{60} transport and retention in water-saturated quartz sand using classic filtration theory. The classic filtration model breakthrough curves and retention profiles failed to reproduce the measured experimental results. This finding brings into question whether α values calculated using classic filtration theory accurately represent nC_{60} attachment efficiency. Classic filtration theory assumes attachment depends only on aqueous phase aggregate concentration and is a first-order kinetic possess. Li et al. [21] suggest the rate of attachment depends on the retained particle concentration and there exists a maximum retention capacity (S_{max}). Li et al. [21] produced a modified model with the attachment rate (k_{att}) linearly dependent on the fraction of surface area available for attachment. As more particles are deposited, the available surface area decreases resulting in decreased k_{att}. As k_{att} approaches zero, the solid-phase concentration of nC_{60} aggregates approaches S_{max}. This modified model suggests α will actually decrease with time. Li at al. [21] were able to much more accurately simulate the nC_{60} breakthrough curves and retention profiles using the modified model.

2.3.2 Column-scale studies

The traditional laboratory method for investigating the fate and transport of nanoparticles in porous media is column experiments. In these experiments, nanoparticle suspensions are pumped into glass columns (typically 10 cm long and 3 cm in diameter) packed with glass beads or Ottawa sand for a specific time period. This is typically followed by pumping a background solution free of nanoparticles, often called a rinse. Nanoparticle concentration in the effluent is generally monitored to generate effluent breakthrough curves. Following the completion of the experiment, the column may be segmented and some average concentration for each section may be measured. Column experiments have been used to investigate the influences of different factors, such as ionic strength, electrolyte concentration and composition, flow velocity, grain surface roughness and particle sizes, on the mobility of engineered nanoparticles in porous media. In the following paragraph, a brief summary of some representative studies is provided.

Ionic strength has been investigated to determine its influence on particle attachment. As ionic strength increases, α has been found to increase resulting in an increase in attachment as a result of a decrease in electrostatic repulsion between particles

[22]. Several studies have shown that as ionic strength increases, α increases resulting in an increase in attachment [23, 24, 25]. This decrease in electrostatic repulsion between particles results in increased particle aggregation which in turn leads to greater attachment. Espinasse et al. [22] found that the theoretical limit for α was reached at the highest experimental ionic strength. Hyung and Kim [23] studied the effect of NOM adsorption to multi-walled nanotubes (MWNTs) and found that the adsorption capacity was affected by ionic strength as well as pH. Adsorption capacity increased as ionic strength increased and adsorption capacity decreased as pH increased. Jaisi and Elimelech [24] studied the transport of single-walled nanotubes (SWNTs) in soil columns and found that SWNT attachment increased due to physical straining with increasing ionic strength.

Electrolyte concentration and composition is another chemical factor influencing particle attachment in the subsurface. Increasing multivalent cation concentration has been found to increase the retention of fullerene aggregates on glass bead surfaces [22]. Jaisi and Elimelech [24] found that SWNT attachment in soil columns increased due to physical straining with the addition of cations. They also found that divalent cations (Ca^{2+}) are more effective than monovalent cations.

Flow velocity is a physical factor that has been found to influence the retention of nanoparticles in porous media. Physical factors tend to influence the collector efficiency, or the rate at which particles strike the collector per the rate at which particles flow toward the collector. Diffusion will be the dominant retention mechanism. At higher flow velocities, less diffusion occurs resulting in lower η_0. Consistent with the theory, experimentally estimated α values have been found to be independent of flow rate [22]. Thus, higher flow velocities have been shown to result in less retention [22, 21, 25].

Micro-scale surface heterogeneity such as surface roughness of porous media may also impact particle attachment. For example, Li et al. [21] found the S_{max} of nC_{60} is influenced by pore-scale hydrodynamics, which would certainly be impacted by sand surface roughness which could alter streamlines around the sand grain and increase nC_{60} retention. Also, increased grain size resulting in greater porosity has been found to decrease retention [21, 22]. Varying transport and retention characteristics have been reported for nC_{60} transport depending on whether glass beads, quartz sands, or natural soils represent the porous medium. Wang at al. [27] found the retention of nC_{60} in columns packed with glass beads is significantly smaller than with quartz sands and natural soils. More recently, Li et al. [21] found that the retention capacity of nC_{60} on natural soils could be 10 times higher than on Ottawa sand.

The effect of particle size on the attachment of nano- and micro-scale latex particles in porous media has been studied [28]. Particles having diameters of 50 nm, 110 nm and 1500 nm were used. The results showed the smallest of the three particle diameters exhibited the least retention over the range of ionic strengths used. The two larger particle diameters showed much higher retention on the sand surface. It was shown that the attachment efficiencies for the particles with a diameter of 500 nm were significantly greater than those of the smaller particles at low ionic strengths. This is not in agreement with expectation. One explanation may be the larger diameter particles are able to deposit in the secondary minimum.

While column-scale studies have provided invaluable information on nanoparticle transport and mobility, such an approach has some limitations. The most important limitation of column experiments is the inability to make direct observations of the mechanisms governing the transport of nanoparticles. A researcher may be able to measure the average concentration of retained nanoparticles within an individual section of the column at the end of the experiment, but the physical distribution of the attached nanoparticles within the segment and direct observation of the attachment relative to collector surfaces are not possible. Thus, it is difficult to clearly elucidate which mechanisms are controlling the transport.

2.3.3 Pore-scale studies

Traditionally, research investigating the transport of nanoparticles in the subsurface has been performed using column-scale studies. The limitation with using a column-scale approach is that inferences must be made about the mechanisms controlling the transport based on the average concentration of the effluent. A more mechanistic approach to investigate the transport of nanoparticles in the subsurface is through the utilization of micromodels to directly observe particle attachment at the pore-scale.

One micromodel study [19] used monodisperse suspensions of spherical polystyrene latex particles with a mean diameter between 3 and 7 μm in micromodels to investigate the importance of different processes involved in the removal of colloids in porous media under saturated conditions. The study examined the effect of particle size, grain surface roughness, solution ionic strength and flow rate on colloid attachment. The colloids had a sulfate (SO_4^-) surface functionalization and a negatively charged surface.

Ionic strength was controlled by adjusting KCl concentration. The physical micromodels contained homogenous pore networks with either rough or smooth collector surfaces as shown in Figure 2.6. The researchers found that the results were in agreement with classic filtration theory for throat to colloid ratios great than 2.5; however, for smaller ratios, straining was an important removal mechanism and is not taken into account by classic filtration theory. The results also showed increased attachment for both increased ionic strength as well as decreased flow rate, in agreement with expectation. Experiments investigating the effect of increased surface roughness indicated that collision efficiency increased. This study shows that surface roughness and physical straining, not taken into account by classic filtration theory, are both important removal mechanisms for nanoparticle transport.

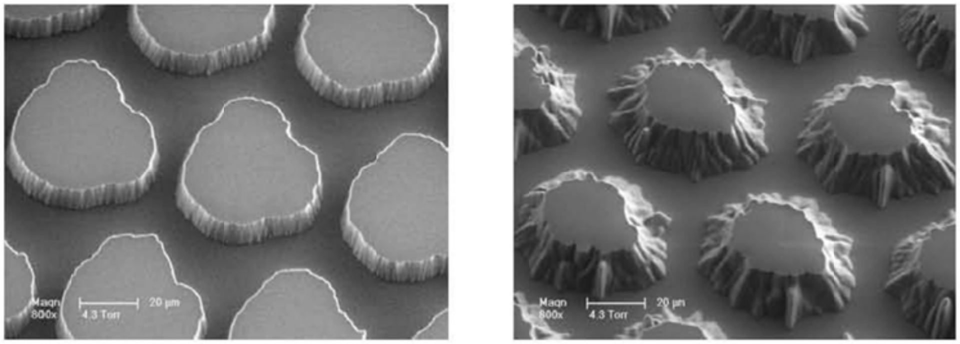

Figure 2.6 Images of the micromodels: relatively smooth grain surfaces (left) and notably rough grain surfaces (right) [19]

The secondary energy minimum has also been investigated to determine its role in particle attachment [29]. The researchers performed flow cell experiments in which a single layer of glass beads was packed into a horizontal flow cell and micro-scale particles were injected. A fluorescent microscope with phase contrast capabilities was used to visualize the attachment. The results showed no attachment occurred at low ionic strengths. At moderate ionic strengths (10-30 mM) achieved using monovalent salt, particle attachment was found to occur in the secondary minimum and accumulation near the rear of the collectors was observed. An ionic strength of 100 mM resulted in attachment over the entire collector surface. This is attributed to no calculated electrostatic energy barrier existing at this high ionic strength. The authors concluded that attachment of micron-scale particles in the secondary energy minimum is an important removal mechanism.

Surface potential has also been shown to influence aggregation and transport of nanoparticles [30]. The study investigated the effect of surface potential on Titania particle aggregation and transport in Pyrex wafer micromodels by adjusting the pH. The results indicated that pH, and therefore surface potential, greatly influenced aggregation, particle-particle interactions and particle-collector interactions.

While pore-scale experiments provide means to directly observe and visualize the transport and retention of particles, there are several limitations. The first is the resolution restriction, which may preclude its application to nano-scale particles. Visualization techniques currently used in pore-scale experiments include visible light, magnetic resonance and X-rays. The corresponding resolution limits for each one are presented in Table 2.1. Clearly, none of these techniques is able to identify particles smaller than 100 nm. A second limitation of pore-scale experiments is the capability to obtain quantitative information in addition to visualization results. Only if quantitative information, such as the number of particles attached, is obtainable from pore-scale experiments, can rigorous modeling and prediction be implemented and validated at the pore-scale to reveal the mechanisms governing nanoparticle attachment and retention.

Table 2.1 Visualization techniques and corresponding resolution limits

Technique	**Resolution Limit**
Visible light imagining	20 μm
Visible light imagining (microscopy)	0.2 μm
Magnetic resonance imagining	10 μm
Synchrotron X-ray tomography	3 μm
γ-ray tomography	mm
Positron emission tomography	?

2.4 Laser Scanning Cytometry

Laser Scanning Cytometry uses laser-based opto-electronics and automated analysis capabilities to visualize, quantify and record fluorescent matter. The LSC is a micro-scope based instrument that incorporates fluorescent microscopy, image analysis and flow cytometry technologies. The advantages of using an LSC are the ability to observe a large scan area (up to several centimeters), quantifiable data is obtainable, a spatial distribution of particles is generated and investigation at the pore-scale provides direct insight on the mechanisms governing transport.

The LSC measures laser excited fluorescence at several wavelengths from fluorescently dyed matter on standard microscope slides. The LSC has two lasers, a 20 mW argon ion laser and a 5 mW red HeNe laser, and each provides a single wavelength to excite fluorescently dyed samples. The fluorescent light given off by the dyed samples is collected and transmitted to up to four photomultiplier tube (PMT) detectors. Each PMT detector measures a different range of wavelengths.

A schematic of the major components within the LSC is provided in Figure 2.7. The following technical description of the process by which the LSC operates was published by Kamentsky et al. [31]:

> The beams from an argon ion and a helium-neon laser are combined at a dichronic mirror and steered to a second dichronic mirror designed to reflect the laser wavelengths and to transmit other wavelengths…The combined beam is steered toward a computer-controlled scanning mirror, producing a saw tooth motion at a nominal rate of 350 Hz and creating a line scan at the microscope slide. After passing through a scan lens, the beam enters the epi-illumination port of a standard Olympus BX50 microscope and is imaged by the objective lens onto the focal plane at the specimen…Fluorescent energy is collected by the objective, reflected by a partially silvered mirror…and steered through the scan lens and to the scanning mirror. It then passes through a series of dichronic mirrors and optical interference filters to up to four photomultipliers, each detecting a specific fluorescent wavelength range.

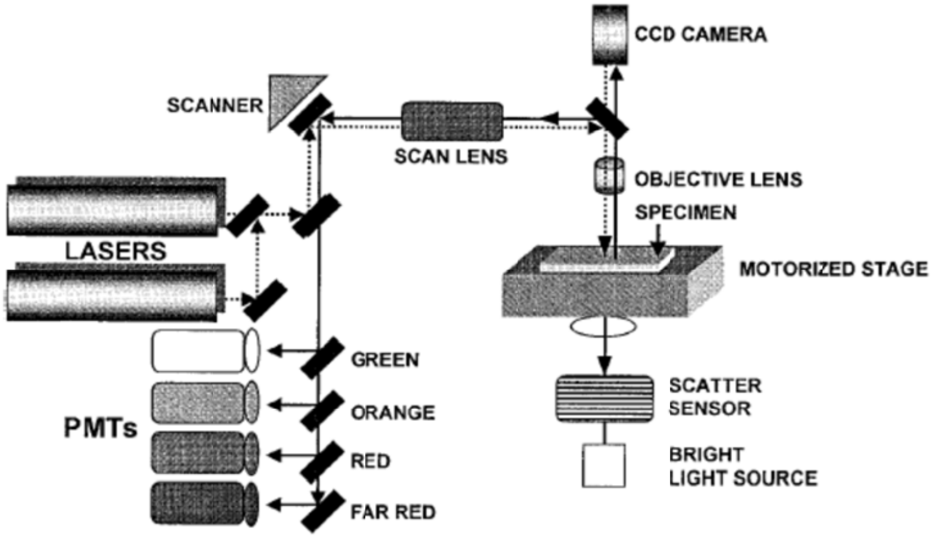

Figure 2.7 Schematic of the Laser Scanning Cytometer components [32]

Laser Scanning Cytometry has several advantages. Multiple channels of information are simultaneously visualized and analyzed. The LSC allows users to automatically segment samples of interest. Further, the LSC has the capability to segment on the sub-cellular level. Several application types are capable of implementation using LSC technology. According to CompuCyte [33], fluorescent molecules in solution, nuclear analysis, cytoplasmic analysis, cellular analysis and colony analysis are just a few of the typical applications of LSC-based studies.

Based on these features of the LSC, it is reasonable to hypothesize that utilizing it will allow for (1) identification of nanoparticles with sizes less than 100 nm and (2) obtaining of quantitative information on nanoparticle attachment and distribution in porous media. At this point in time, an LSC has not been used to investigate fate and transport of nanoparticles in porous media. This study represents the first LSC-based approach for investigating the transport and retention of nanoparticles.

Chapter 3

Experimental Equipment Design

3.1 Introduction

One of the major objectives of this study is to design a procedure for using Laser Scanning Cytometry to visualize, quantify and record the transport of nanoparticles in saturated glass bead porous media. Fluorescent particles and a flow cell system need to be appropriately selected and designed in order to allow for the observation of the transport of nanoparticles using fluorescent microscopy equipped with an LSC. This chapter details the selection and characterization of the particles and the design of the flow cell system.

Fluorescent particle selection was dependent on the characteristics of the LSC. More specifically, the excitation wavelength of the laser and the emission wavelengths of the PMT detectors governed the selection of the fluorescent particles. Fluorescent particles with an excitation spectrum peak near the wavelength provided by the laser and an emission spectrum peak within the wavelengths covered by one of the available PMT detectors were selected based on manufacturer supplied excitation and emission spectra. In order to verify the compatibility of the fluorescent particles with the LSC, exploratory LSC scans were performed during the particle selection process. Also, a procedure for preparing particle suspensions was developed.

Characterizations of the particle suspensions were performed through particle size distribution and zeta potential measurements. Particle size distribution measurements allowed for determining if aggregation was occurring as well as verifying the diameters of the particles. Zeta potential values further indicated the stability of the particle suspensions at various ionic strengths.

Selection of the flow system components, including glass beads, a flow cell, a syringe pump, syringes, tubing and fittings, required compatibility with flow applications as well as optical and fluorescent microscopy. Glass beads have been widely used as model porous media in many experiments. In this study, another reason to select glass beads is their optical properties are compatible with fluorescent microscopy. Flow cell selection also depended on the dimensions of the LSC microscope stage. The size of the flow cell was restricted by the space available on the microscope stage and the vertical clearance between the stage and the optic. Syringes, a syringe pump, tubing and fittings were purchased after the selection of the flow cell. Procedures for preparing glass beads and packing flow cells with a single layer of glass beads were developed.

3.2 Fluorescent Particles

3.2.1 Introduction

The particles used in this study are Fluorophorex™ Fluorescent Nanospheres (Phosphorex, Inc., Fall River, MA). They are uniform spheres made from polystyrene with a carboxyl surface functionalization. The fluorescence used to dye the particles is green with an excitation maximum at 480 nm and an emission maximum at 520 nm. The stock solution contains 0.1% Tween 20 in DI water and the antimicrobial agent is 2 mM NaN_3. The density of the particles is 1.06 g/cm^3 and the surface charge value provided by the manufacturer is 0.165 meq/g.

The fluorescent particles, shown in Figure 3.1, have reported diameters of 510 nm, 210 nm and 57 nm. One millimeter stock solutions with a solids content of 1% were purchased; however, the concentration in terms of the number of particles per milliliter of solution varies depending on the diameter of the particles. The concentrations of the stock solutions are 1.37×10^{11} #/mL for the 510 nm particles, 1.96×10^{12} #/mL for the 210 nm particles and 9.8×10^{13} #/mL for the 57 nm particles.

Figure 3.1 Particle suspensions in original shipping containers (1 mL)

3.2.2 Procedure for preparing particle suspensions

Particle suspensions were prepared for each individual experiment using standard dilution calculations. Only single-step dilutions directly from the stock particle suspensions were performed. Solids content was used as the concentration unit and solids contents of 0.005%, 0.0025% and 0.0005% were selected. The standard concentration was 0.0025% solids. Other concentrations were used only in experiments analyzing the influence of initial concentration.

The first step in particle suspension preparation was sonication of the stock particle suspension for five minutes. A precision pipette was used to obtain the volume of stock solution required for each dilution. The particle suspensions were prepared in a volumetric flask and diluted with DI water. Sodium bicarbonate ($NaHCO_3$) titrations using 0.1 M $NaHCO_3$ were performed to obtain a pH of 6.95±0.1 for each particle suspension. In cases when the pH was raised above the desired range, 10 mM HCl titrations were performed. Sodium chloride (NaCl) was used to obtain the ionic strength of each particle suspension. The ionic strengths used were 0 mM, 3 mM NaCl and 100 mM NaCl. The standard ionic strength, 3 mM NaCl, was used unless the specific experiment was investigating the influence of solution chemistry.

3.2.3 Procedure for particle size distribution measurements

Particle size distributions were measured using a 90Plus Particle Size Analyzer (Brookhaven Instruments Corporation, Holtsville, NY). The basis of the 90Plus Particle Size Analyzer is Dynamic Light Scattering (DLS) principles. In general, the analyzer can measure particles sizes ranging from 2 nm to 3000 nm. Photon Correlation Spectroscopy (PCS) of Quasi-Elastically Scatter Light (QLES) is the foundation of the analysis in which fluctuations about average, scattered, laser light intensity is correlated. The analysis typically requires a few minutes, has a relative error of ±1% and requires approximately 2 mL of sample.

The instrument is controlled by a computer and the governing software is user-friendly requiring the input of just a few simple parameters. Dust poses the biggest interference to the measurements, but the built-in dust filter is simple to manipulate in order to correct the interference. The result is a lognormal size distribution from which mean and standard deviation are calculated by weight. An effective diameter is measured using the analyzer and can be verified against the manufacturer's reported particle diameter. Unimodal size distributions provide confirmation of stable particle suspensions.

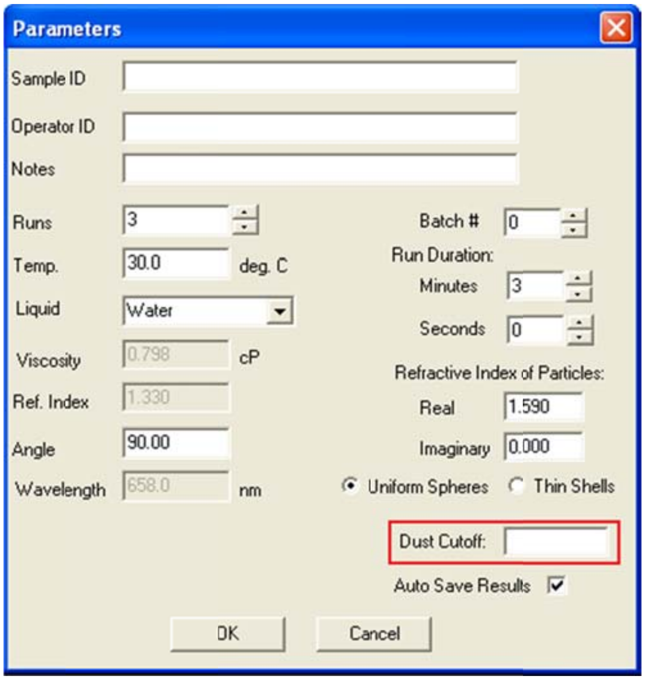

Sample ID
Operator ID
Notes
Runs: 3
Temp.: 30.0 deg. C
Liquid: Water
Viscosity: 0.798 cP
Ref. Index: 1.330
Angle: 90.00
Wavelength: 658.0 nm
Batch #: 0
Run Duration:
Minutes: 3
Seconds: 0
Refractive Index of Particles:
Real: 1.590
Imaginary: 0.000
● Uniform Spheres ○ Thin Shells
Dust Cutoff:
Auto Save Results ☑

Figure 3.2 90Plus Particle Size Analyzer parameters window

The 90Plus Particle Size Analyzer parameters window is shown in Figure 3.2. The value for the dust cutoff, shown within the red box, is entered there. The dust cutoff is an algorithm that rejects data corrupted by scattering due to dust. If the value for the dust cutoff is too high, 100% of the data is used for correlation. If the value is too low, a significant amount of data will be excluded from the correlation and the effective diameter reported will be smaller. Ideally, 98% data retention for correlation is desired. A value of 15 should be used for particles on the order of 10 nm. For particles on the order of a few 100 nm, a value of 30 is a starting point. The starting point for particles on the order of 1 μm is a dust cutoff value of 80. The user should take an iterative approach in adjusting the dust cutoff value until a reasonable amount of data is retained. For a very clean sample, it is acceptable to have 100% data retention.

3.2.4 Procedure for zeta potential measurements

Zeta potential measurements were performed using a ZetaPALS Zeta Potential Analyzer (Brookhaven Instruments Corporation, Holtsville, NY) which utilizes Phase Analysis Light Scattering (PALS), an extension of electrophoretic light scattering (ELS), to measure electrophoretic mobility (EPM) and thus calculate zeta potential. PALS is a more sensitive technique than ELS and is useful when measuring low EPM which can arise in particle suspensions for various reasons. One such reason is a medium of low dielectric constant or high viscosity. A second case is that in which high salt molarity leads to strong electrostatic shielding of particles in a highly conductive medium and limits the electric field which may be applied. Another case is a low mobility due to a low zeta potential. It has been shown that PALS is capable of measuring velocities 1000 times smaller than ELS.

The ZetaPALS Zeta Potential Analyzer requires the use of an electrode and preparation of a good particle suspension at an appropriate concentration. Keeping the cuvette and electrode clean is important due to the sensitivity of the instrument. The software is simple and requires the user to input just a few simple parameters. The main concern of the user is keeping the electrode clean and preventing contamination of the sample.

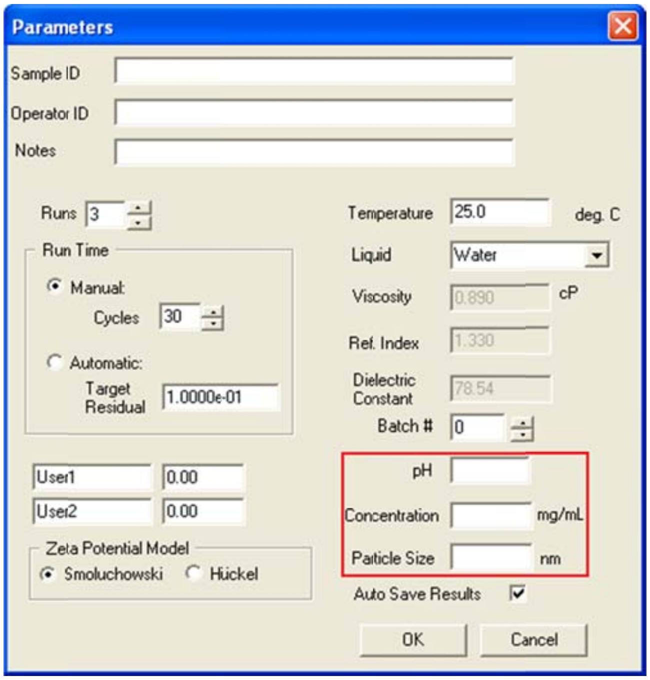

Sample ID
Operator ID
Notes
Runs 3
Run Time
● Manual: Cycles 30
○ Automatic: Target Residual 1.0000e-01
User1 0.00
User2 0.00
Zeta Potential Model
● Smoluchowski ○ Hückel
Temperature 25.0 deg. C
Liquid Water
Viscosity 0.890 cP
Ref. Index 1.330
Dielectric Constant 78.54
Batch # 0
pH
Concentration mg/mL
Paticle Size nm
Auto Save Results ☑

Figure 3.3 Zeta potential analyzer parameters window

The parameters window for the zeta potential analyzer is shown in Figure 3.3. For this study, the three parameters that varied each experiment were pH, concentration (mg/mL) and particle size (nm), shown in the red box. The pH needs to be calculated during sample preparation and manually inputted in its field in the parameters window. The particle concentration within the suspension can be calculated using the solids content of the suspension and the physical characteristics of the particles provide by the manufacturer; however, the concentration is not used by the software to calculate the results, but it can be plotted as a dependent variable during data analysis. The particle size also needs to be manually inputted. It serves purely as a label because the method employed by the software does not use particle size to calculate zeta potential.

3.3 Flow System Design

3.3.1 Glass beads

Spherical glass beads (Potters Industries, Inc., Valley Forge, PA) were selected as model porous media in this study. The glass beads have a density of 2.5 g/cm^3, a Knoop hardness of 515, an average compressive strength of 36,000 psi and a free silica content of 0%. The Potters designation for the glass beads is #3 and corresponds to a 20-30 U.S. sieve size resulting in a maximum diameter of 850 μm and a minimum diameter of 600 μm. The minimum percent of round particles provided by the manufacturer is 65%. The #3 glass beads were sieved using a size 25 U.S. sieve corresponding to 710 μm. The resulting range of diameters for the glass beads is from 600 μm to710 μm.

Prior to use, the glass beads were washed with pure acetone solution followed by pure hexane solution. The glass beads were then soaked in concentrated (12.1 M) hydrochloric acid (HCl) for 12 hours and then rinsed several times with DI water to remove residual HCl. Next, the glass beads were placed in a series of 20 minute ultrasonic baths using an FS60 Ultrasonic Cleaner (Fisher Scientific, Pittsburgh, PA) at room temperature containing 0.01 M sodium hydroxide (NaOH), DI water and 1.0 M nitric acid (HNO_3). The glass beds were then again rinsed with DI water until pH 7 was reached followed by oven-drying at 125 °C for 12 hours.

3.3.2 Flow cell

The flow cell chosen for this study was an ibidi μ-Slide I$^{0.8}$ Luer (ibidi LLC, Verona, WI) consisting of an uncoated hydrophobic plastic designed for high resolution microscope analysis. The optical quality of the material is comparable to glass and exhibits low birefringence and auto fluorescence. Experiments using fluorescence at all wavelengths from UV to IR (280-900 nm) are possible at an uncompromised resolution with this flow cell. The optical properties of the standard bottom are a refractive index n_D (589 nm) of 1.52, an Abbe number of 56 and a thickness of 180 µm. The thin bottom allows for low or high magnification up to 100X. The flow cell is 25.5 mm wide and 75.5 mm long.

The geometry of the flow channel is rectangular. The flow channel has a 5 mm width, 50 mm length and 0.8 mm height as shown in Figure 3.4. The channel volume is thus 0.2 mL. The bottom matches a No. 1.5 cover slip. The inlet and outlet of the flow channel are easily connected to tubes and pumps via Luer adapters.

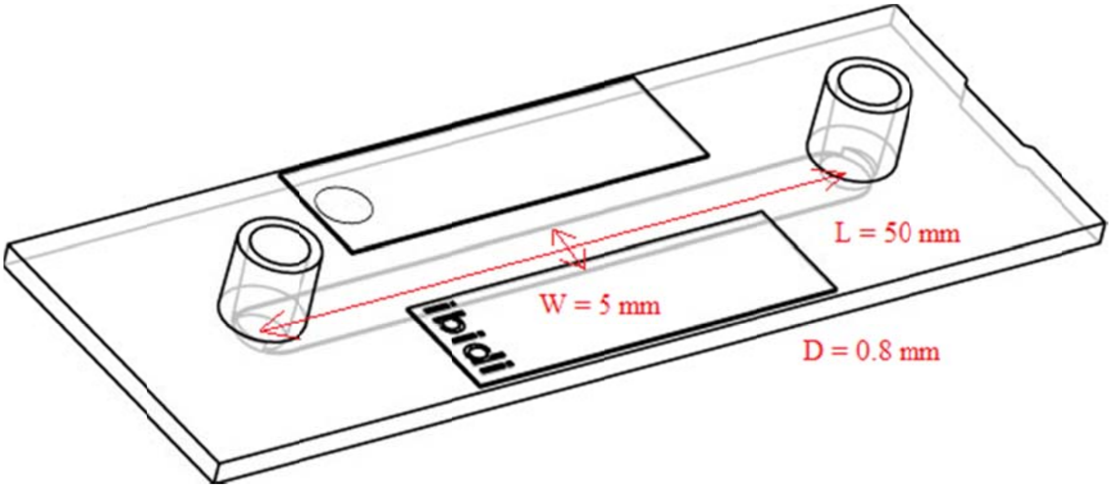

Figure 3.4 Flow channel dimensions

3.3.3 Tubing and fittings

Tubing and fittings were selected to complete the flow system. The tubing was TYGON® 3350 Sanitary Silicone Tubing (Saint-Gobain Performance Plastics Corporation, Beaverton, MI). The inner surface of the tubing is designed to reduce the risk of particle entrapment and microscopic build-up during fluid transfer. The manufacturer reports in-house analysis of the inner surface of its tubing reveals it is up to three times smoother than other silicone tubing and continues to prevent residue build-up even in repeat use applications. Further in-house tests for extractability show the tubing has a low extractable content helping to maintain purity during fluid transfer. The tubing has an inner diameter of 1/16 in, an outer diameter of 1/8 in and a wall thickness of 1/32 in.

The tubing was connected to the flow cell using an Elbow Luer Adapter (ibidi LLC, Verona, WI) made of polypropylene. The adapter has at one end a male luer and at the other end, a single barb connector. The adapter is designed for any connection between a female luer to flexible tubing with an inner diameter of 0.8-1.6 mm. The male luer end has an inner diameter of 2 mm and the single barb connector end has an inner diameter of 0.8 mm. The low height helps minimize interference with the optic when the flow cell is placed on a microscope stage. Figure 3.5 shows the connections between the flow cell, fittings and tubing.

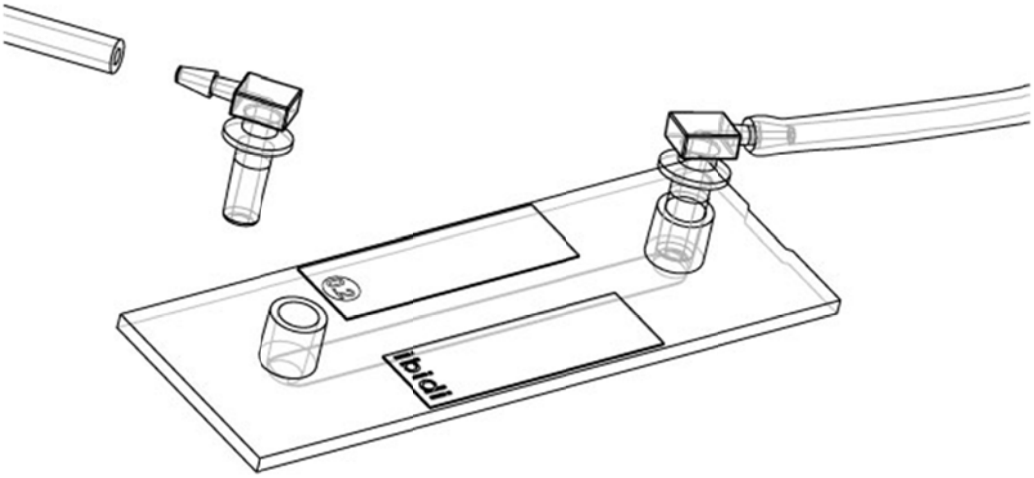

Figure 3.5 Flow cell, fittings and tubing

A three-way valve was used to allow air bubbles within the flow system to be released before reaching the flow cell. A three-way HV3-3 Valve (Hamilton Company

USA, Reno, NV) was selected and connected to the tubing using 1/16 in Barb to 1/4-28 Male (Upchurch Scientific®, Inc.) adapters made of Tefzel® (ETFE). The same adapter was used to connect a Quick Connect Female Luer to a 1/4-28 Female (Upchurch Scientific®, Inc.) adapter made of PEEK™. This adapter was able to connect to the syringe.

3.3.4 Syringe and syringe pump

The glass syringe used was a Hamilton 1025TLL 25 mL GASTIGHT® Syringe (Hamilton Company USA, Reno, NV). A KDS210 Infusion/Withdrawal Pump (KD Scientific, Inc., Holliston, MA) was selected for this study. The syringe pump holds up to two syringes ranging from 10 µL to 140 mL and has a minimum flow rate of 1.67×10^{-8} mL/min. Figure 3.6 provides a picture of the flow system setup in the LSC laboratory.

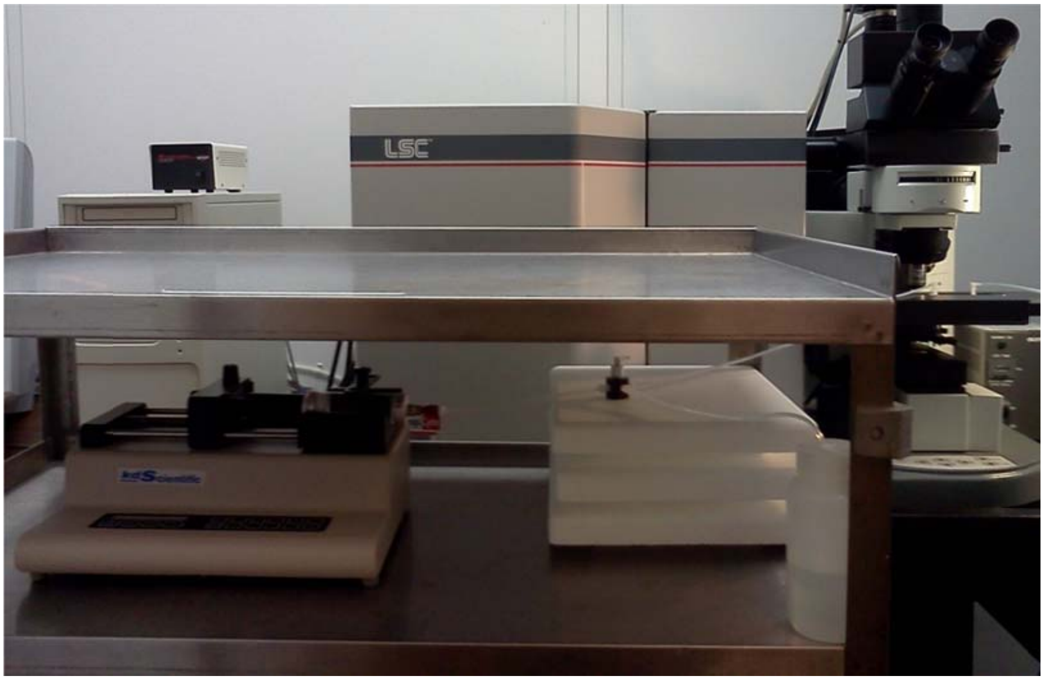

Figure 3.6 Flow system setup in Laser Scanning Cytometer laboratory

3.3.5 Procedure for flow cell packing

The first step in flow cell preparation was to weigh and record the mass of the empty flow cell. Next, the flow cell was packed with glass beads prepared according to the procedure presented in Section 3.3.1. Because the height of the flow channel is 0.8 mm, the glass beads selected had a range of diameters from 0.6 mm to 0.71 mm, corresponding to the first two standard U.S. sieve sizes of less than 0.8 mm. Using glass beads slightly less than the flow channel height allowed for a uniform single-layer of glass beads packing to be achieved.

The technique employed for flow cell packing required a funnel created from filter paper. The flow cell was held at an angle with the inlet higher than the outlet and the funnel was used to direct glass beads into the inlet of the flow channel. In instances when the glass beads resisted sliding through the channel, a pair of tweezers was used to tap the sides of the cell so as to shake the glass beds through the channel until they reached the end. It was difficult to pack the flow cell without having some excess glass beads accumulate within the inlet and outlet; therefore, tweezers were again used to tap the bottom of the flow cell under the inlet and outlet to pop some of the excess glass beads out until the glass bed level was equal to the channel height. The weight of the packed flow cell was then measured and recorded.

The porosity of the flow cell was measured in order to calculate the volume of solution corresponding to a pore volume (PV) for each experiment. The manufacturer reported the density of the glass beads as 2.5 g/cm^3. The mass of the glass beds was measured by subtracting the weight of the empty flow cell from that of the packed flow cell. The porosity was found by subtracting the volume of glass beads, determined from calculations using the glass bead mass and density, from the volume of the flow channel, reported as 0.2 mL by the manufacturer.

Another approach to estimate porosity is to calculate the volume of water in the pore spaces based on the measured mass and reported density of the water. The estimated porosity values using the two methods are comparable to each other. Measuring the porosity using water before each experiment was difficult because the flow cell must be removed from the flow system setup and then reattached without leaving any air bubbles in the system. This proved to be difficult. Thus, the approach based on glass bead volume was used in this study to estimate the porosity of packed flow cell.

Chapter 4

Experimental Methods

4.1 Introduction

In this study, an LSC was used to scan and thus identify the spatial distribution of particles that were stably attached in glass beads packed in a flow cell. The compatibility between the fluorescently dyed particles and the LSC system was initially verified by scanning fluorescent particle suspensions directly on standard microscope slides. The laser and PMT detector selection depended on the excitation and emission spectra of the fluorescent particles. The LSC parameters were adjusted separately for each size of particle. Next, suspensions were introduced into unpacked flow cells and scanned to determine the starting points for the LSC parameters for use during the flow cell experiments. The final step was to perform LSC scans using packed flow cells to fine-tune the LSC parameters and verify successful operation.

A series of experiments were performed to measure the effects of injection duration, solution chemistry, Darcy velocity and solids content on the retention of nanoparticles in porous media. The scan area used throughout the study was limited to the middle 12.5 mm of the length of the flow channel due to vertical clearance restrictions between the inlet and outlet of the flow cell and the microscope objective. The scan area, however, is consistent between each experiment. The standard for each experiment was 0.0025% solids content, 3 mM NaCl ionic strength and 0.04 cm/s Darcy velocity. Each experiment began with a 40 PV injection of particle suspension into the flow cell, which was already completely saturated with background solution. Next, 5 PV of background solution was injected. Such a procedure resulted in only stably attached particles remaining in the flow cell prior to the LSC scan. Flow cell experiments for each size of particle were conducted individually. In most cases, duplicates of each experiment were performed.

The Darcy velocities used were 0.08 cm/s, 0.06 cm/s, 0.04 cm/s and 0.02 cm/s. Solids contents of 0.005%, 0.0025% and 0.0005% were used and ionic strengths up to 100 mM NaCl were selected. Most of the flow cell experiments had injection durations of 40 PV; however, additional experiments using injection durations of 120 PV, 240 PV and 300 PV were performed to determine the presence of a maximum capacity for attachment. Another set of flow cell experiments was performed in which a rinse with corresponding background solution and a subsequent LSC scan was followed by a rinse with DI water and a second LSC scan to analyze the influence of solution chemistry and attachment in the secondary minimum.

4.2 Laser Scanning Cytometry

4.2.1 Introduction

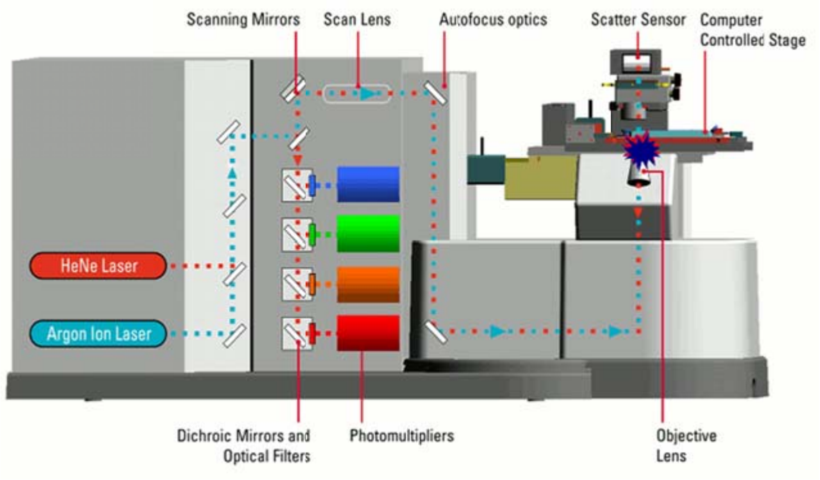

Figure 4.1 Laser Scanning Cytometer

The LSC, shown in Figure 4.1, (CompuCyte Corporation, Westwood, MA) is a microscope-based instrument that measures fluorescent constituents using a laser and up to four colors of fluorescence. The samples may appear directly on a microscope slide or within a liquid suspension. The LSC performs automated analysis of solid-phase samples using laser-based opto-electronics. The instrument simultaneously scans the sample and records the data including the exact position of each event along with several other properties. Figure 4.2 provides a picture of the LSC in the BM^3 Laboratory.

Figure 4.2 Laser Scanning Cytometer laboratory set-up

The process by which the LSC operates is shown in Figure 4.3 below. The software records several properties of each event, in addition to area and integral, including maximum pixel, time, x-position, y-position, perimeter and more. This data can be used to quantify the results as well as provide a spatial distribution of the data.

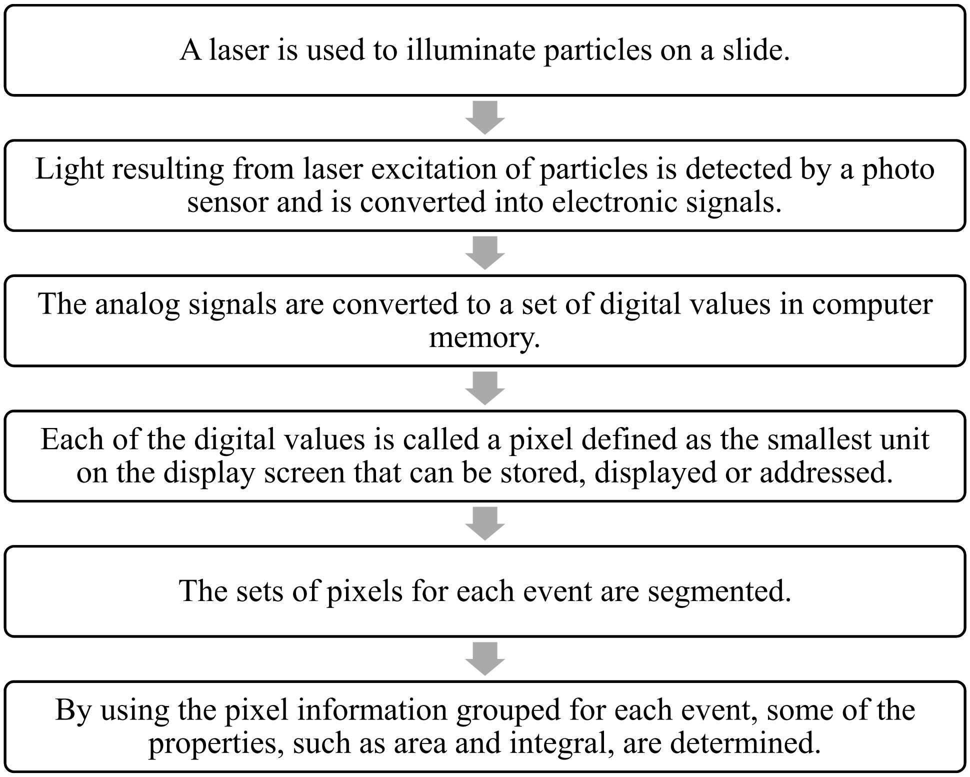

A laser is used to illuminate particles on a slide.

Light resulting from laser excitation of particles is detected by a photo sensor and is converted into electronic signals.

The analog signals are converted to a set of digital values in computer memory.

Each of the digital values is called a pixel defined as the smallest unit on the display screen that can be stored, displayed or addressed.

The sets of pixels for each event are segmented.

By using the pixel information grouped for each event, some of the properties, such as area and integral, are determined.

Figure 4.3 Process by which the Laser Scanning Cytometer operates

4.2.2 Microscope unit

The microscope is a standard Olympus BX-50 with a motorized stage as shown in Figure 4.4. It is equipped with an objective turret. The objectives available are 10X, 20X and 40X with nominal beam or spot sizes of 10 µm, 5 µm and 2.5 µm, respectively. A slider control allows the user to switch from the brightfield, used when focusing the microscope, to the laser beam used during scanning. Because the flow cell is thicker than a standard microscope slide, the 40X objective cannot be used due to vertical clearance restrictions. For this experiment, the 20X objective is used. A more powerful object could be used if the focal length is long enough.

Figure 4.4 Microscope unit portion of the Laser Scanning Cytometer

4.2.3 Laser selection

The LSC has two lasers. One laser is a 20 mW argon ion laser (488 nm, Cyonics Uniphase Model 2014A-20SL). The other is a 5 mW red HeNe laser (633nm, Cyonics Uniphase). Each laser provides a different wavelength to excite fluorescent samples. In order to select a laser, the user must obtain the excitation spectra for the fluorescence used to stain the sample. Ideally, the user should select fluorescence with an excitation maximum as close to the wavelength a laser provides as possible. It is important to know some spectra provided may have been created for the fluorescent dye before it was used to dye the particles and a slight variation in the spectra may occur following the application of the dye to the particles.

The excitation and emission spectra for the green fluorescence are presented in Figure 4.5. The broken green line represents the excitation spectra of the green fluorescence. The green fluorescence has an excitation maximum at 480 nm. The solid green line represents the emission spectra of the green fluorescence with an emission maximum at 520 nm.

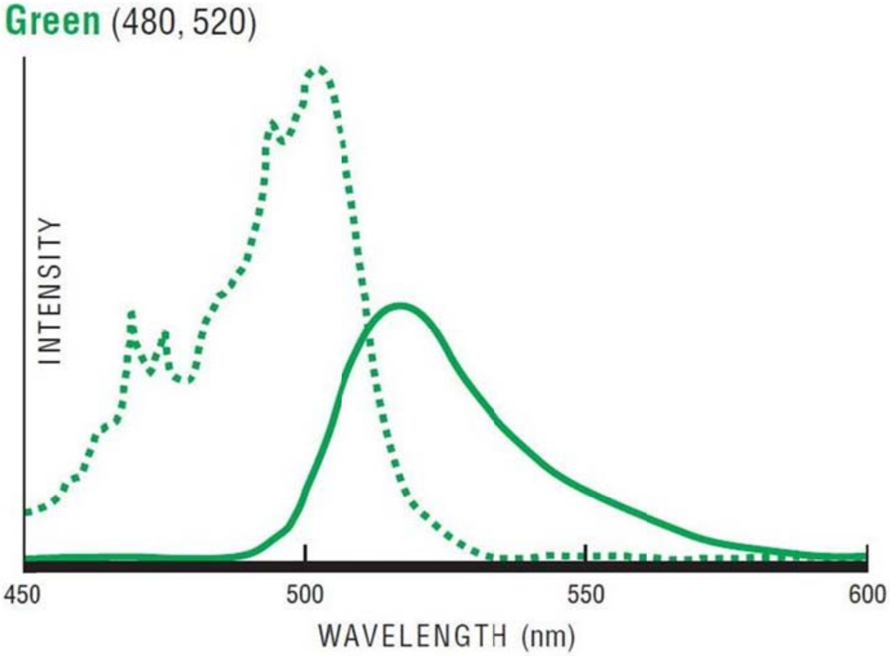

Figure 4.5 Excitation (broken) and emission (solid) spectra of green fluorescence

The LSC's 5 mW red HeNe laser provides a wavelength of 633 nm which does not intersect the excitation spectrum for the green fluorescence; thus, the 5 mW red HeNe laser will be unable to excite the green fluorescence. In Figure 4.6, the red line represents the wavelength 488 nm provided by the 20 mW argon ion laser. This wavelength falls near the excitation maximum for the green fluorescence and it is reasonable to believe the combination of this laser and the selected fluorescence will result in excitation.

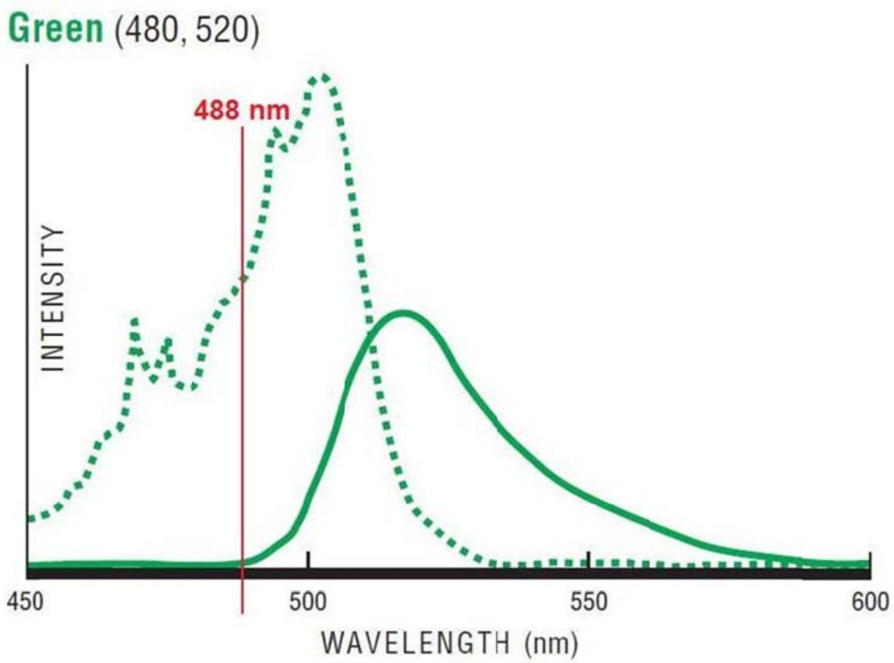

Figure 4.6 Wavelength provided by the 20 mW argon ion laser (red) graphed to show intersection with excitation spectrum of the green fluorescence (broken)

4.2.4 Photomultiplier tube selection

The LSC has PMT detectors each measuring a different range of wavelengths. The fluorescent light given off by the dyed particles is collected and transmitted to up to four PMT detectors that process the light selected by each filter. The following optical filter tubes are available (ID, wavelength/bandpass and typical dye used are listed):

- B: 463/39 (DAPI),
- D: 530/30 (FITC, Green Fluorescent Protein),
- J1: 580/30 (PE),
- K1: 625/28 (PI) and
- H1: 650/LP (CY5).

The first number given represents the wavelength the optical filter tube is centered at and the second number represents the range of wavelengths covered. The LSC has the capacity for four PMT detectors which can be operated simultaneously. Figure 4.7 provides a picture showing the location of the PMT detectors on the LSC.

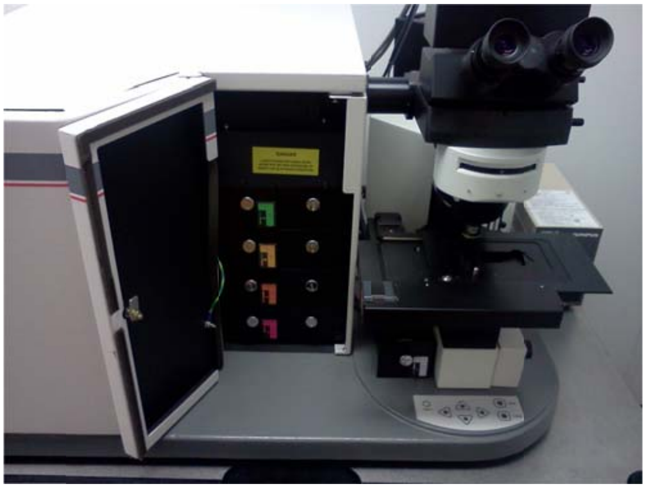

Figure 4.7 Location of PMT detectors within the Laser Scanning Cytometer

The solid green line in Figure 4.8 represents the emission spectra for the green fluorescence. The maximum intensity occurs at the wavelength 520 nm. The vertical blue lines at 515 nm and 545 nm represent the range of wavelengths covered by the D: 530/30 optical filter tube. The maximum intensity falls within this range and thus it is reasonable to believe the combination of this optical filter tube, the 20 mW argon laser selected previously and the green fluorescence will result in successful excitation and emission of the fluorescently dyed particles.

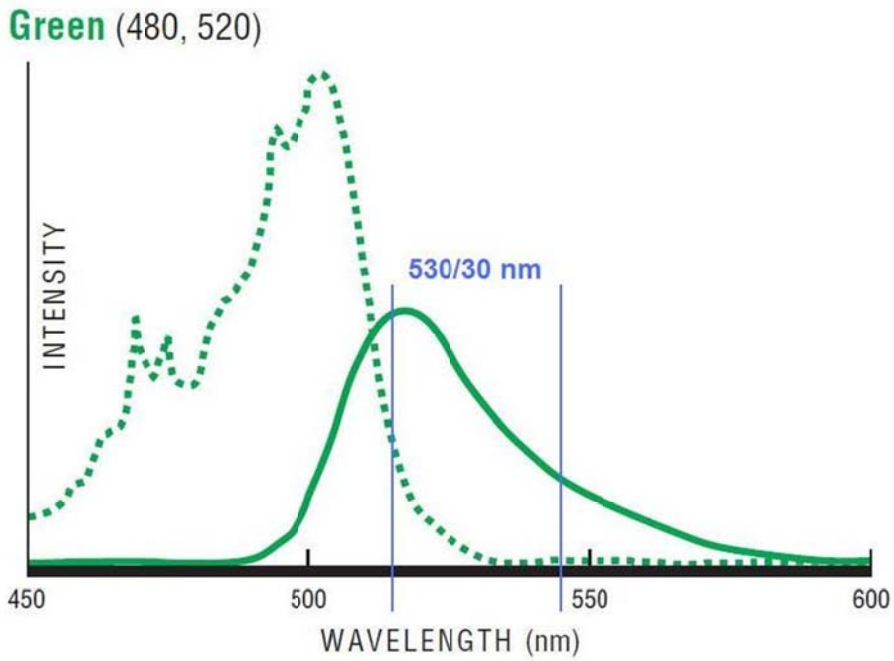

Figure 4.8 Range of wavelengths provided by the D: 530/30 optical filter tube (blue) graphed to show intersection with emission spectrum of the green fluorescence (solid)

The combination of laser and optical filter tube used for the fluorescent particles should be verified by trial experiments. Figure 4.9 shows the set sensors dialogue window in which four optical filter tubes are activated in combination with the 20 mW argon laser to scan fluorescent particles. The D: 530/30 optical filter tube is labeled as blue in the figure and indicates the strongest response when all four optical filter tubes are operating at the same PMT (%) and offset. This verifies that the selection of this optical filter tube and laser combination is acceptable.

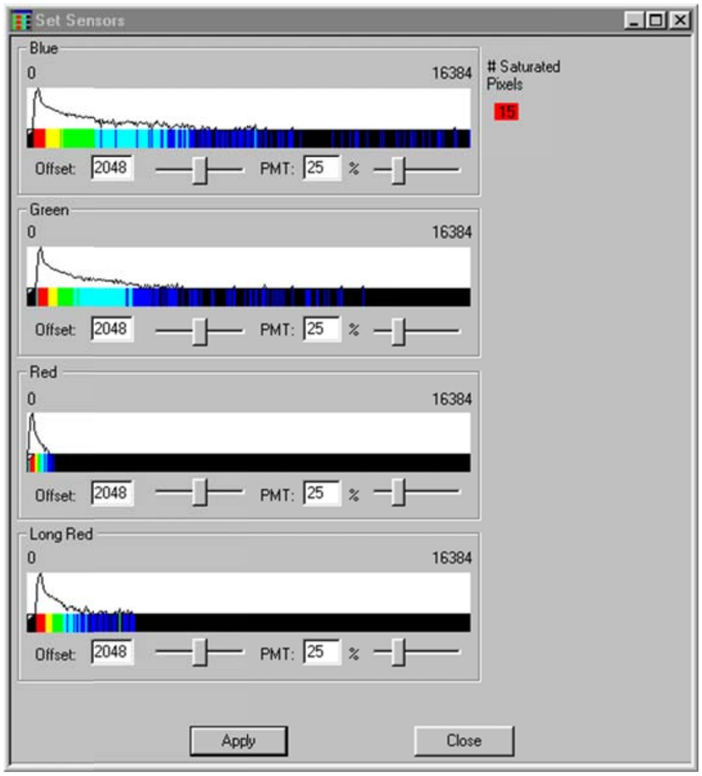

Blue
0 16384
Saturated Pixels 15
Offset: 2048 PMT: 25 %

Green
0 16384
Offset: 2048 PMT: 25 %

Red
0 16384
Offset: 2048 PMT: 25 %

Long Red
0 16384
Offset: 2048 PMT: 25 %

Figure 4.9 Set sensors dialogue window from Laser Scanning Cytometer software

4.2.5 Defining the scan area

The LSC uses a coordinate system in which all of the measurements are in microns and are measured from the origin located at the top-right corner of the slide. The x-axis, parallel to the length of the slide, is approximately 110 mm and the y-axis, parallel to the width of the slide, is approximately 51.5 mm. Scans occur in 0.5 µm steps in the x-direction. Each time a single laser scan occurs in the y-direction and the length covered by each scan depends on the power of the objective.

For this experiment, the entire flow channel cannot be scanned due to spatial restrictions as a result of the elbow luer adapters protruding up from the flow cell high enough to come in contact with the microscope objective. As a result, only the middle 12.5 mm of the flow channel are scanned. Using the flow cell dimensions provided by the manufacturer and the pre-defined coordinate system of the LSC, the scan area was mathematically determined and manually inputted into the CompuCyte WinCyte software. Figure 4.10 shows the scan area dialogue window with the green rectangle representing the scan area for this study. The four corner points were manually inputted to define the scan area. For the x-axis, the start point is 31,500 and the end point is 44,000, given in the LSC predefined coordinate system. For the y-axis, the start point is 10, 250 and the end point is 15,250, again given based on the same coordinate system.

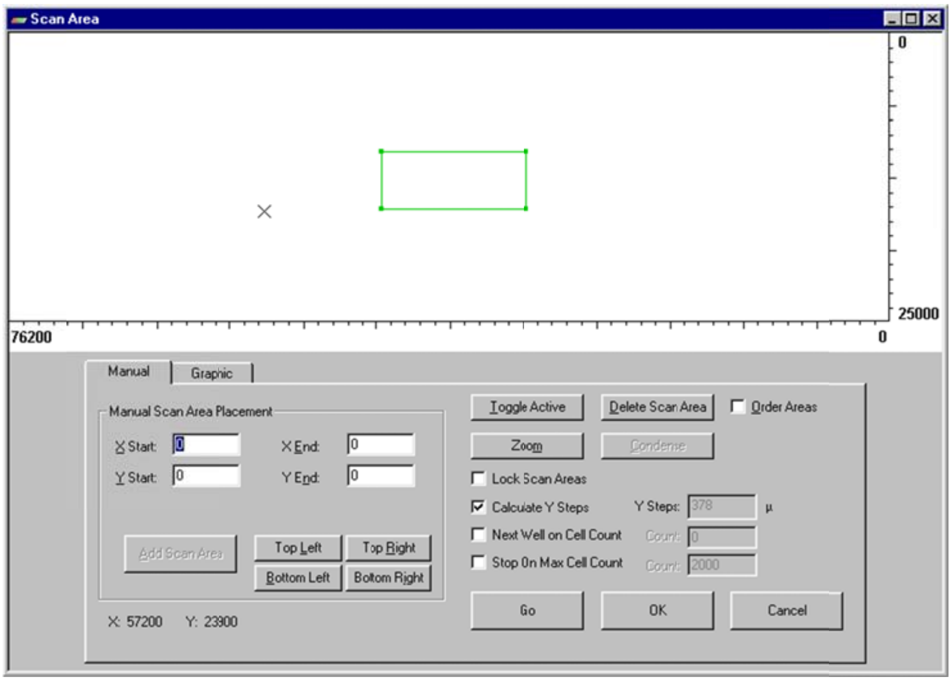

Manual Scan Area Placement

X Start: 0

X End: 0

Y Start: 0

Y End: 0

☐ Order Areas

☐ Lock Scan Areas

☑ Calculate Y Steps Y Steps: 378 µ

☐ Next Well on Cell Count Count: 0

☐ Stop On Max Cell Count Count: 2000

X: 57200 Y: 23900

Figure 4.10 Scan area dialogue window from Laser Scanning Cytometer software

4.2.6 Setting the parameters

Scanning requires the adjustment of PMT (%) and offset through an iterative process. In the instrument settings dialogue window shown in Figure 4.11, select lasers can be activated and the PMT (%) and offset values can be set. The PMT (%) should be adjusted so the color bars are in the upper third of the scale as shown in Figure 4.12, which depicts the blue PMT detector in the set sensors dialogue window. Ideally, the signal should be as high as possible while minimizing the number of saturated pixels.

Saturation occurs when the pixel reaches the maximum allowable value of 16,384 and the detector no longer responds to increased signal levels.

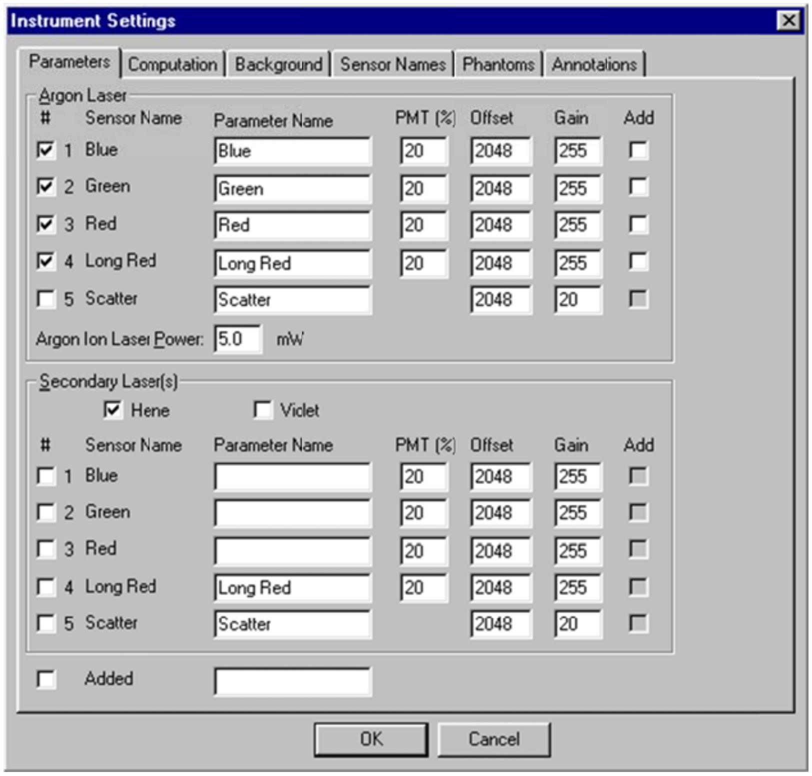

Argon Laser

#	Sensor Name	Parameter Name	PMT (%)	Offset	Gain	Add
☑ 1	Blue	Blue	20	2048	255	☐
☑ 2	Green	Green	20	2048	255	☐
☑ 3	Red	Red	20	2048	255	☐
☑ 4	Long Red	Long Red	20	2048	255	☐
☐ 5	Scatter	Scatter		2048	20	☐

Argon Ion Laser Power: 5.0 mW

Secondary Laser(s)

☑ Hene ☐ Violet

#	Sensor Name	Parameter Name	PMT (%)	Offset	Gain	Add
☐ 1	Blue		20	2048	255	☐
☐ 2	Green		20	2048	255	☐
☐ 3	Red		20	2048	255	☐
☐ 4	Long Red	Long Red	20	2048	255	☐
☐ 5	Scatter	Scatter		2048	20	☐

☐ Added

Figure 4.11 Instrument settings dialogue window from Laser Scanning Cytometer software

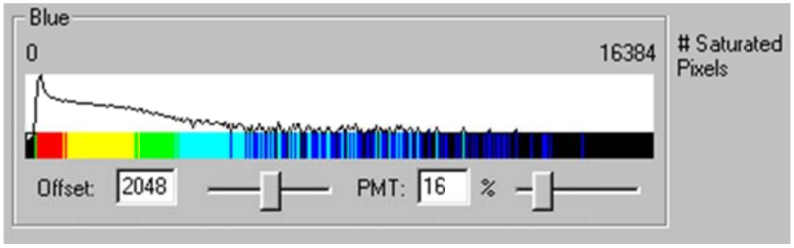

Offset: 2048

PMT: 16 %

Figure 4.12 Blue PMT detector in set sensors dialogue window from Laser Scanning Cytometer software

An instance in which the PMT (%) is set too high and saturation is occurring is depicted in Figure 4.13. The red box with a number inside of it indicates the presence and number of saturated pixels. The saturation occurs because the PMT (%) was increased from 16% in the first figure to 20% in the second figure. The PMT (%) value of 16% results in the dark blue color (the furthest to the right) registering in the upper third of the scale which is ideal; no saturation is occurring. This is indicative of the desired parameters for that situation. The offset should be adjusted so as to achieve a small gap between the zero point and the beginning of the color bars. In the figures below, the black area between the zero point and the red portion of the color bar indicates the offset is acceptable.

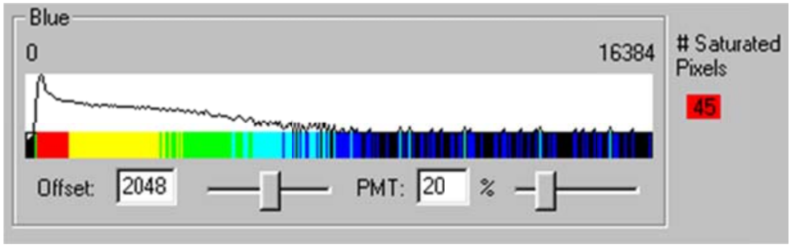

Saturated Pixels: 45

Offset: 2048

PMT: 20 %

Figure 4.13 Saturation occurring with blue laser

4.3 Flow Cell Experiments

<u>4.3.1 Introduction</u>

A typical LSC scan duration is roughly 20 minutes using the scan area defined for this study. Considering the duration of a single scan, it is very difficult to scan mobile particles in the flow cell system. This study focused on using LSC scans to record stably attached particles. Such a capability is adequate for investigating the attachment of nanoparticles on glass bead surfaces.

During the stable attachment experiments, the flow system setup is in the LSC laboratory and the flow cell is mounted on the LSC microscope stand as shown in Figure 4.14 and Figure 5.15, respectively. The syringe, tubing and flow cell are all positioned as near to the same elevation as possible. In order to account for this volume when determining the volume of particle suspension and background solution to introduce, the volume of solution between the syringe and three-way valve was measured, as was the volume between the three-way valve and the flow cell inlet.

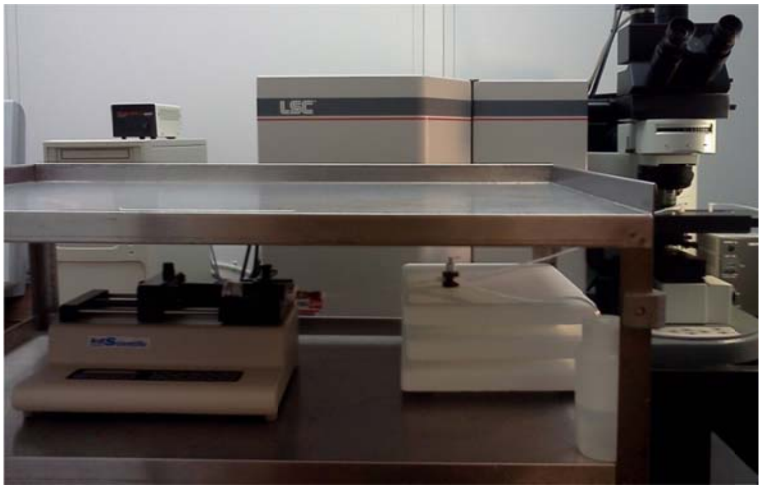

Figure 4.14 Flow system setup in the Laser Scanning Cytometer laboratory

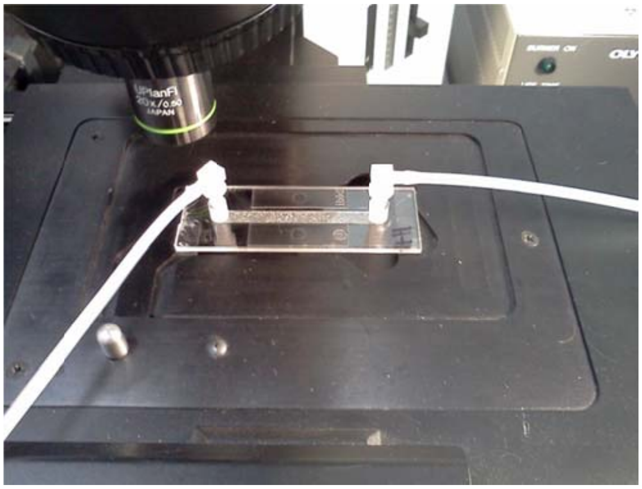

Figure 4.15 Flow cell mounted on the Laser Scanning Cytometer microscope stand

4.3.2 Flow cell experimental procedure

Each experiment begins with a 0.5 mL background solution rinse at 0.1 mL/min. These values were selected based on data from previous studies [29]. In order to insure 0.5 mL of background solution is introduced into the flow channel initially, it is important to take into account the volume of solution required to reach the flow channel inlet. It is important to visually inspect the flow system to make sure air bubbles are not present and the flow channel is completely saturated.

Following a background solution rinse, particle suspension will be injected. Injection velocities used are 0.08 cm/s, 0.06 cm/s, 0.04 cm/s and 0.02 cm/s. The standard velocity is 0.04 cm/s and the other velocities are used to analyze the influence of Darcy velocity on stable attachment.

The introduction of the particle suspension requires the syringe containing the background solution to be switched with the syringe containing the particle suspension. It is important to position the three-way valve so as to prevent backflow from the flow channel when switching syringes. Once the syringe containing the particle suspension is attached, a volume of solution is pumped in order to fill the tube between the syringe and the three-way valve insuring no air bubbles are present.

The standard injected PV of particle suspension used for this study is 40 PV. Larger PVs are used during experiments analyzing the influence of injection duration. A 40 PV standard was selected based on previous pore-scale experiments [29] with consideration for the time it takes to conduct an experiment at the minimum velocity. Because the tubing between the syringe and the three-way valve has been filled with particle suspension, only 40 PV is pumped after switching the valve to allow fluid to flow towards the flow cell. The three-way valve again needs to be positioned to prevent backflow from the flow cell after the 40 PV is complete. At this point, a portion of the 40 PV of particle suspension is located in the tubing between the three-way valve and the flow cell.

Following injection of 40 PV of particle suspension, 10 PV of background solution will be introduced into the flow cell. The purpose of the background solution rinse is to flush unattached particles from the flow channel, so that stably attached particles can be investigated. The same technique as before is required to fill the tubing between the syringe and the three-way valve, being careful to avoid air bubbles in the flow system. Because the tubing after the three-way valve is still filled with a portion of the particle suspension, the background solution rinse requires 10 PV in addition to the volume of solution between the valve and the flow cell. Once the rinse is complete, the three-way valve is again closed in order to prevent backflow from the flow channel during the LSC scan.

4.3.3 Procedure for Laser Scanning Cytometer scans

The first step in performing an LSC scan is focusing the microscope. The LSC is only able to record the particles attached within its depth of field. Using a 20x magnification, the depth of field is 5.8 μm, while the depth of flow cell is 0.8 mm. Thus, the LSC can only detect a portion of the particles attached onto glass bead surfaces. For this study, the microscope is slowly brought into focus until the top of the glass beads just come into focus. Although only a portion of the attached particles are detectable, the scanning results are comparable between each experiment because the scan area and the focusing location are consistent.

The second step of an LSC scan is to define the scan area. As discussed previously, the scan area covers the middle 12.5 mm of the flow channel. The start x-position is 31,500 and the end x-position is 44,000. The start y-position is 10,250 and the end y-position is 15,250. Once the user has inputted these vales to manually define the scan area, the protocol can be saved and used for all future scans.

Following the definition of the scan area, the parameters for the scan are set. This study used the 20 mW argon ion laser and the D: 530/30 (FITC, Green Fluorescent Protein) optical filter tube selected based on excitation and emission spectra of the green fluorescence used to dye the particles, as detailed in Section 4.2.3 and Section 4.2.4. The two main parameters that must be considered are the PMT (%) and offset gain. This is first done through an iterative process. The PMT (%) should be adjusted so the color bars are in the upper third of the scale. Ideally, the signal should be as high as possible while minimizing the number of saturated pixels. The offset should be adjusted so as to achieve a small gap between the zero point and the beginning of the color bars.

The parameters used in this study are shown in Table 4.1. These values are reported as a reference for future studies and are not necessarily the values that should be used. As the fluorescence ages or new batch suspensions are purchased, the values for these parameters may need adjustment. An iterative approach is the only method to optimize these values. After the scan area is set, the laser and optical filter tube are selected and the parameters are inputted, the scan is ready to proceed. The entire scan takes approximately 20 minutes for the scan area and magnification used in this study. Following the completion of the scan, the cell file can be saved and the data can be exported as a text file to be analyzed using other software.

Table 4.1 Typcal Laser Scanning Cytometer software parameters for flow cell experiemnts

Diameter	**PMT (%)**	**Offset Gain**
510 nm	25	1900
210 nm	25	1900
57 nm	40	1950

Chapter 5

Results and Analysis

5.1 Overview

In this chapter, experimental results are presented and analyzed. Particle characterization results, including particle size distribution and zeta potential measurements, and flow cell experiment results will be covered. The particle size distribution results will be presented in tables as well as graphically in the form of differential distributions and cumulative undersize distributions. Zeta potential measurements will be presented in tabular and graphical form as a function of zeta potential (mV) versus ionic strength (mM NaCl). The results of 25 flow cell experiments (with duplicates) will be presented using graphs, histograms and spatial distribution figures. An experimental matrix is presented in Table 5.1. Flow cell experiments were conducted to investigate the transport and retention of three different size particles, 510 nm, 210 nm and 57 nm. In these experiments, several parameters including injection duration, solution chemistry, Darcy velocity and solids content were varied.

Table 5.1 Experimental matrix for flow cell experiments

Exp.	Dia. (nm)	Solids Cont. (%)	mM NaCl	Darcy Vel. (cm/s)	Inj. Duration (PV)
001	510	0.0025	3	0.08	40
002	510	0.0025	3	0.06	40
003	510	0.0025	3	0.04	40
004	510	0.0025	3	0.02	40
005	510	0.005	3	0.04	40
006	510	0.0005	3	0.04	40
011	210	0.0025	3	0.08	40
012	210	0.0025	3	0.06	40
013	210	0.0025	3	0.04	40
014	210	0.0025	3	0.02	40
015	210	0.005	3	0.04	40
016	210	0.0005	3	0.04	40
021	57	0.0025	3	0.08	40
022	57	0.0025	3	0.06	40
023	57	0.0025	3	0.04	40
024	57	0.0025	3	0.02	40
025	57	0.005	3	0.04	40
026	57	0.0005	3	0.04	40
031	510	0.0025	3	0.08	120
032	57	0.0025	3	0.08	120
033	510	0.0025	3	0.04	120
034	57	0.0025	100	0.04	40
035	57	0.0025	3	0.08	300
036	510	0.0025	3	0.04	240
037	510	0.0025	100	0.04	40

5.2 Particle Characterization

5.2.1 Particle size distributions

Particle size distributions were measured in order to confirm the particle diameters reported by the manufacturer as well as to monitor the effect of solution chemistry on particle aggregation. Particle suspensions were shipped in 1 mL bottles labeled with a diameter for the contained particles in suspension; however, a product data sheet was also provided by the manufacturer which reported a mean diameter different from that of the bottle. The mean diameter reported on the product data sheet was confirmed to be the official manufacturer value.

The measurement parameters were consistent for each of the particle size distribution experiments performed. The only parameter that varied was the dust cutoff, an algorithm that rejects data corrupted by scattering due to dust, in order to obtain 90-98% data retention. For the 510 nm particles, the dust cutoff used was 40.00 and for the 210 nm and 57 nm particles, it was 20.00.

The first particle size distribution experiment that will be presented is for the 510 nm particles. The suspension used for this experiment was 0.0025% solids in DI water. Table 5.2 gives the measurement parameters for this experiment and the measurement results are presented in Table 5.3. The mean effective diameter for this experiment is 518.6 nm, a 1.69% difference from the diameter provided on the product data sheet. The mean polydispersivity, a measure of the non-uniformities existing in the distribution, is 0.004. The experiment has a mean baseline index of 9.1 and mean data retention of 99.00%.

Table 5.2 Measurement parameters for 510 nm particle size distribution measurement

Parameter	**Value**
Temperature	25.0
Suspension	Water
Viscosity	0.890 cp
Ref. Index Fluid	1.330
Angle	90.00
Wavelength	658.0 nm
Dust Cutoff	40.00
Runs Completed	3
Run Duration	3 minutes
Total Elapsed Time	9 minutes
Average Count Rate	342.0 kcps
Ref. Index Real	1.590
Ref. Index Imaginary	0.000

Table 5.3 Measurement results for 510 nm particle size distribution experiment

Run	**Eff. Dia. (nm)**	**Half Width (nm)**	**Polydispersivity**	**Baseline Index**
1	525.4	16.6	0.001	8.4 / 100.00%
2	512.1	36.2	0.005	9.2 / 98.50%
3	518.4	36.7	0.005	9.8 / 98.50%
Mean	518.6	29.8	0.004	9.1 / 99.00%
Std. Error	3.8	6.6	0.001	0.4 / 0.50%
Combined	518.7	36.7	0.005	9.2 / 99.00%

The lognormal size distribution results for the 510 nm particle size distribution measurement are presented in Figure 5.1 and Figure 5.2. Figure 5.1 shows the cumulative undersize distribution, the percent of the size distribution at or below the diameter. Figure 5.2 shows the differential size distribution; a unimodal distribution confirming the narrow distribution of particle sizes.

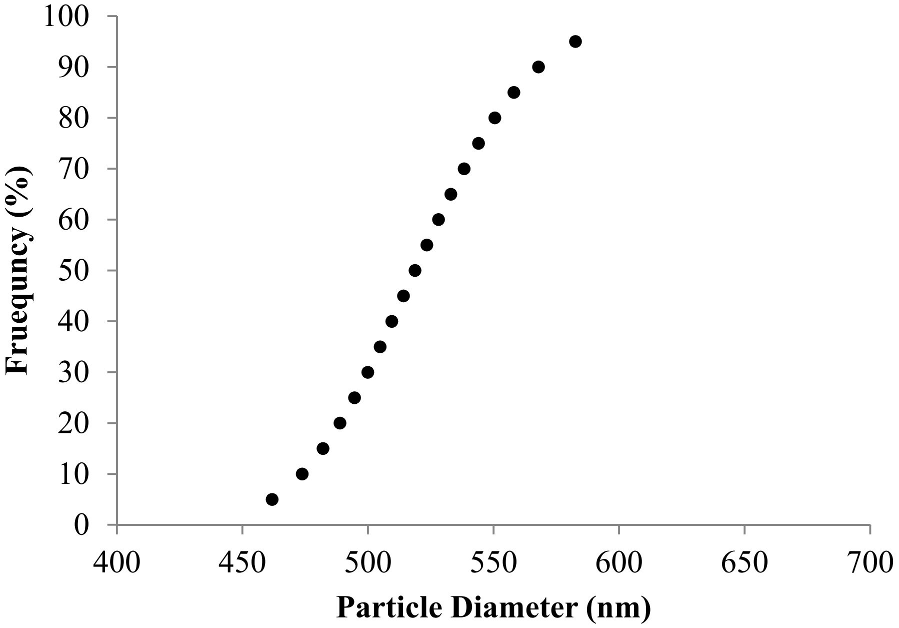

Figure 5.1 Cumulative undersize distribution for 510 nm particle suspension

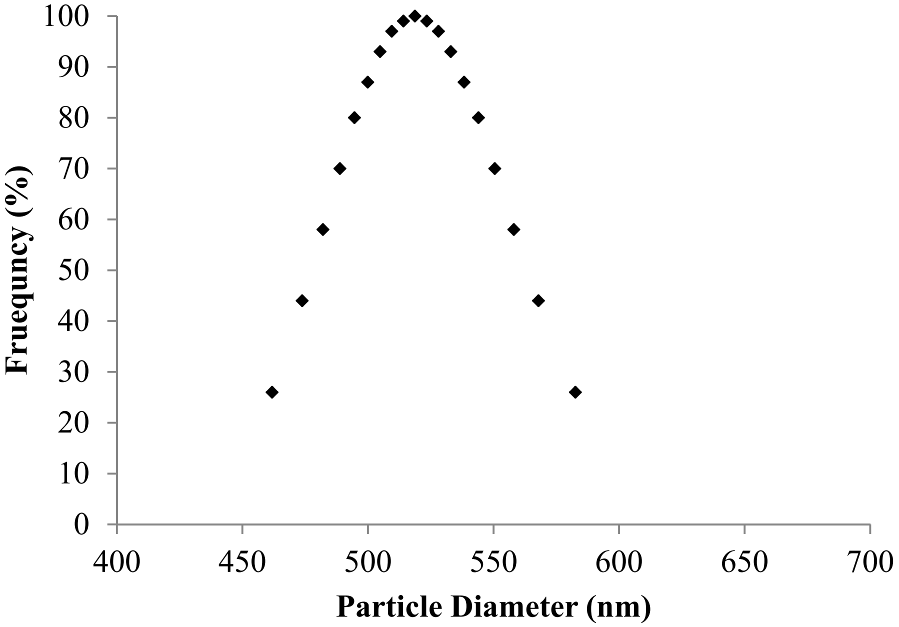

Figure 5.2 Differential distribution for 510 nm particle suspension

The particle size distribution experiment for the 210 nm particles was performed similarly. The suspension used for the experiment was 0.0025% solids in DI water. Measurement parameters for this experiment are provided in Table 5.4 and the measurement results are given in Table 5.5. The mean effective diameter measured is 201.3 nm, a 4.14% difference from the diameter provided on the product data sheet. The mean polydispersivity is 0.018 and the mean baseline index and data retention is 9.3 and 92.95%, respectively.

Table 5.4 Measurement parameters for 210 nm particle size distribution measurement

Parameter	**Value**
Temperature	30.0
Suspension	Water
Viscosity	0.798 cp
Ref. Index Fluid	1.330
Angle	90.00
Wavelength	658.0 nm
Dust Cutoff	20.00
Runs Completed	3
Run Duration	3 minutes
Total Elapsed Time	9 minutes
Average Count Rate	478.4 kcps
Ref. Index Real	1.590
Ref. Index Imaginary	0.000

Table 5.5 Measurement results for 210 nm particle size distribution measurement

Run	**Eff. Dia. (nm)**	**Half Width (nm)**	**Polydispersivity**	**Baseline Index**
1	204.2	17.6	0.007	10.0 / 94.78%
2	200.6	40.3	0.040	8.1 / 90.46%
3	199.0	14.1	0.005	9.7 / 93.59%
Mean	201.3	24.0	0.018	9.3 / 92.95%
Std. Error	1.5	8.2	0.011	0.6 / 1.29
Combined	201.3	17.5	0.008	9.4 / 92.95%

The lognormal size distribution results of the 210 nm particle size distribution experiment are presented in the following figures. Figure 5.3 shows the cumulative undersize distribution. The differential size distribution is presented in Figure 5.4.

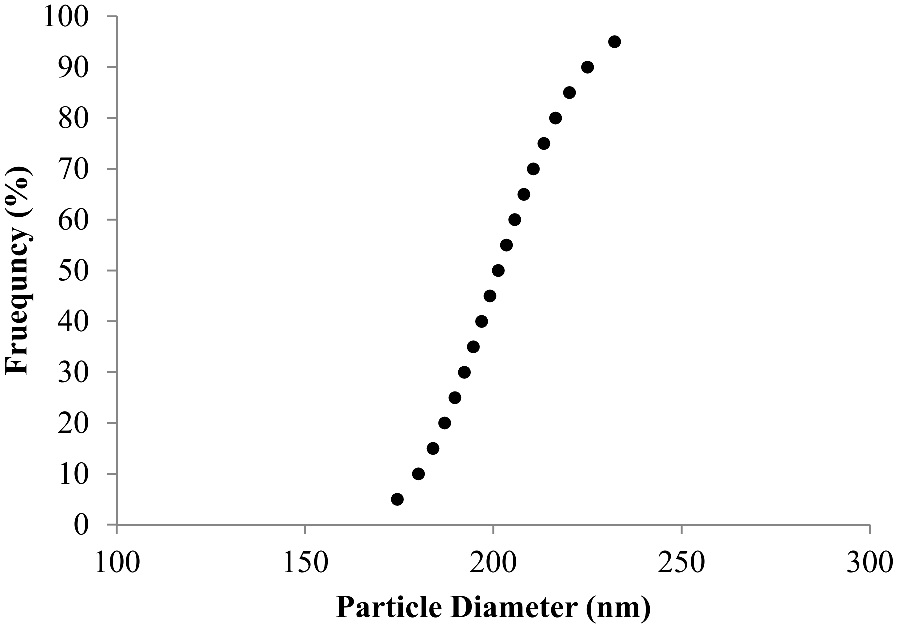

Figure 5.3 Cumulative undersize distribution for 210 nm particle suspension

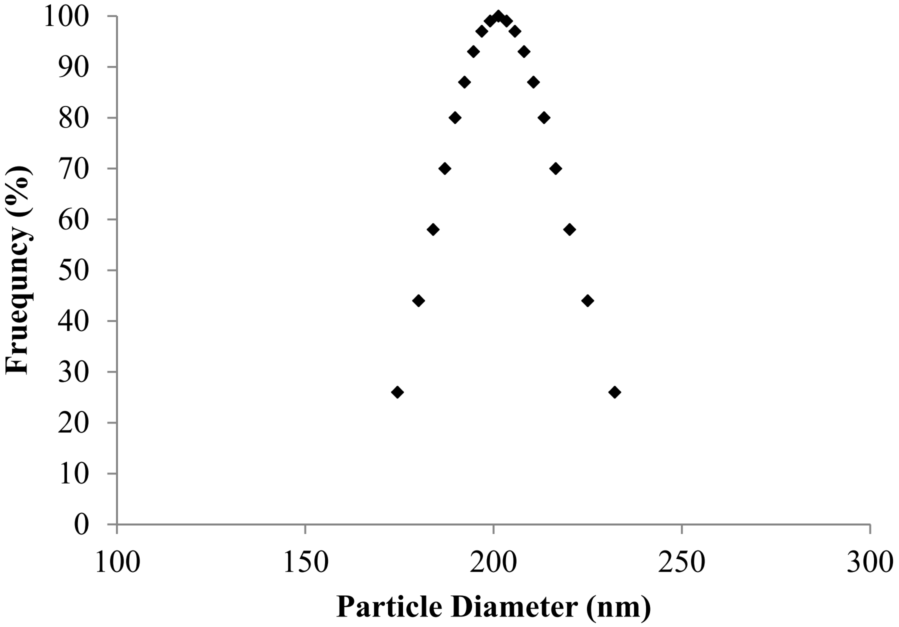

Figure 5.4 Differential distribution for 210 nm particle suspension

The particle size distribution experiment for the 57 nm particles was performed similarly to the experiments for the previous two particle sizes; however, the results were slightly more difficult to obtain. The small size of the particles seemed to make them more susceptible to interference from dust. The suspension used for the experiment was 0.0025% solids in DI water. Table 5.6 provides the measurement parameters and Table 5.7 gives the measurement results. The mean effective diameter measured is 64.5 nm, a 13.2% difference from the diameter provided on the product data sheet. The mean polydispersivity is 0.155 and the mean baseline index and data retention is 9.0 and 90.30%, respectively.

Table 5.6 Measurement parameters for 57 nm particle size distribution measurement

Parameter	**Value**
Temperature	30.0
Suspension	Water
Viscosity	0.798 cp
Ref. Index Fluid	1.330
Angle	90.00
Wavelength	658.0 nm
Dust Cutoff	20.00
Runs Completed	3
Run Duration	3 minutes
Total Elapsed Time	9 minutes
Average Count Rate	520.4 kcps
Ref. Index Real	1.590
Ref. Index Imaginary	0.000

Table 5.7 Measurement results for 57 nm particle size distribution measurement

Run	**Eff. Dia. (nm)**	**Half Width (nm)**	**Polydispersivity**	**Baseline Index**
1	64.5	27.1	0.176	9.2 / 90.19%
2	64.2	24.7	0.148	9.2 / 91.69%
3	64.6	24.4	0.142	8.5 / 89.00%
Mean	64.5	25.4	0.155	9.0 / 90.30%
Std. Error	0.1	0.9	0.011	0.3 / 0.78
Combined	64.5	25.5	0.156	9.0 / 90.30%

The 57 nm particle size distribution experiment lognormal size distribution results are presented in the following figures. The cumulative undersize distribution and differential size distribution are provided in Figure 5.5 and 5.6, respectively.

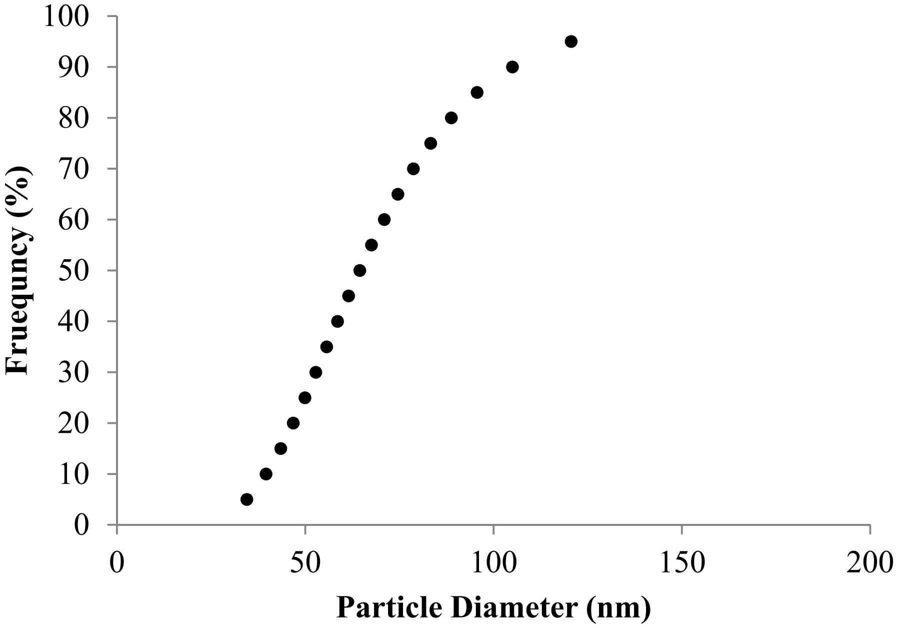

Figure 5.5 Cumulative undersize distribution for 57 nm particle suspension

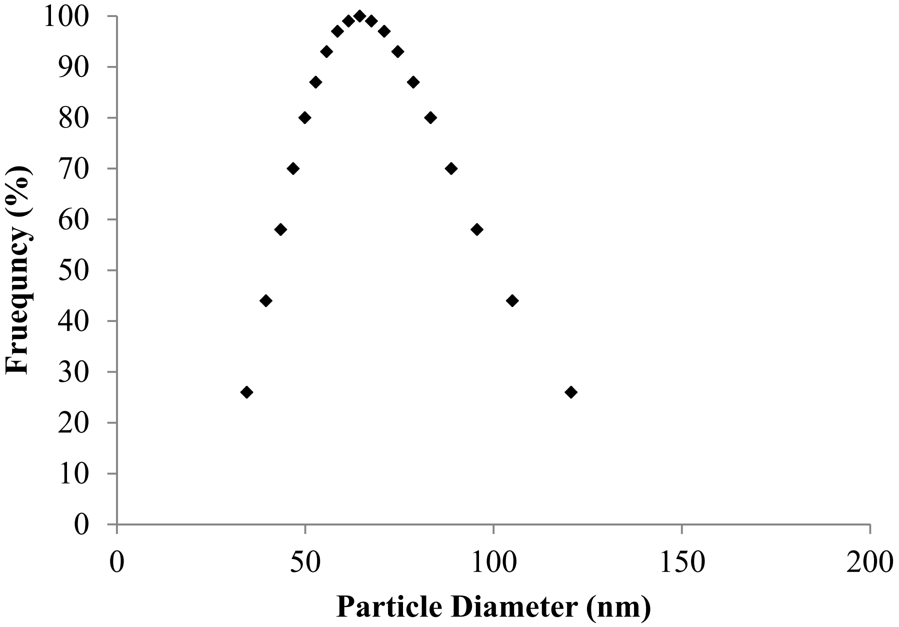

Figure 5.6 Differential distribution for 57 nm particle suspension

5.2.2 Zeta potential measurements

Zeta potential measurements were made to determine the average surface charge of the particles. The average surface charge directly controls the electrostatic interaction between particle and porous medium surfaces. The measurement parameters were consistent for each of the zeta potential measurements performed. Table 5.8 provides the measurement parameters of the zeta potential measurement for the 510 nm particles. For each ionic strength value used in the experiments, Table 5.9 presents the corresponding zeta potential of the particles and relative residual of the data. The relative residual is a dimensionless value characterizing the fitted data.

Table 5.8 Zeta potential measurement parameters for 510 nm particle suspensions

Parameter	**Value**
pH	6.90
Temperature (°C)	25.0
Liquid	Water
Viscosity (cP)	0.890
Refractive Index	1.330
Wavelength (nm)	658.0

Table 5.9 Zeta potential measurement results for 510 nm particle suspensions

Ionic Strength (mM NaCl)	**Zeta Potential (mV)**
0	-45.37
3	-45.13
10	-46.10
20	-45.08
50	-38.10
70	-37.68
100	-32.09
200	-23.72
300	-24.49
400	-24.79

The zeta potentials of the particles were negative at the experimental pH (6.95±1) for all of the solution chemistries. A graphical representation of the data from Table 5.9 is provided in Figure 5.7. As the ionic strength of the monovalent salt solution increases, the zeta potentials become less negative until appearing to plateau somewhere in the ionic strength range of 100-200 mM NaCl, at approximately -25 mV. The decrease in zeta potential resulting from the increased ionic strength is attributed to electric double layer compression [29]. Several previous studies [34] have shown the interactions between particles and grain surfaces are electrostatic in origin. The zeta potential data can be used to analyze the interaction energies between particles and glass bead surfaces, and thus provide a better understanding of the transport and retention of particles in porous media.

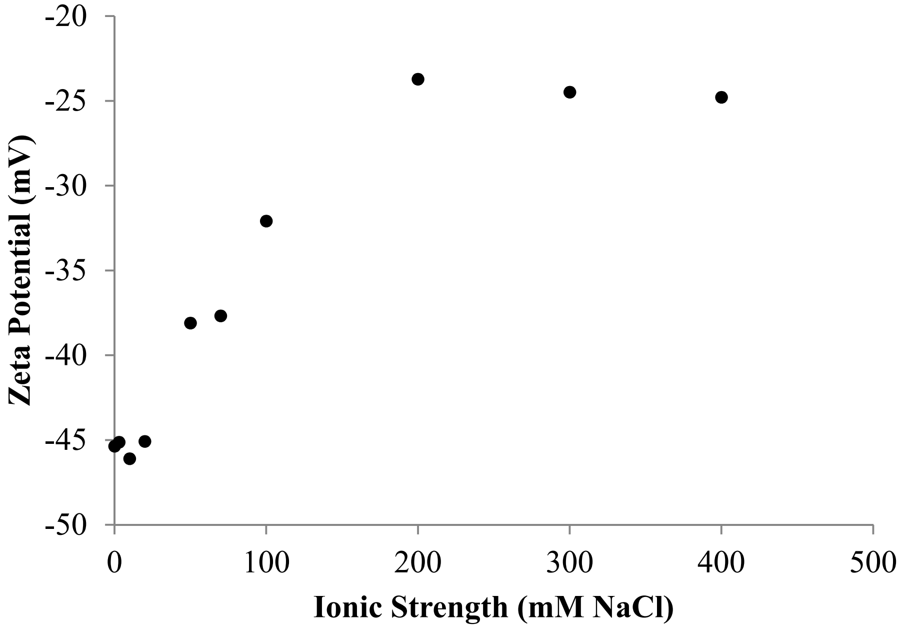

Figure 5.7 Zeta potential measurement results for 510 nm particle suspensions

The zeta potential measurements also provide the EPM, or mobility for each particle suspension. Mobility is defined as the average velocity that the particles in suspension would maintain in an electric field of 1 V/cm. Figure 5.8 provides the graphical representation of the mobility data measured during the 510 nm particle zeta potential measurements. Conductance was also measured during the zeta potential measurements and the graphical results of the conductance measurements are shown in Figure 5.9.

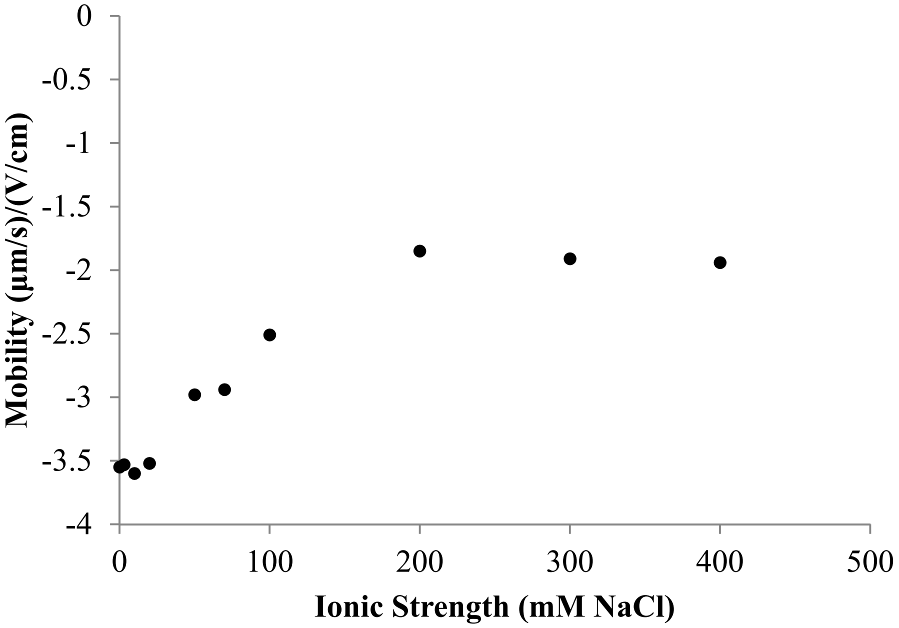

Figure 5.8 Mobility measurement results for 510 nm particle suspensions

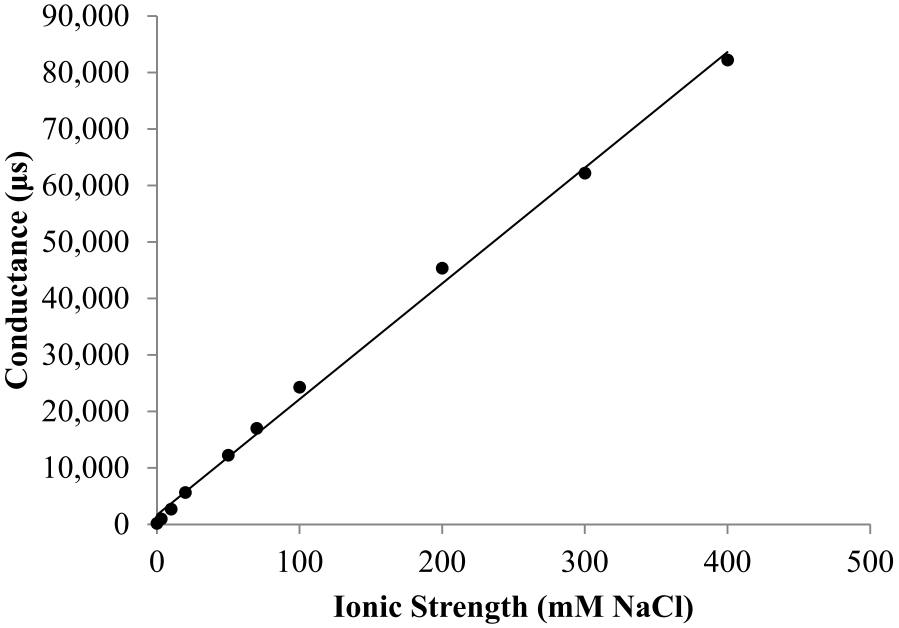

Figure 5.9 Conductance measurement results for 510 nm particle suspensions

Zeta potential measurements for the 210 nm and 57 nm particles were also performed for suspensions in DI water and 3 mM NaCl. The more in-depth zeta potential analysis was only done for the 510 nm particles. The zeta potential data for each of the three particle sizes at the two solution chemistries is presented in Table 5.10.

Table 5.10 Zeta potential measurements for each size particle in DI water suspensions and 3 mM NaCl suspensions

Diameter (nm)	**Zeta Potential (mV)**	
	DI Water	**3 mM NaCl**
510	-45.37	-45.13
210	-41.40	-43.99
57	-40.49	-41.83

5.2.3 Summary of particle characterization results

The following conclusions may be drawn based on the results of the particle size distributions and zeta potential measurements:

1. Particle size distributions measured for each of the three particle sizes are generally in agreement with the diameters provided on the manufacture's product data sheet.
2. Results of the zeta potential measurements for each of the three particles sizes are very close in value at the experimental solution chemistry. This consistency between the different particle sizes used in this study allows the influence of zeta potential to be ignored, simplifying the scenario and allowing for the investigation of the influence of particle size on retention.
3. The selected range of particle sizes, generally from 50 nm to 500 nm, reflects the typical range of engineered nanomaterial aggregate sizes [35]. Zeta potential measurements for particles suspendered in DI water and varied ionic strengths are in the same range of reported zeta potential values as engineered nanomaterials [36]. Thus, the behavior of the selected particles is assumed representative of the behavior of common engineered nanomaterials.

5.3 Conversion of Laser Scanning Cytometer Data

5.3.1 Laser Scanning Cytometer typical data

The output file from an LSC scan provides several different types of data. Table 5.11 shows data for the first 25 events recorded during a sample LSC scan.

Table 5.11 Typical data from Laser Scanning Cytometer scan output file

#	x	y	Area (µm^2)	Integral	Max Pixel
1	31905	10877	99	590146	3226
2	31986	10873	14	48593	1342
3	31781	10983	140	845170	4585
4	31810	10947	90	383388	2440
5	31880	10932	301	1395040	3037
6	31885	10909	40	149229	1757
7	31892	10905	62	269608	2172
8	31915	10954	905	4375779	4294
9	31919	10916	565	2859840	3648
10	31921	10889	39	149843	1591
11	31942	10947	67	350327	2720
12	31947	10991	230	899032	2425
13	31948	10939	11	26053	798
14	31960	10891	23	105106	2029
15	31960	10960	570	2301100	2128
16	31964	10909	888	4357598	3413
17	31965	10999	24	73347	1249
18	31967	10978	16	38126	841
19	31978	10943	149	641945	2283
20	31984	10924	22	85452	1821
21	32069	10879	198	717917	2443
22	32072	10869	26	83236	1728
23	32006	10960	30	93118	1285
24	32027	10955	51	149384	1382
25	32051	10922	403	1680850	3327

The first column, labeled with a number sign, gives the reference number of the recorded event. The event labeled with the number one (1) is the first event recorded during the LSC scan. This should not be confused as representing a single particle, but rather an event within a threshold contour defined by the user. If several particles are close enough in proximity, a single contour may enclose all of the particles resulting in multiple particles represented as a single event.

The second and third columns in Table 5.11 provide the position data for the recorded event. The second column represents the x-position of the contouring channel based on the centroid of the event. The third column gives the recorded event's y-position of its centroid. The values are given in the software's predefined coordinate system which is relative to the stage's home position. These coordinates are later converted to a new coordinate system in which the rightmost side of the flow channel inlet is the origin, flow is in the x-direction and the units are millimeters. The formulas for converting the coordinates are as follows:

$$x_{new} = (62{,}750 - x_{LSC})/1000$$

$$y_{new} = (15{,}250 - y_{LSC})/1000$$

The fourth column in Table 5.11 provides the area in square microns as determined by the threshold contour. The fifth column lists the integral for the recorded event. The integral value is the total amount of fluorescence. As depicted in Figure 5.10, the values for area and integral of a recorded event show a statistically linear correlation relationship.

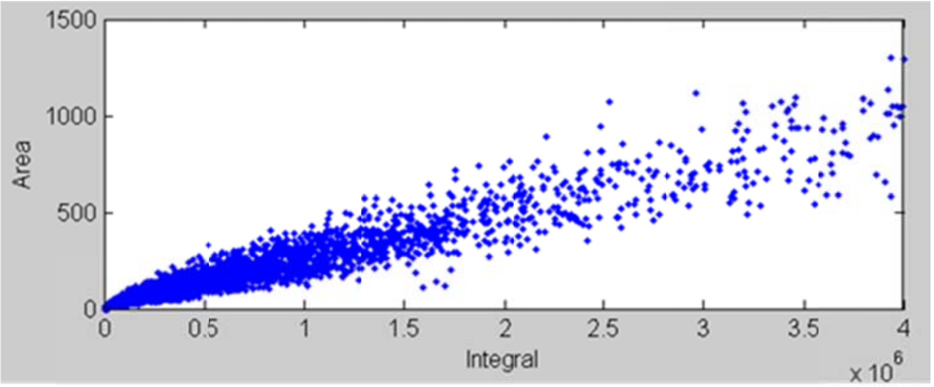

Figure 5.10 Graph of area vs. integral data for sample Laser Scanning Cytometer scan

The final column in Table 5.11, column 6, provides the maximum pixel value, or the highest intensity of fluorescence within the threshold contour, for the recorded event. This value can be anywhere from 0 to 16,384, as defined by the software. A value of 16,384 represents an event in which at least one of the pixels within the threshold contour reached its maximum intensity, or saturation. The variation in maximum pixel values is due to particles absorbing varying amounts of fluorescence as well as some particles being more or less in focus than other particles during the scan due to a third dimension being present within the flow cell.

5.3.2 Converting area data to number of attached particles

In order to estimate the number and location of particles attached within the scan area of the flow cell, a method for converting the data provided by the LSC to a particle count is required. Both area and integral were considered as possible data sources that could be useful to quantify the attachment. It was determined that using integral data would be difficult because of the large variation in maximum pixel values resulting from some particles scanning very intensely while others scanned much less so. This may have been a result of various particles absorbing an unequal amount of fluorescence as well as some particles being more focused within the scan area than others. Thus, area data is used to quantify the number of attached particles.

The first step in using area data to quantify the number of particles attached for a specific experiment is to create a histogram of the area data. For each of the three particles sizes, the peak value of the area histogram is consistent. For the 510 nm particles, the peak occurs at an area value of 18 as shown in Figure 5.11. Figure 5.12 and Figure 5.13 show the peak occurs at an area value of 12 for both the 210 nm and 57 nm particles, respectively. Because of the magnitude of the zeta potentials measured for the particle suspensions at each of the ionic strengths, as well as the particle size distribution measurement results, it is expected that little or no aggregation occurred. That being said, it is believed that the consistent peaks on the area histograms occurred because the event captured a single particle, which is the most common occurrence expected within the flow cell. In some cases, much larger areas were captured by a single event. This is likely a result of particles attaching in close enough proximity that they were captured within the same threshold contour.

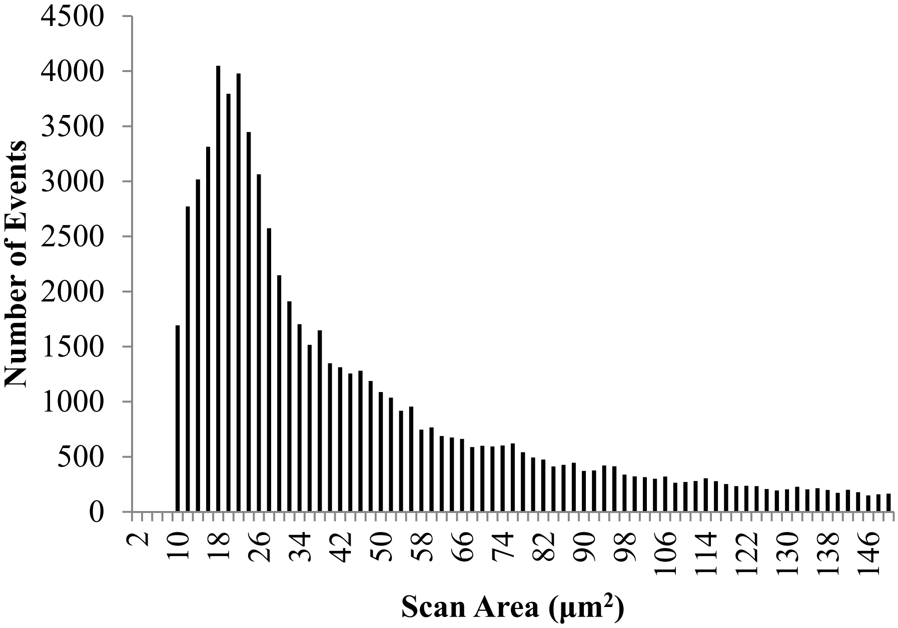

Figure 5.11 Area histogram for sample 510 nm particle flow cell experiment

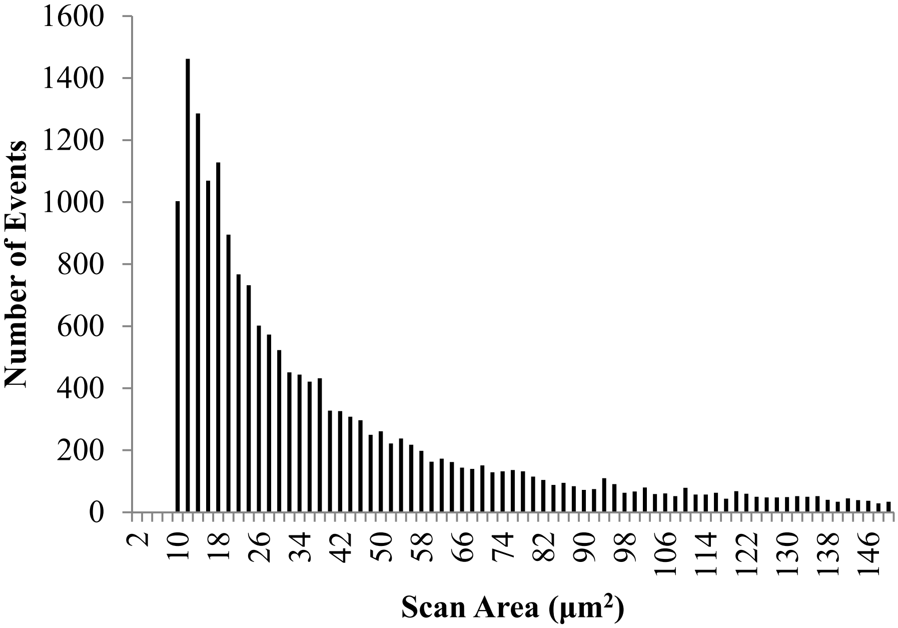

Figure 5.12 Area histogram for sample 210 nm particle flow cell experiment

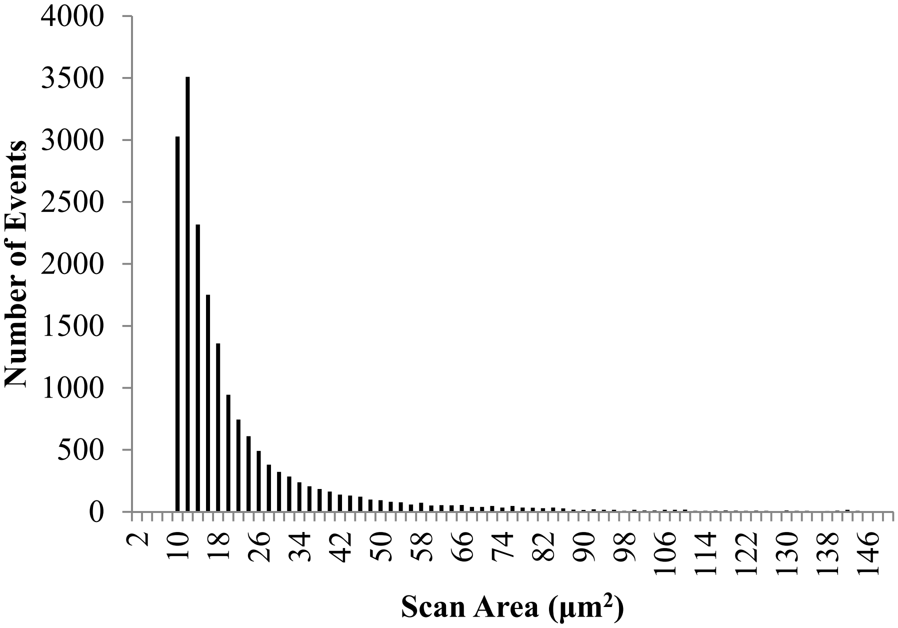

Figure 5.13 Area histogram for sample 57 nm particle flow cell experiment

The second step in converting the area data to the number of particles attached is to determine how much of the data to accept. During an LSC scan, some events capture background noise and/or other disturbances which at times cover a significantly large area; therefore, a method was developed for eliminating the events corresponding to an area representing more than 15 particles, selected arbitrarily. For the 510 nm particles, an individual particle was determined to be represented by an area of 18; 15 particles is thus represented by an area of 270. The result is to eliminate all events within the dataset that have an area greater than 270. For the 510 nm particle flow cell experiments, this eliminates an average of 6.4% of the data from each experiment. An area of 12 was determined to represent an individual particle for the 210 nm and 57 nm particles, and thus an area of 180 represents 15 particles. The same process of eliminating all of the events within the dataset that have an area greater than 180 was used for all of the experiments at these particle sizes. This eliminates an average of 8.3% of the data from each flow cell experiment for the 210 nm particles and 4.3% of the data for 57 nm particle flow cell experiments.

5.3.3 Spatial distributions of attached particles

One method of data analysis is to develop spatial distributions of the attached particles. The previous section covered the method developed for converting the area value measured for each recorded event to the number of attached particles each event represents. It also described a method for eliminating data determined to not represent particle attachment. The LSC data for each event has a corresponding x- and y-position which is converted to a coordinate system as defined earlier. Using the data for the number of attached particles as well as the position data, MATLAB is used to create a figure showing the spatial distribution of attached particles within the scan area for each flow cell experiment. The y-axis represents the y-position of the recorded event in millimeters and the x-axis represents the x-position of the event in millimeters. Each event is represented by a single dot on the spatial distribution, all of which are the same size; however, the number of attached particles a specific dot represents is defined by the color bar. The color bar defines which colors correspond to each number of attached particles. Figure 5.14 provides a spatial distribution of attached particles for a sample flow cell experiment. For this figure, the color bar maximum is 4 attached particles to better show the effectiveness of the color bar for distinguishing more concentrated areas of attached particles. The elliptical appearance of the spherical glass beads is due to the stretching of the y-axis compared to the x-axis.

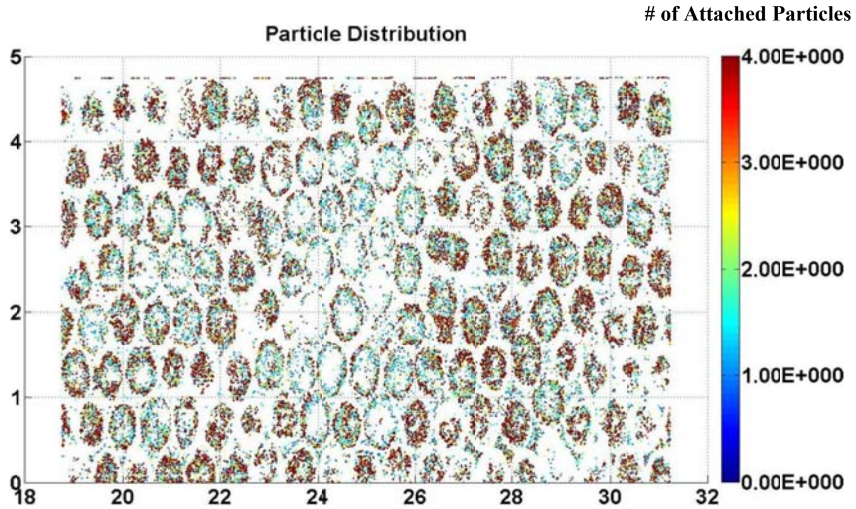

Figure 5.14 Spatial distribution of attached particles for a sample flow cell experiment

5.4 Flow Cell Experiment Results Analysis

5.4.1 Influence of particle size

The influence of particle size on mobility has been investigated in earlier studies in the colloidal science, with debatable conclusions. An early study [37] showed no differences in the attachment kinetics of different size latex particles (46-753 nm); however, a later study for particles with 245 nm to 755 nm sizes found increased attachment for larger size particles [38]. A recent study [28] compared different size particles (from 50 nm to 1500 nm) and found that the smallest particles exhibit the lowest degree of retention. None of these studies, however, agree with the classic filtration theory. Classic filtration theory predicts an increase of attachment when particle sizes are decreased in the submicron range.

Because of these inconsistencies, experiments were conducted to investigate the influence of particle size on attachment. Figure 5.15 shows spatial distributions of attached particles for each of the three particle sizes under the same experimental conditions (0.08 cm/s, 3mM NaCl, 40 PV). Duplicates are labeled (a) and (b). Figure 5.16

provides the number of attached particles in the scan area corresponding to these experiments.

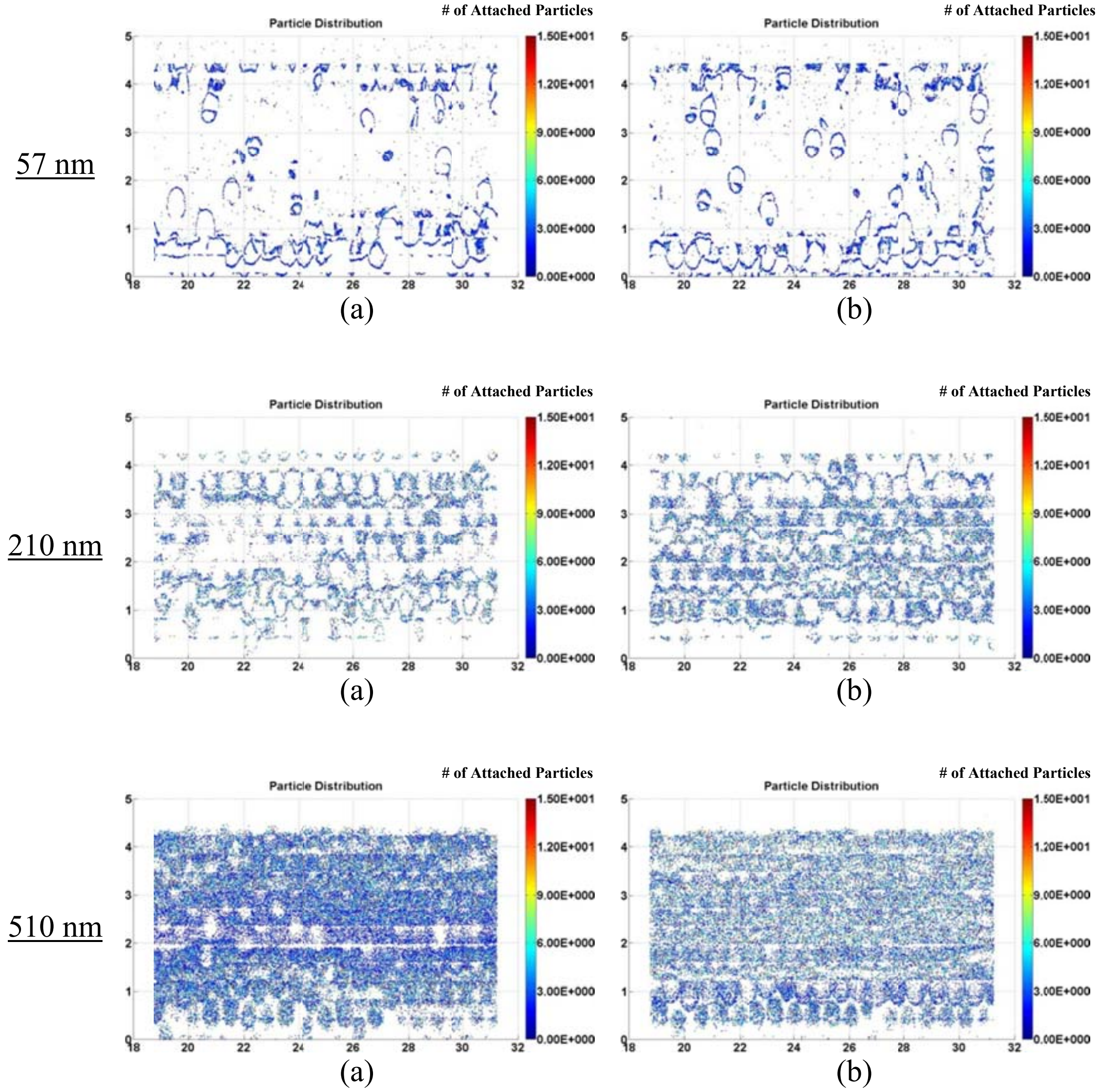

Figure 5.15 Spatial distributions of attached particles for flow cell experiments investigating the influence of particle size (0.08 cm/s, 3 mM NaCl, 40 PV)

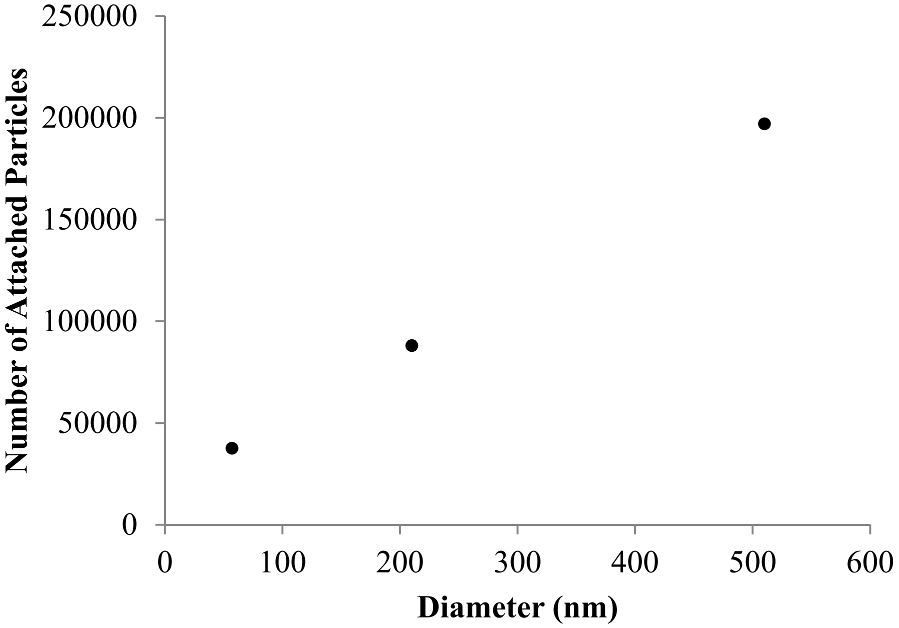

Figure 5.16 Influence of particle size on attachment (0.08 cm/s, 3 mM NaCl, 40 PV)

Based on Figure 5.15 and Figure 5.16, it is clear that the number of attached particles decreased with decreased particle size, consistent with Pelley and Tufenkji [28]. After 40 PV of injection at the same experimental conditions, only 37, 684 attached particles were measured in the scan area for the 57 nm particles, compared to 197,063 and 88,123 attached particles measured in the scan area for the 510 nm and 210 nm particles, respectively. It is difficult to explain why significantly less attachment was observed for the smaller particles. According to the classic filtration theory, 57 nm particles will have a higher η_0 compared to the two larger size particles due to enhanced diffusion processes. Because each of these particles have comparable surface potentials, it is reasonable to expect the highest attachment for the 57 nm particles because they have the highest η_0. The observation from this study is obviously in contradiction with the classic filtration model predictions. Considering this finding is consistent with the column-scale study by Pelley and Tufenkji [28], a group with excellent credibility on colloidal science research, more effort was devoted to comparing the behaviors of the three different size particles under varied injection duration, solution chemistry, solids content and Darcy velocity.

At this point, it is appropriate to acknowledge a possible technical issue related to LSC scanning. In Figure 5.17, there appears to be regions of reduced attachment occurring along the flow channel walls for the experiments using 510 nm and 210 nm particles; however, less attachment is unexpected in these areas compared to that of the center of the flow channel. What appears to be minimal attachment occurring could actually be a result of the LSC threshold contour failing to distinguish an event due to the area being oversaturated with fluorescence. This oversaturation results in the intensity never dipping low enough for a threshold contour to occur and account for the particles attached in these regions. Because it represents a relatively small portion of the scan area, it is believed that the results and trends are still statistically valid.

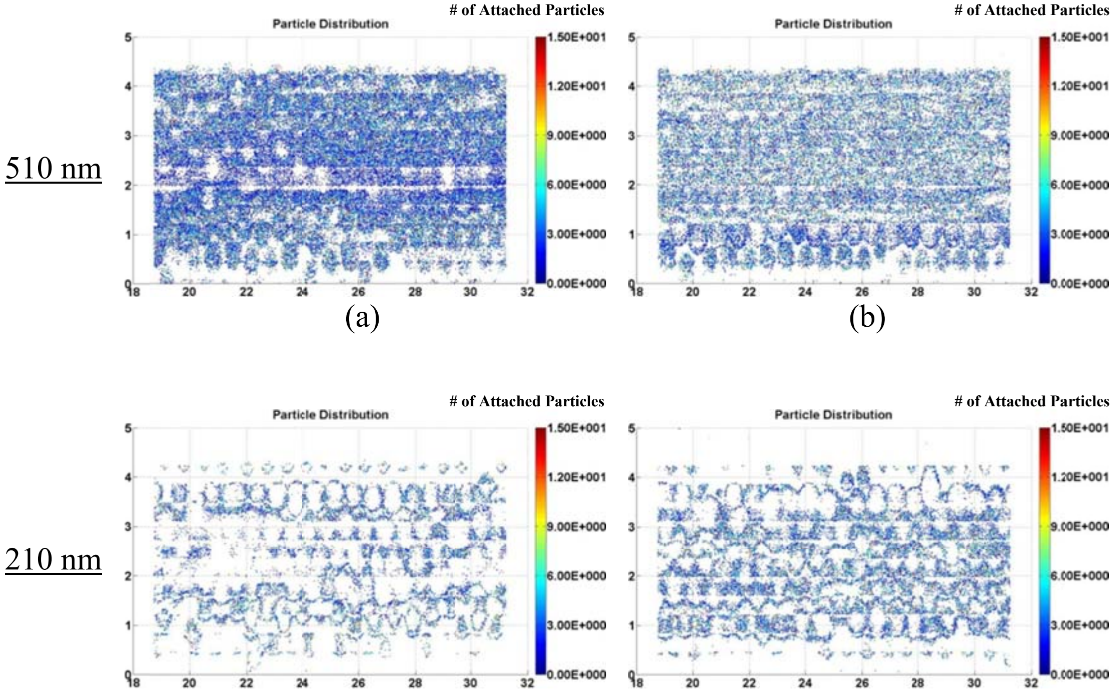

(a) (b)

(a) (b)

Figure 5.17 Spatial distributions of attached particles for flow cell experiments (0.08 cm/s, 3 mM NaCl, 40 PV)

5.4.2 Influence of injection duration

Different injection durations for suspensions of 510 nm and 57 nm particles at two different Darcy velocities were used to investigate the influence of injection duration on attachment. The purpose is to compare the attachment styles of different size particles to available theories. Specifically, if the attachment follows classic filtration theory [18], the number of attached particles should increase exponentially as injection duration is increased. On the contrary, if the attachment follows an S_{max} model [21], the number of attached particles will stop increasing with increased injection duration after the glass bead surfaces reach maximum capacity.

The solids content for these experiments was 0.0025% and the ionic strength was 3 mm NaCl. Darcy velocities of 0.08 cm/s and 0.04 cm/s were used with a combination of 40 PV, 120 PV, 240 PV and 300 PV injection durations. Regardless of the duration that the particle suspension was injected, the rinse performed was always 5 PV for these experiments. Figure 5.18 provides a graphical representation of the results from the flow cell experiments investigating the influence of injection duration on attachment using 510 nm particles.

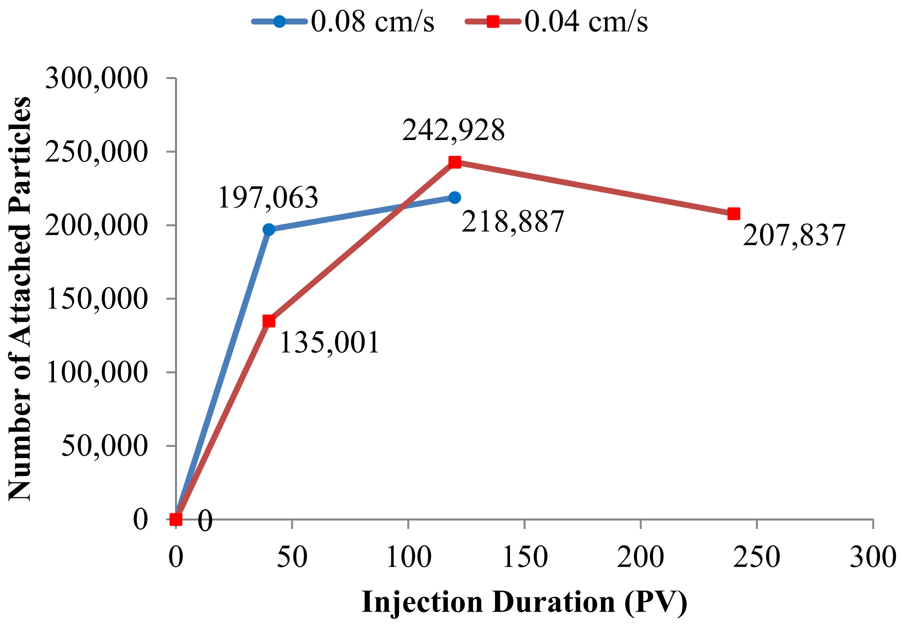

Figure 5.18 Influence of injection duration on attachment using 510 nm particles

For the 510 nm particles, the flow cell experiment in which the injection duration was tripled 40 PV to 120 PV at 0.08 cm/s only results in roughly a 10% increase in attachment. At 0.04 cm/s, the increase in injection duration from 40 PV to 120 PV for the 510 nm particles results in approximately an 80% increase in attachment; however, an increase in injection duration up to 240 PV actually results in less attached particles compared to that of the 120 PV experiment. This decrease coupled with the only slight increase from 40 PV to 120 PV at 0.08 cm/s indicates a likely S_{max}. In examining the graphical results, it appears S_{max} for the 510 nm particles under these experimental conditions is between 200,000 and 250,000 particles within the scan area.

The spatial distributions of the flow cell experiments investigating the influence of injection duration on attachment for the 510 nm particles at 0.08 cm/s and 0.04 cm/s are presented in Figure 5.19 and Figure 5.20, respectively. It appears more attachment occurs within the center regions of the flow channel with the increased injection durations.

40 PV

120 PV

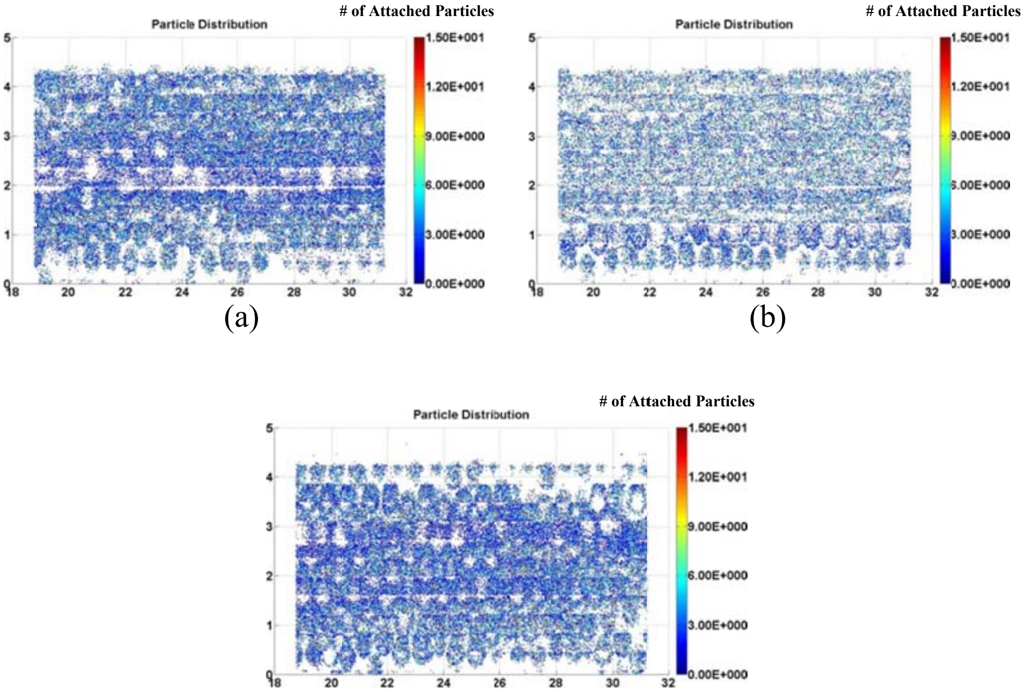

(a) (b)

Figure 5.19 Spatial distributions of attached particles for flow cell experiments investigating the influence of injection duration using 510 nm particles and 0.08 cm/s Darcy velocity

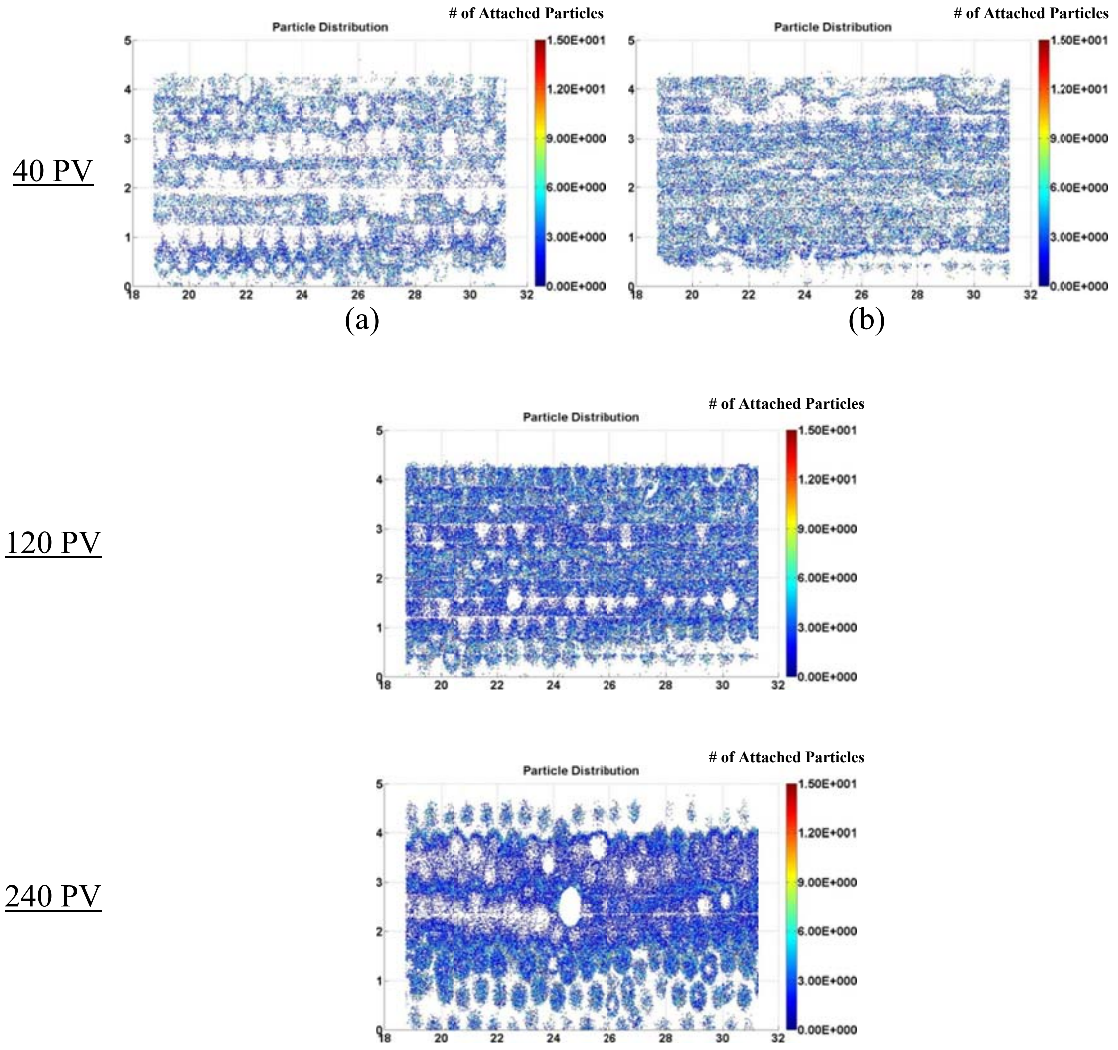

Figure 5.20 Spatial distributions of attached particles for flow cell experiments investigating the influence of injection duration using 510 nm particles and a Darcy velocity of 0.04 cm/s

The influence of injection duration on attachment for 57 nm particles was investigated at 0.08 cm/s Darcy velocity. The graphical representation of the results is presented in Figure 5.21 and the spatial distributions for the flow cell experiments are shown in Figure 5.22.

As the injection duration increases, more attachment occurs; however, the rate of increasing attachment decreases with increasing injection duration. Overall, less than 65% additional attachment occurs as injection duration is increased from 40 PV to 300

PV. For this experiment, attachment increases 40% as injection duration increases from 40 PV to 120 PV. Attachment only increases less than 20% as injection duration increases from 120PV to 300 PV. Significant increases in injection duration only lead to moderate increases in attachment indicating that the attachment of 57 nm particles fails to follow classic filtration theory. The fact that the rate of attachment slows down as injection duration increases may indicate the particles previously attached to glass bead surfaces may block available sites for subsequent attachment. While the blocking effect is obvious, experiments with longer injection durations may be necessary to identify if S_{max} behavior is shown by 57 nm particles.

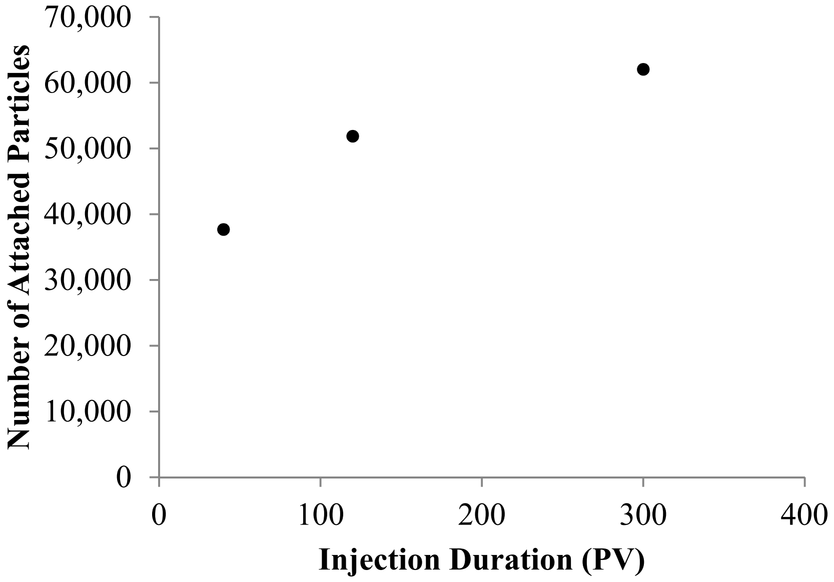

Figure 5.21 Influence of injection duration on attachment using 57 nm particles and a Darcy velocity of 0.08 cm/s

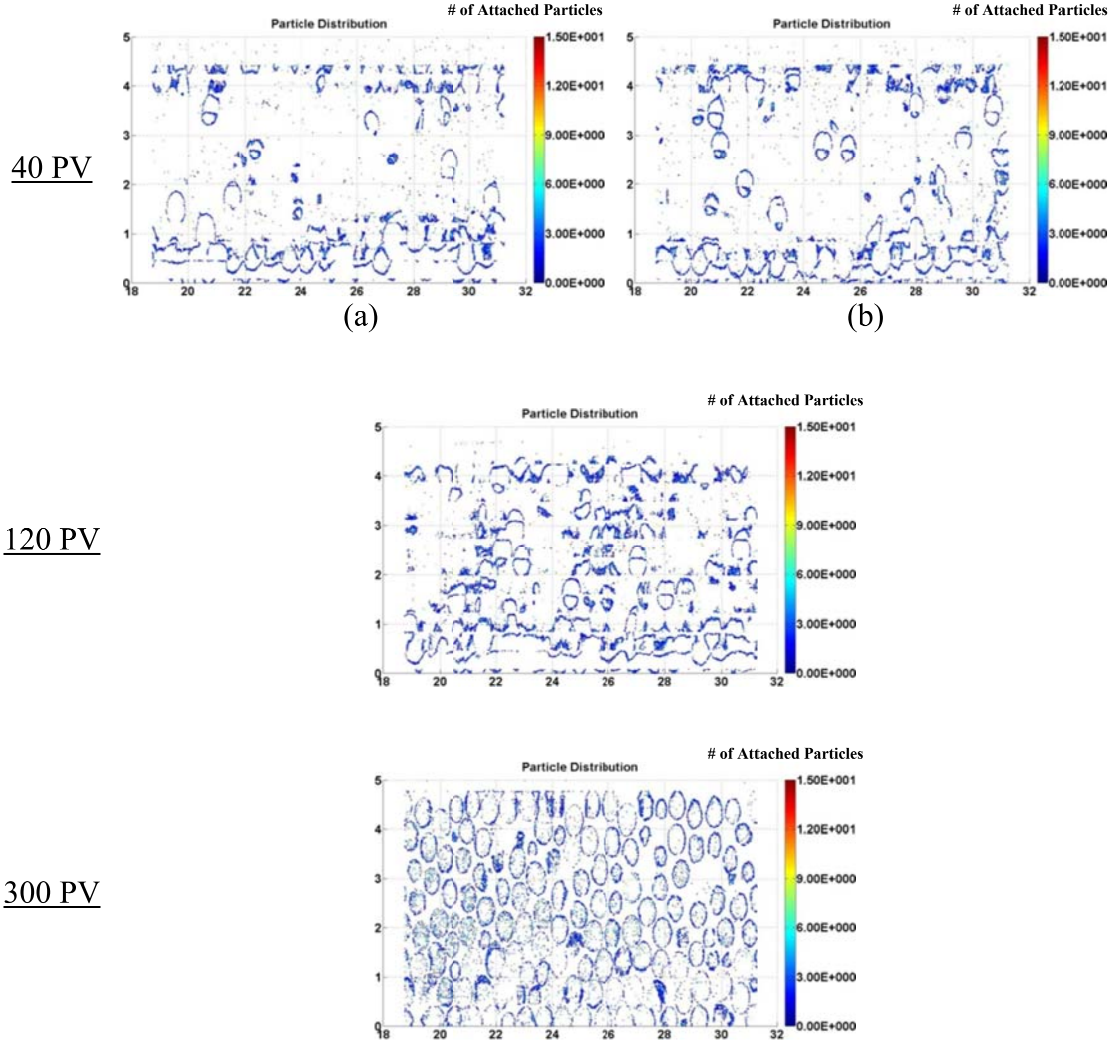

Figure 5.22 Spatial distributions of attached particles for flow cell experiments investigating the influence of injection duration using 57 nm particles and a Darcy velocity of 0.08 cm/s

5.4.3 Influence of solution chemistry

Two additional flow cell experiments were conducted to investigate the influence of solution chemistry on attachment for the 510 nm and 57 nm particles. In these experiments, 40 PV of particle suspension was first injected, followed by 5 PV of background solution (i.e. 100mM NaCl). At this point, an initial LSC scan was performed followed by a 5 PV injection of DI water and a subsequent LSC scan. The solids content used for these experiments was 0.0025% and the Darcy velocity was 0.04 cm/s. The ionic strength of the particle suspension and background solution was 100 mM NaCl. The graphical results for the 510 nm and 57 nm experiments are presented in Figure 5.23 and Figure 5.24, respectively. The spatial distributions for the flow cell experiments investigating the influence of solution chemistry for the 510 nm and 57 nm particles are presented in Figure 5.25 and Figure 5.26, respectively.

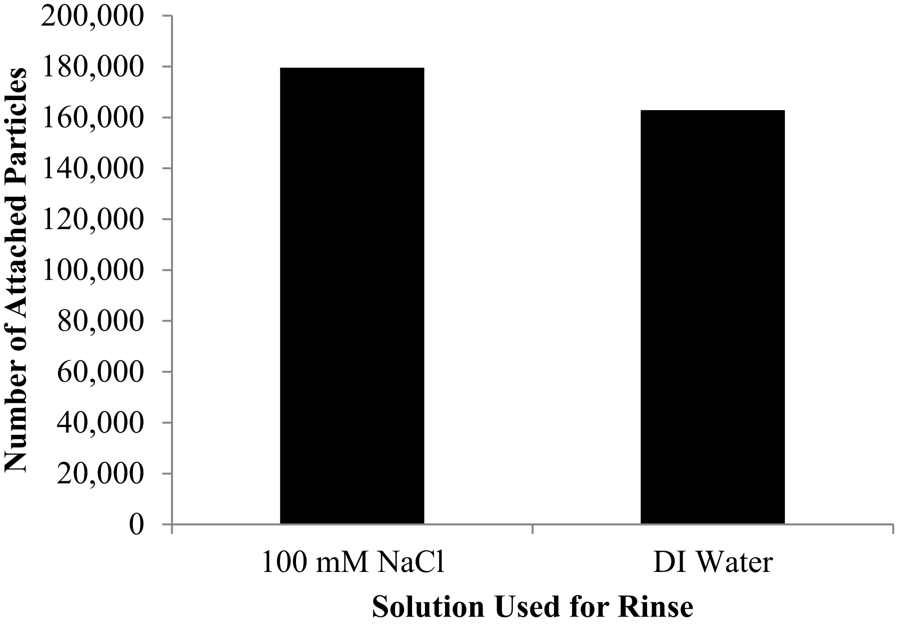

Figure 5.23 Influence of solution chemistry on attachment using 510 nm particles

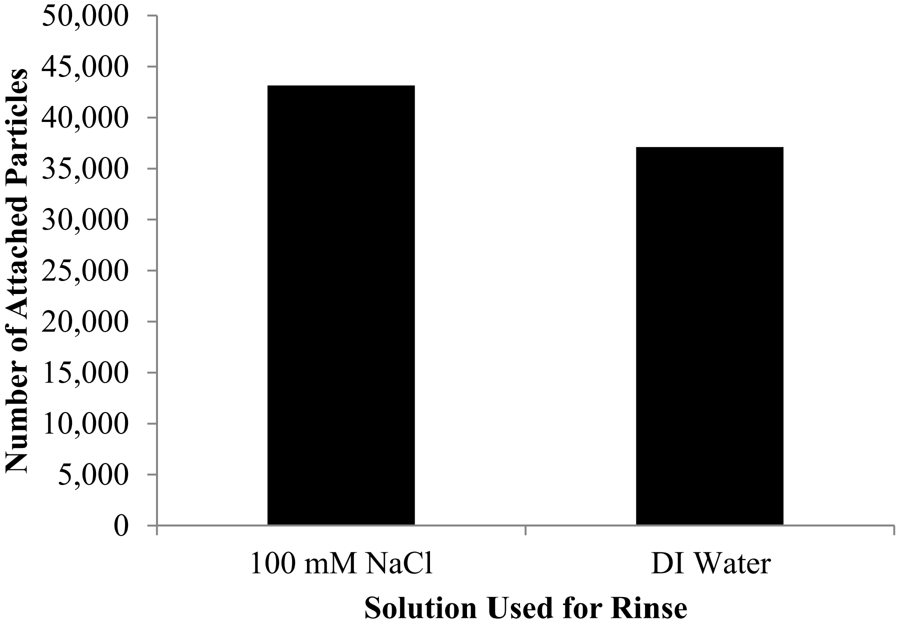

Figure 5.24 Influence of solution chemistry on attachment using 57 nm particles

<u>100 mM NaCl background solution rinse</u>

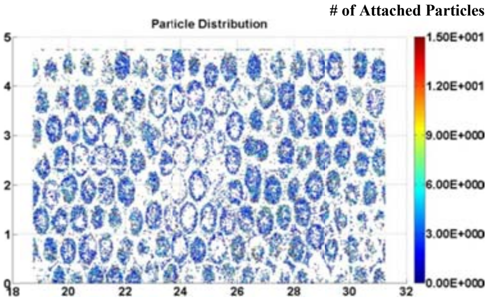

<u>DI water rinse</u>

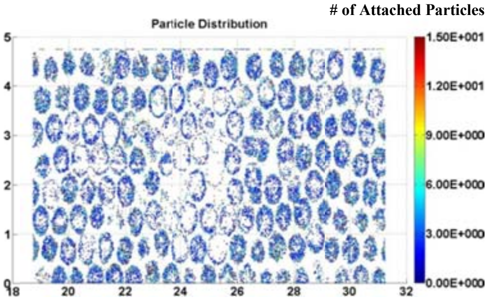

Figure 5.25 Spatial distributions of attached 510 nm particles for flow cell experiment investigating the influence of solution chemistry on attachment

<u>100 mM NaCl background solution rinse</u>

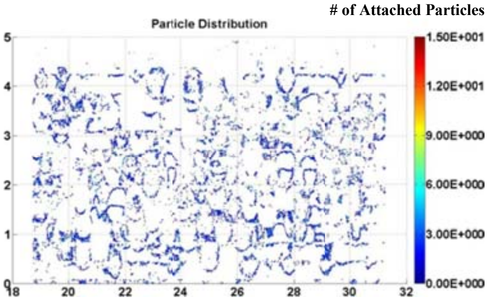

<u>DI water rinse</u>

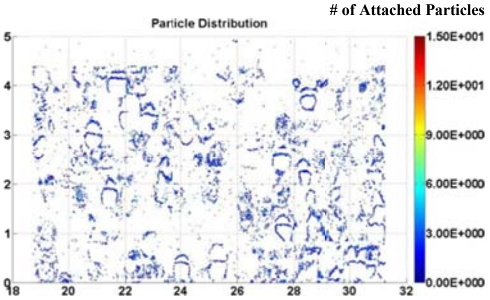

Figure 5.26 Spatial distributions of attached 57 nm particles for flow cell experiment investigating the influence of solution chemistry on attachment

Under the experimental conditions, both particle and glass bead surfaces are negatively charged; thus, net repulsive interactions should exist between particles and glass beads. On the contrary, significant attachment is observed for experiments using both particle sizes. Such a phenomenon is typically referred to as attachment under unfavorable conditions (i.e. particles and porous media surfaces have the same sign of charge) and has been widely reported for colloidal particle and bacteria transport. The mechanisms leading to unfavorable attachment, however, are not well understood. One popular explanation is attachment in the secondary minimum.

As briefly described in Section 2.3.1, the secondary minimum is a small region possessing attractive interaction energy at a greater separation distance than that of the energy barrier. This is attributed to the fact that the van der Waals and electrostatic double layer interactions have different dependencies with respect to separation distance (power-law and exponential, respectively). According to DLVO theory, if the ionic strength in the solution changes to a sufficiently low level, the secondary minimum attractive energy well will disappear. For these experiments to be in agreement with this, the particles attached as a result of the secondary minimum well should release during the DI water rinse. In comparing the spatial distributions of attached particles before and after the DI water rinse, the percentage of particles attached as a result of the secondary minimum should be quantifiable.

For the 510 nm particles, the DI water rinse results in 9.3% of the attached particles removed. The DI water rinse for the 57 nm particles results in 14% of the attached particles removed. These results indicate the secondary minimum may contribution to approximately 10% of the particle attachment. Further, the similar percentage of particles released for both 510nm and 57 nm particles indicates the contribution of the secondary minimum is independent of particle size. These experiments found most (85-90%) particles are attached to glass bead surface due to primary energy minimum. This is consistent with column-scale nC_{60} fullerene transport studies [21]. In that study, surface charge heterogeneity of porous medium surface was considered the reason for primary energy minimum attachment.

5.4.4 Influence of Darcy velocity

The influence of Darcy velocity on attachment was also investigated at several velocities for each of the particle sizes. The solids content for each of these experiments was 0.0025%, the ionic strength was 3 mM NaCl, the pH was 6.95±1 and the injection duration was 40 PV with the standard 5 PV background solution rinse. Darcy velocities of 0.08 cm/s, 0.06 cm/s, 0.04 cm/s and 0.02 cm/s were used and duplicate experiments were performed with the results subsequently averaged. Figure 5.27 provides the graphical results of the Darcy velocity flow cell experiments for all three particle sizes. The spatial distributions of attached particles for the 510 nm, 210 nm and 57nm particle experiments are presented in Figure 5.28, Figure 5.29 and Figure 5.30, respectively.

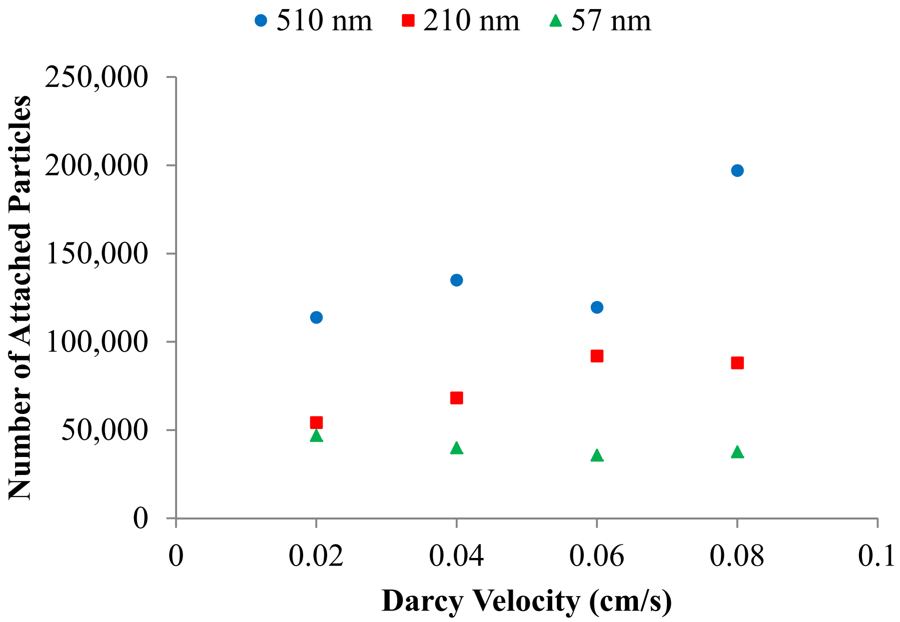

Figure 5.27 Influence of Darcy velocity on attachment

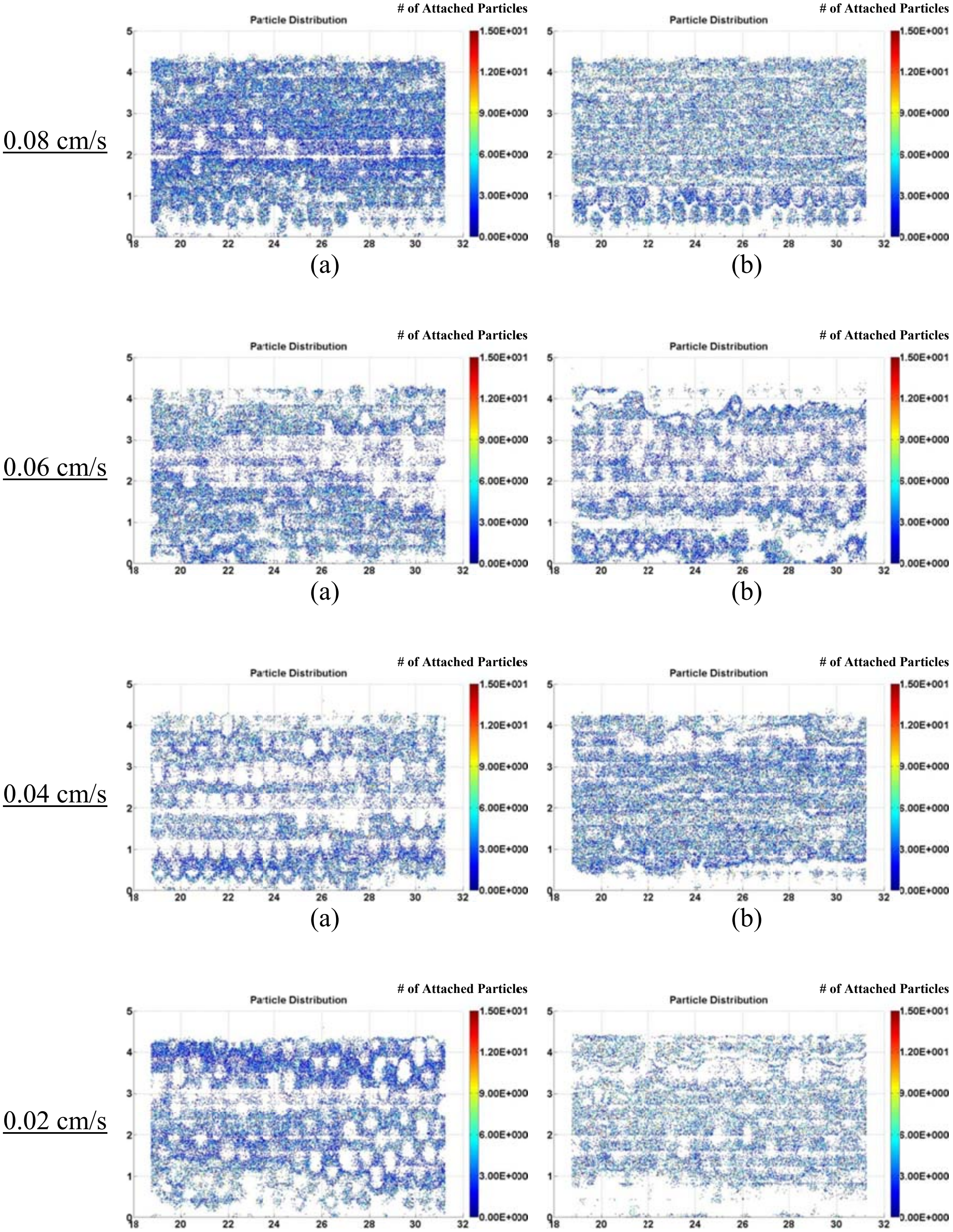

0.08 cm/s

(a) (b)

0.06 cm/s

(a) (b)

0.04 cm/s

(a) (b)

0.02 cm/s

(a) (b)

Figure 5.28 Spatial distributions of attached particles for flow cell experiments investigating the influence of Darcy velocity using 510 nm particles

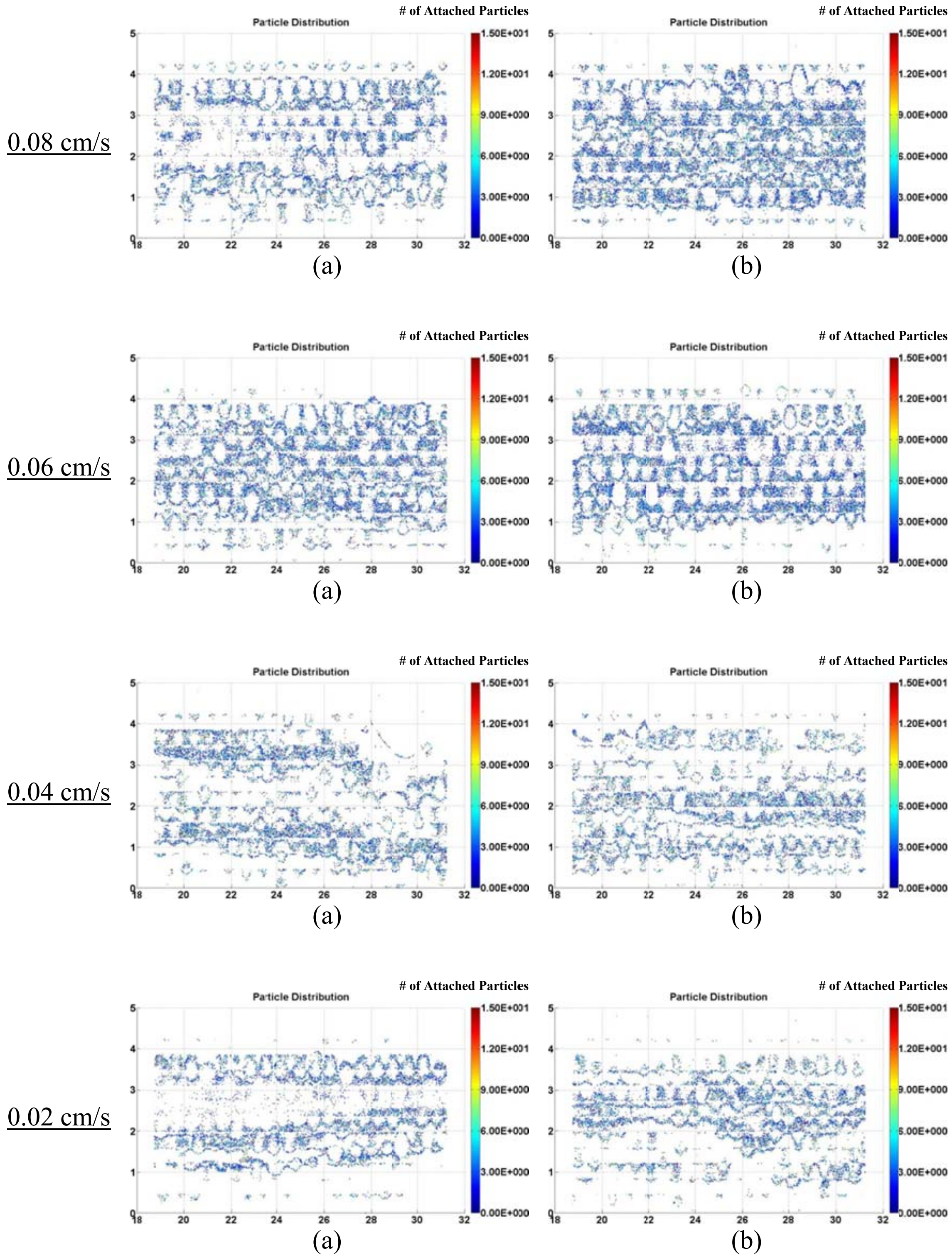

0.08 cm/s (a) (b)

0.06 cm/s (a) (b)

0.04 cm/s (a) (b)

0.02 cm/s (a) (b)

Figure 5.29 Spatial distributions of attached particles for flow cell experiments investigating the influence of Darcy velocity using 210 nm particles

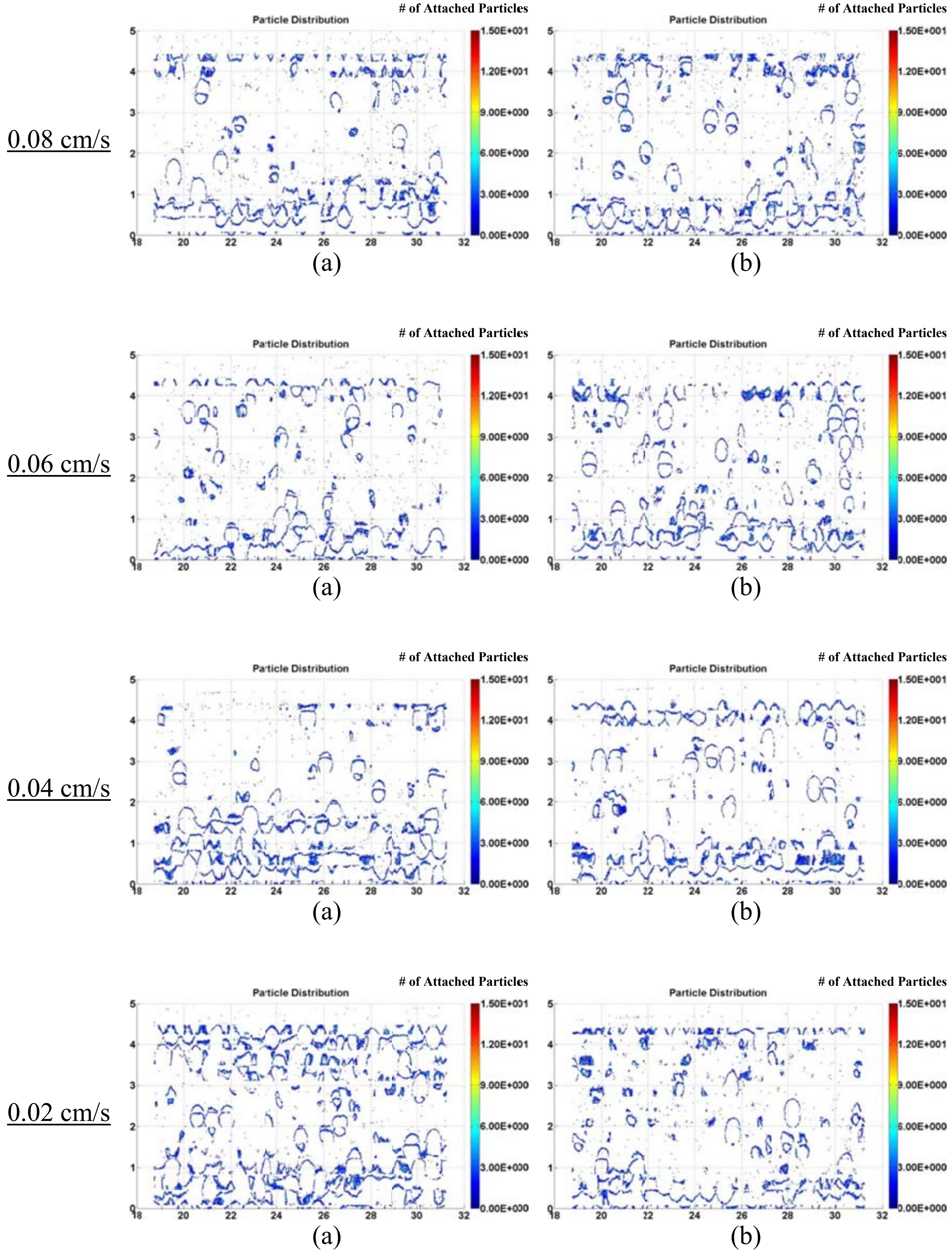

Figure 5.30 Spatial distributions of attached particles for flow cell experiments investigating the influence of Darcy velocity using 57 nm particles

Several unexpected trends are seen in these results. According to Figure 5.27, both of the larger particles (510 nm and 210 nm) exhibit an increase in attachment as the Darcy velocity increases; however, the trend is not clear for the 57 nm particles. Attachment of the 57 nm particles varies only slightly as the Darcy velocity changes and provides no clear indication of increasing or decreasing attachment. These results are inconsistent with a previously published column-scale study [21] in which attachment was found to reduce with increasing Darcy velocity for nC_{60} nanoparticles.

A possible explanation for the unexpected increase in attachment within the scan area as the Darcy velocity increases for the 510 nm and 210 nm particles is the inability to define a scan area containing the inlet of the flow channel due to spatial limitations between the flow cell and fittings and the microscope objective. The results of each LSC scan only reflect a relative number of attached particles within the scan area as opposed to the total number of attached particles in the flow channel. More specifically, it is possible significantly higher attachment is occurring upstream of the scan area near the flow channel inlet resulting in the apparent decrease in attachment in the middle 12.5 mm of the flow channel. This hypothesis can be explained by the observed S_{max} in Section 5.4.2.

As illustrated in Figure 5.27, at the low Darcy velocity (0.04 cm/s), the number of attached 510 nm particles after a 40 PV injection is roughly 135,001. This is about 50-60% of the estimated S_{max} for the scan area (200,000 to 250,000). If S_{max} is unachieved, plenty of available attachment sites are present on the glass bead surfaces near the flow cell inlet. The result is particles attaching preferentially to glass bead surfaces closer to the flow channel inlet, allowing for fewer particles to travel to the scan area in the middle

12.5 mm of the flow cell. The LSC scan is unable to measure the number of particles attaching near the flow channel inlet. This explanation is further supported by experiments with longer injection durations. After a 120 PV injection, the number of attached 510 nm particles increases approximately 80% compared to the number of attached particles after a 40 PV injection experiment with 0.04 cm/s Darcy velocity. On the other hand, the number of attached particles increases roughly 10% for the 510 nm particles when the injection duration increases from 40PV to 120PV with a Darcy velocity of 0.08 cm/s as can be seen in Figure 5.31. In conclusion, the spatial limitation restricting the definition of the scan area results in no sufficient data to show if increasing Darcy velocity leads to increasing or decreasing attachment of 510 nm and 210 nm particles for varying injection durations. It is reasonable, however, to speculate that velocity should not have profound influence on the number of attached particles if sufficiently large injection durations are used based on the fact that observed S_{max} from Figure 5.31 is very similar for 0.04 cm/s and 0.08 cm/s Darcy velocities.

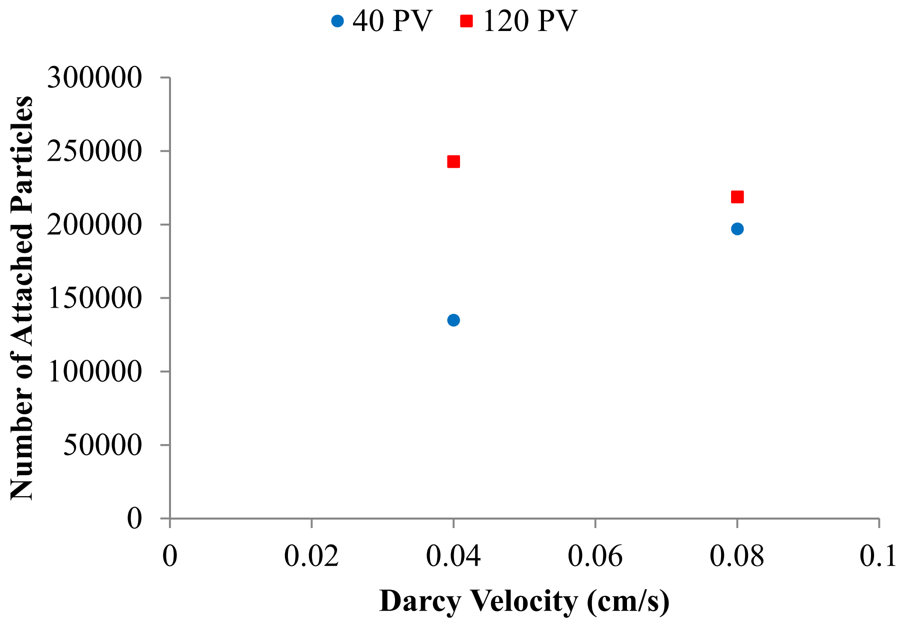

Figure 5.31 Influence of injection duration on attachment for 510 nm particles

A similar explanation explains the relatively flat trend for the influence of the Darcy velocity on 57 nm particle attachment. As illustrated in Section 5.4.2, much less attachment is observed for 57 nm particles compared to larger particles, indicating a lower S_{max}. It is possible that fewer attachment sites are available on the glass bead surfaces for the 57 nm particles near the flow channel inlet allowing more particles to travel downstream; therefore, there is no concern that 57 nm particles accumulate at the inlet as is the case for the larger particles. The relatively flat trend for the influence of Darcy velocity on attachment for the 57 nm particles suggests that transport for the 57 nm particles is dominated by diffusion. This is further confirmed by the spatial distributions presented in Figure 5.30, in which all of the spatial distributions indicate particles are able to attach around the entire surface of the glass beads. Because attachment is possible at the downstream surface areas of the glass beads, it further indicates diffusion is likely the controlling mechanism of attachment.

5.4.5 Influence of solids content

Flow cell experiments investigating the influence of solids content on attachment were also performed. The ionic strength for each of these experiments was 3 mM NaCl, the Darcy velocity was 0.04 cm/s, the pH was 6.95±1 and the injection duration was 40 PV with the standard 5 PV background solution rinse. Solids contents of 0.005%, 0.0025% and 0.0005% were used and duplicate experiments were performed and averaged. Figure 5.32 presents the results of the influence of solids content flow cell experiments graphically for each of the three particle sizes.

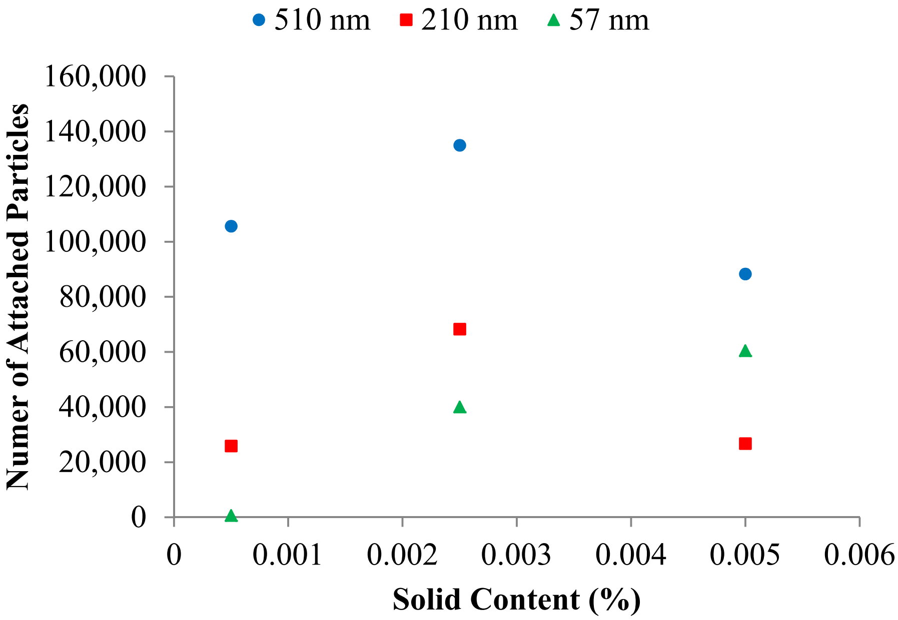

Figure 5.32 Influence of solids content on attachment

The experiments using the two larger particle sizes both display an initial increase and then subsequent drop-off in attachment for the highest solids content. This decrease in the number of attached particles as the solids content increases is counterintuitive. Because a great number of particles are introduced at the higher solids content, it seems logical to expect greater attachment will occur; however, this is not the case. Similar observations were reported for colloidal particle transport at the column-scale [39]. In that study, increasing the input concentration for 3.2 μm and 1.0 μm colloids produced less attachment and higher mass recovery in the effluent.

A possible explanation should consider particle (aqueous) - particle (attached) repulsive interactions. While some particles are already attached onto glass bead surfaces, particles introduced later in the injection may interact with them. This interaction may lead to some attached particles escaping from their attachment sites due to repulsive energy. The frequency of such interactions should be proportional to the particle concentration in solution (i.e. solids content) and the number of attached particles on the glass bead surfaces. If the solids content is not sufficiently high, the number of such interactions is not predominant. This explains the initial increase in the number of attached particles as solids content increases from 0.0005% to 0.0025%; however, it is important to note the number of attached particles is not proportional to the solids content of the injected particle suspension. When the solids content is higher, such interactions are more dominant and lead to a decreasing number of attached particles, as is shown when solids content is increased from 0.0025% to 0.005%.

The spatial distributions of attached particles for the experiments using 510 nm and 210 nm particles at various solids contents are presented in Figure 5.33 and Figure 5.34, respectively.

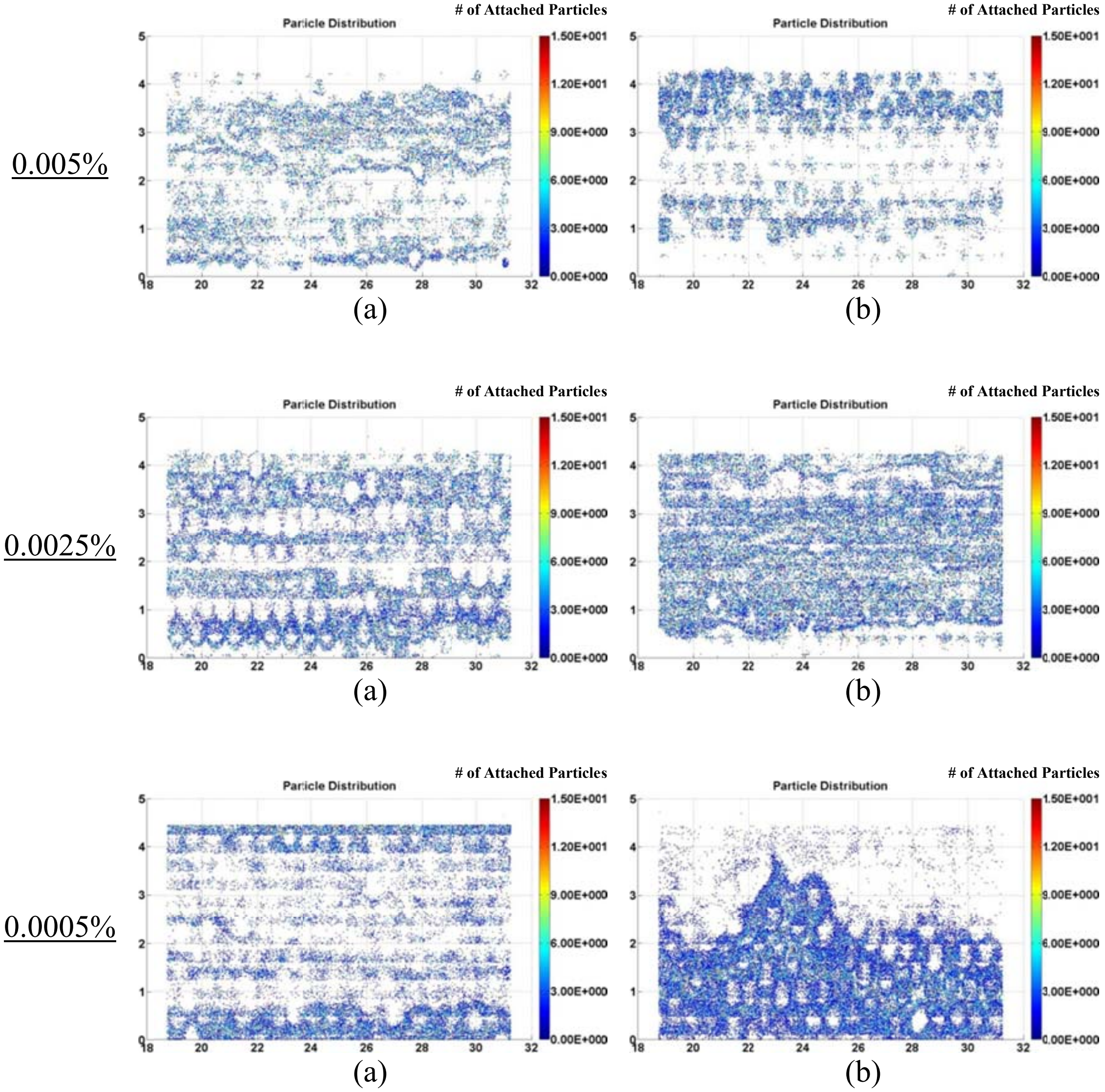

Figure 5.33 Spatial distributions of attached particles for flow cell experiments investigating the influence of solids content using 510 nm particles (note: 0.005% (b) appears to have been out of focus, possibly due to being out of level, which caused a large portion of the scan area to be missed)

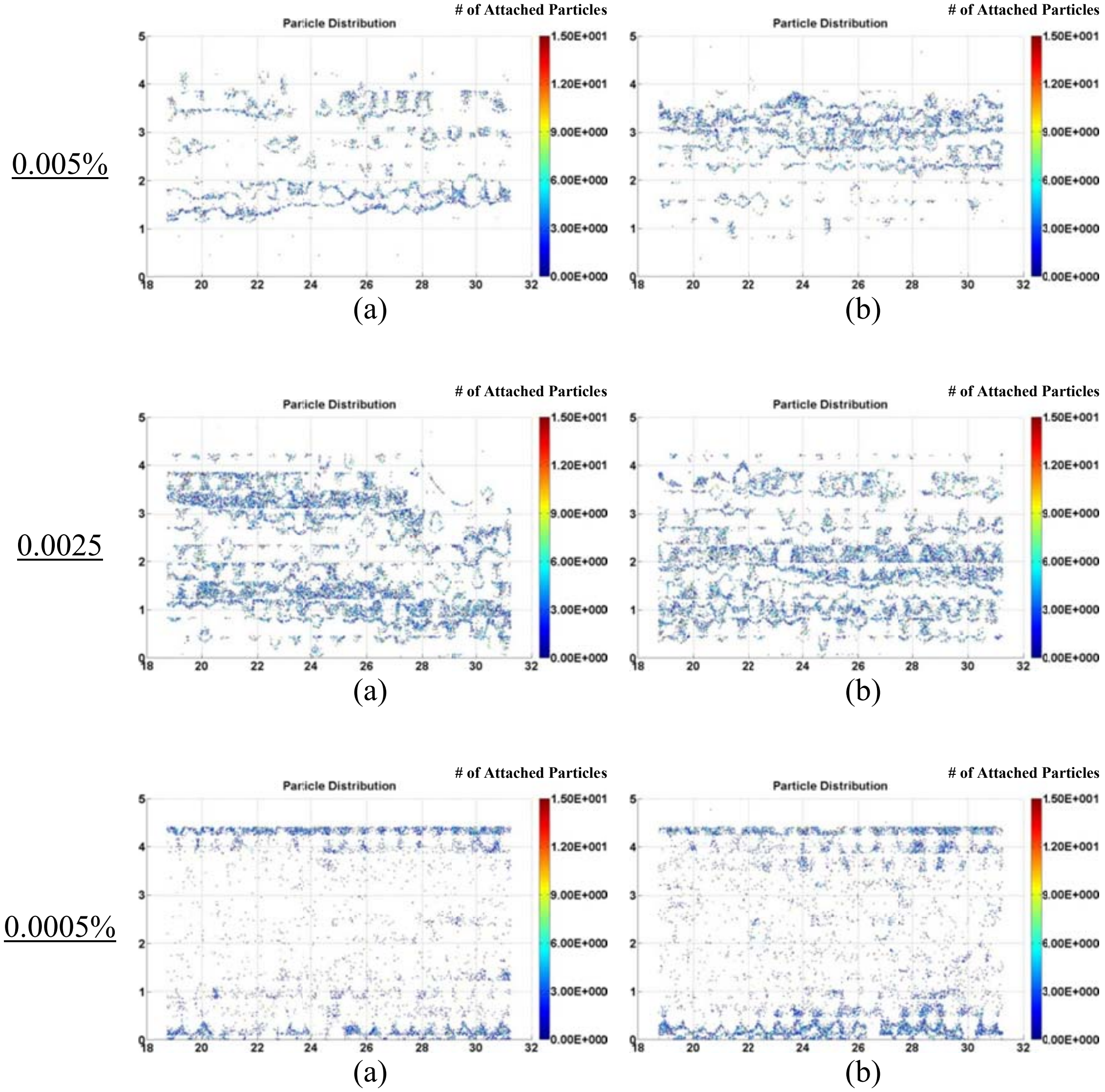

(a) (b)

Figure 5.34 Spatial distributions of attached particles for flow cell experiments investigating the influence of solids content using 210 nm particles

The flow cell experiments investigating the influence of solids content on attachment using the 57 nm particles exhibit a relatively uniform attachment profile along the direction of flow, or x-direction. Along the y-direction, more particle attachment occurs close to the channel walls compared to that of the center of the flow channel. The graphical results of these experiments are presented in Figure 5.35 and the spatial distribution of attached particles is presented in Figure 5.36. The increase in solids content results in a corresponding increase in the number of particles attached, in agreement with expectation. Such an observation is in contrast with the results of the 510 nm and 210 nm particle experiments where an obvious drop in attachment is observed when solids content is as high as 0.005%. This could be due to relatively less significant effects particle (aqueous) - particle (attached) interactions due to the much smaller particle size. The smaller particle size leads to much weaker repulsive interaction energy making it more difficult to mobilize the attached particles. Doubling the solids content from 0.0025% to 0.005% only results in a roughly 50% increase in particle attachment, however, indicating that particle (aqueous) - particle (attached) interactions may still be occurring to a less dominant extent compared to that of the larger particles.

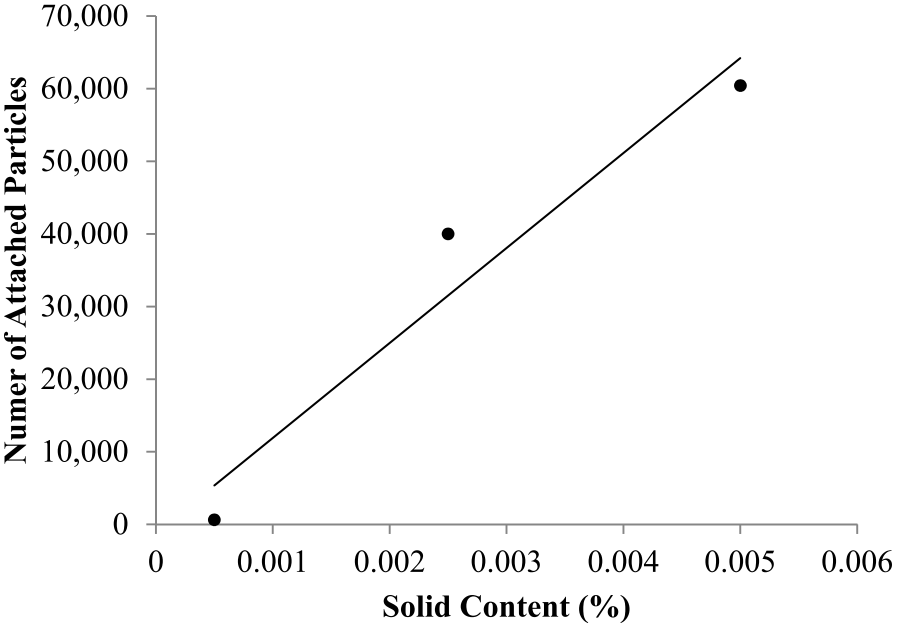

Figure 5.35 Influence of solids content on attachment using 57 nm particles

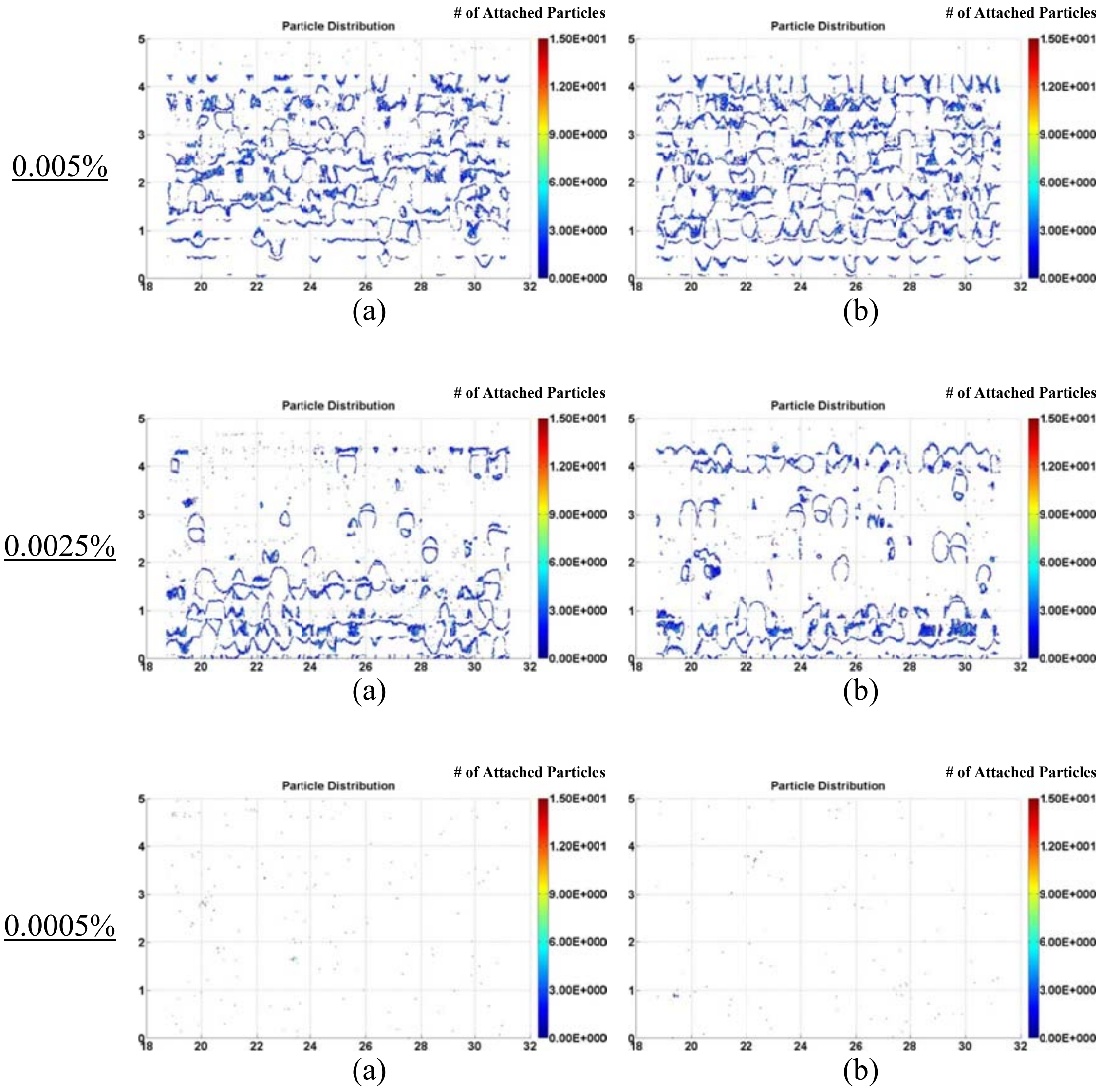

Figure 5.36 Spatial distributions of attached particles for flow cell experiments investigating the influence of solids content using 57 nm particles

Chapter 6

Conclusions

6.1 Overview

The primary focus of this study was to develop a method for using Laser Scanning Cytometry to investigate the transport of nano-scale particles in porous media. The purpose was to develop a repeatable approach in which the stable attachment of particles in a glass bead packed flow cell could be visualized, recorded and quantified in order to provide qualitative data and spatial distributions of attachment. From these results, the expectation was that direct insight into the fundamental mechanism governing the transport of nano-scale particles in porous media would be provided.

The first phase involved determining the feasibility of using fluorescent particles as small as 57 nm in conjunction with an LSC. After compatibly was verified, a method was developed to prepare and characterize particle suspensions, a flow system was designed and an experimental protocol was developed for flow cell experiments using an LSC. The second phase required an approach for taking the LSC data and converting it to quantifiable results, including spatial distributions of attached particles. From these results, direct observations were made regarding the influence of particle size, injection duration, solution chemistry, Darcy velocity and solids content on attachment. Further, observations and hypotheses were made concerning the mechanisms influencing the transport of the particles.

6.2 General Conclusions

1. An experimental protocol for using Laser Scanning Cytometry to investigate the transport of nano-scale particles in glass bead porous media was developed. This technique allows for both visualization and quantification of attachment. From the results, observations about the influence of particle size, injection duration, solution chemistry, Darcy velocity and solids content on attachment can be made. More importantly, direct insight into the fundamental mechanisms governing transport is provided.
2. The results of zeta potential measurements confirm that each of the three size particles are very close in zeta potential at each of the solution chemistries investigated; therefore, investigation into the influence of particle size on attachment is possible. More importantly, the range of particle sizes and corresponding zeta potentials are in the same range of reported sizes and zeta potentials as common engineered nanoparticle aggregates [35, 36]. This allows for the assumption that the behavior of the particles used in this study is representative of the behavior of common engineered nanomaterials.
3. The number of attached particles was found to decrease with decreasing particle size. Such an observation is in contradiction with classic filtration theory, but consistent with the column-scale study by Pelley and Tufenkji [28]. More effort was devoted to compare the behaviors of the three different size particles under varied injection duration, solution chemistry, solids content and Darcy velocity.

4. The increase in injection duration for the 510 nm particles indicates a likely S_{max}. Blocking effects were observed for the 57 nm particles in which attached particles block the available attachment sites and slow down the attachment of subsequent incoming particles. The spatial distributions of attached particles for these experiments also indicate more attachment occurs in the center regions of the flow channel with increasing injection duration.
5. Secondary minimum attachment plays a minor role for the attachment of both the 510 nm and 57 nm particles. Only about 10% of the attachment can be attributed to secondary minimum attachment, consistent with column-scale studies [21]. Further, the contribution of the secondary minimum is independent of particle size over the range of particle sizes investigated.
6. Change of Darcy velocity does not have profound influence on the attachment of the 57 nm particles. The seemingly flat trend for the influence of Darcy velocity for the 57 nm particles indicates that their transport is dominated by diffusion. Diffusion control can be further confirmed by the spatial distributions of attachment particles which show many 57 nm particles attached on downstream areas of the glass beads. Experiments on the influences of Darcy velocity on the attachment of 510 nm and 210 nm particles, however, did not provide definitive conclusions because the LSC scans did not cover the areas adjacent to the flow cell inlet. This is area is believed to be particularly critical to 510 nm and 210 nm particles with higher attachment capacity.

7. Investigations of initial solids content revealed the importance of particle (aqueous) - particle (attached) interactions. For 510 nm and 210 nm particles, there exists a critical initial solids content above which the number of attached particles will decrease with increasing initial solids content, consistent with previous column-scale studies [39]. This trend does not occur for the 57 nm particles. They exhibit increasing attachment with increasing solids content due to much weaker repulsive interaction energy for smaller size particles.

6.3 Future Recommendations

1. In several of the spatial distributions of attached particles there appears to be regions of reduced attachment occurring along the flow channel walls; however, less attachment is unexpected in these areas compared to that of the center of the flow channel. What appears to be minimal attachment occurring could actually be a result of the LSC threshold contour failing to distinguish an event due to the area being oversaturated with fluorescence. This oversaturation results in the intensity never dipping low enough for a threshold contour to occur and to account for the particles attached in these regions. Initially, it was believed that keeping the LSC parameters consistent for each experiment was important so as to not influence the results. After much consideration, it is now believed that the LSC parameters should be optimized for each individual experiment. Over time, the behavior of the fluorescent particles is inconsistent and the fluorescence can certainly change as it ages. Further, the fluorescence is designed, and excitation and emission

spectra developed for it, before it is applied to a particle suspension. It was discovered that the excitation and emission spectra are not exactly representative of how the fluorescently dyed particles will scan, because the behavior of the fluorescence can be slightly altered once it is introduced to the particle suspension. It is not reasonable to believe that each batch of particle suspension purchased will exhibit the same response to the LSC parameters.

2. The most important parameter the LSC operator needs to consider is the threshold contour. The value for the threshold contour determines how events will be recorded. Depending on the background noise and intensity value of areas where no attachment occurs, the threshold contour should be very carefully defined in order to maximize the number of particles accounted for during each LSC scan.
3. This study did not definitively define where the microscope was focused; rather, the microscope was focused at the top of the single layer of glass beads. The glass bead diameters vary over a small range, so it is not possible to get every single one of the beads into perfect focus. Future studies should consider developing a method to measure exactly where the microscope is focused within the flow channel in regards to the vertical dimension. This may allow several scans to be performed and combined from which a third spatial dimension can be introduced to the analysis.

References

1. U.S. Environmental Protection Agency (2007). "Nanotechnology White Paper." Washington, DC: 100/B-07/001.
2. Lux Research (2009). "Nanomaterials." Retrieved at http://www.luxresearchinc.com/.
3. Woodrow Wilson International Center for Scholars (2011). "Nanotech-enabled Consumer Products Continue to Rise." Available at http://www.nanotechproject.org/news/archive/9231/.
4. Woodrow Wilson International Center for Scholars (2009). "An inventory of nanotechnology-based consumer products currently on the market." Available at http://www.nanotechproject.org/inventories/consumer/.
5. Benn, T. M., and P. Westerhoff (2008). "Nanoparticle silver released into water from commercially available sock fabrics." *Environmental Science & Technology* 42 (11): 4133-4139.
6. Geranio, L., Heuberger, M., and B. Nowack (2009). "The Behavior of Silver Nanotextiles during Washing." *Environmental Science & Technology* 43 (21): 8113-8118.
7. Benn, T., Cavanagh, B., Hristovski, K., Posner, J. D., and P. Westerhoff (2010). "The Release of Nanosilver from Consumer Products Used in the Home." *Journal of Environmental Quality* 39 (6): 1875-1882.
8. Kaegi, R., Ulrich, A., Sinnet, B., Vonbank, R., Wichser, A., Zuleeg, S., Simmler, H., Brunner, S., Vonmont, H., Burkhardt, M., and M. Boller (2008). "Synthetic TiO2 nanoparticle emission from exterior facades into the aquatic environment." *Environmental Pollution* 156 (2): 233-239.

9. Klaine, S. J., Alvarez, P. J. J., Batley, G. E., Fernandes, T. F., Handy, R. D., Lyon, D. Y., Mahendra, S., McLaughlin, M. J., and J. R. Lead (2008). "Nanomaterials in the environment: Behavior, fate, bioavailability, and effects." *Environmental Toxicology and Chemistry* 27 (9): 1825-1851.
10. Zhang, W., Yao, Y., Sullivan, N., and Y. S. Chen (2011). "Modelling the Primary Size Effects of Citrate-Coated Silver Nanoparticles on Their Ion Release Kinetics." *Environmental Science & Technology* 45 (10): 4422-4428.
11. Friends of the Earth (2009). "Nano & Biocidal Silver." Available at http://www.foe.org/sites/default/files/Nano-silverReport_US.pdf.
12. Future Markets, Inc., (2011). "The World Market For Nanoparticle Titanium Dioxide (TiO2)." Pub ID: FTMK6327962.
13. Long, T. C., Saleh, N., Tilton, R. D., Lowry, G. V., and B. Veronesi (2006). "Titanium dioxide (P25) produces reactive oxygen species in immortalized brain microglia (BV2): Implications for nanoparticle neurotoxicity." *Environmental Science & Technology* 40 (14): 4346-4352.
14. Bermudez, E., Mangum, J. B., Wong, B. A., Asgharian, B., Hext, P. M., Warheit, D. B., and J. I. Everitt (2004). "Pulmonary responses of mice, rats, and hamsters to subchronic inhalation of ultrafine titanium dioxide particles." *Toxicological Sciences* 77 (2): 347-357.
15. Wang, J. J. a., Sanderson, B. J. S. b., and H. a. Wang (2007). "Cyto- and genotoxicity of ultrafine TiO2 particles in cultured human lymphoblastoid cells." *Mutation Research – Genetic Toxicology and Environmental Mutagenesis* 628 (2): 99-106.

16. Reeves, J. F., Davies, S. J., Dodd, N. J. F., and A. N. Jha (2007) “Hydroxyl radicals (OH) are associated with titanium dioxide (TiO2) nanoparticle-induced cytotoxicity and oxidative DNA damage in fish cells.” *Mutation Research/Fundamental and Molecular Mechanisms of Mutagenesis* 640 (1-2): 113-122.

17. Zhang, Y., Chen, Y. S., Westerhoff, P., Hristovski, K., and J. C. Crittenden (2008). “Stability of commercial metal oxide nanoparticles in water.” *Water Research* 42 (8-9): 2204-2212.

18. Yao, K. M., Habibian, M. T., and C. R. O’Melia (1971). “Water and Waste Water Filtration: Concepts and Applications.” *Environmental Science & Technology* 5 (11): 1105-1112.

19. Auset, M., and A. A. Keller (2006). “Pore-scale visualization of colloid straining and filtration in saturated porous media using micromodels.” *Water Resources Research* 42, W12S02, doi: 10.1029/2005WR004639.

20. Elimelech, M., Gregory, J., Jia, X., and R. A. Williams (1995). “Particle Deposition and Aggregation: Measurement, Modelling and Simulation.” Woburn, MA: Butterworth-Heinemann, 448.

21. Li, Y., Wang, Y., Pennell, K. D., and L. M. Abriola (2008). “Investigation of the Transport and Deposition of Fullerene (C60) Nanoparticles in Quartz Sands under Varying Flow Conditions.” *Environmental Science & Technology* 42 (19): 7174-7180.

22. Espinasse, B., Hotze, E. M., and M. R. Wiesner (2007). “Transport and Retention of Colloidal Aggregates of C60 in Porous Media: Effects of Organic Macromolecules,

Ionic Composition, and Preparation Method." *Environmental Science & Technology* 41 (21): 7396-7402.

23. Hyung, H., and J.-H. Kim (2008). "Natural Organic Matter (NOM) Adsorption to Multi-Walled Carbon Nanotubes: Effect of NOM Characteristics and Water Quality Parameters." *Environmental Science & Technology* 42 (12): 4416-4421.
24. Jaisi, D. P., and M. Elimelech (2009). "Single-Walled Carbon Nanotubes Exhibit Limited Transport in Soil Columns." *Environmental Science & Technology* 43 (24): 9161-9166.
25. Liu, X., O'Carroll, D. M., Petersen, E. J., Huang, Q., and C. L. Anderson (2009). "Mobility of Multiwalled Carbon Nanotubes in Porous Media." *Environmental Science & Technology* 43 (21): 8153-8158.
26. Jaisi, D. P., Saleh, N. B., Blake, R. E., and M. Elimelech (2008). "Transport of Single-Walled Carbon Nanotubes in Porous Media: Filtration Mechanisms and Reversibility." *Environmental Science & Technology* 42 (22): 8317-8323.
27. Wang, Y., Yusong, Li., Fortner, J. D., Hughes, J. B., Abriola, L. M., and K. D. Pennell (2008). Transport and Retention of Nanoscale C_{60} Aggregates in Water-Saturated Porous Media." *Environmental Science & Technology* 42 (10): 3588-3594.
28. Pelley, A.J., and N. Tufenkji (2008). "Effect of particle size and natural organic matter on the migration of nano- and microscale latex particles in saturated porous media." *Journal of Colloid and Interface Science* 321 (1): 74-83.
29. Kuznar, Z. A., and M. Elimelech (2007). "Direct microscope observation of particle deposition in porous media: Role of secondary energy minimum." *Physicochem. Eng. Aspects* 294: 156-162.

30. Guzman, K. A. D., Finnegan, M. P., and J. F. Banfield (2006). “Influence of Surface Potential on Aggregation and Transport of Titania Nanoparticles.” *Environmental Science & Technology* 40 (24): 7688-7693.
31. Kamentsky, L. A., Burger, D. E., Gerschman, R. J., Kamentsky, L. D., and E. Luther (1997). Slide-based laser scanning cytometry. *Acta Cytologica* 41: 123-143.
32. Darzynkiewicz, Z., Bedner, E., Li, X., Gorczyca, W., and M. R. Melamed (1999). “Laser-Scanning Cytometry: A New Instrumentation with Many Applications.” *Experimental Cell Research* 249, 1-12.
33. CompuCyte (2011). “Laser Scanning Cytometry.” *LSC Technology Brochure*. Retrieved at http://www.compucyte.com/.
34. Petosa, A. R., Jaisi, D. P., Quevedo, I. R., Elimelech, M., and N. Tufenkji (2010). “Aggregation and Deposition of Engineered Nanomaterials in Aquatic Environments: Role of Physiochemical Interactions.” *Environmental Science and Technology* 44 (17): 6532-6549.
35. Duncan, L. K., Jinschek, J. R., and P. J. Vikesland (2008). “C_{60} Colloid Formation in Aqueous Systems: Effects of Preparation Method on Size, Structure, and Surface Charge.” *Environmental Science & Technology* 42 (1): 173-178.
36. Brant, J., Lecoanet, H., and M. R. Wiesner (2005). “Aggregation and deposition characteristics of fullerene nanoparticles in aqueous systems.” *Journal of Nanoparticle Research* 7 (4-5): 545-553
37. Elimelech, M., and C. R. Omelia (1990). “Effect of particle size on collision efficiency in the deposition of Brownian particles with electrostatic energy barriers.” *Langmuir* 6 (6): 1153-1163.

38. Litton, G.M., and T.M. Olson (1996). “Particle size effects on colloid deposition kinetics: Evidence of secondary minimum deposition.” *Colloids and Surfaces A: Physicochem. Eng. Aspects* 107: 273-283.
39. Bradford, S.C., and M. Bettahar (2006). “Concentration dependent transport of colloids in saturated porous media.” *Journal of Contaminant Hydrology* 82: 99-117.

Appendix A. Experimental Data

Table A.1 Raw data for flow cell experiments using 510 nm particles

MEAN DIAMETER: 510 nm

Exp. #	**001a**	**001b**	**002a**	**002b**	**003a**	**003b**	**004a**	**004b**	**005a**	**005b**	**006a**	**006b**	**031a**	**033a**	**036a**	**037a**
% solids	0.0025	0.0025	0.0025	0.0025	0.0025	0.0025	0.0025	0.0025	0.005	0.005	0.0005	0.0005	0.0025	0.0025	0.0025	0.0025
mM NaCl	3	3	3	3	3	3	3	3	3	3	3	3	3	3	3	100
cm/s	0.08	0.08	0.06	0.06	0.04	0.04	0.02	0.02	0.04	0.04	0.04	0.04	0.08	0.04	0.04	0.04
Susp. pH	6.851	6.851	6.851	6.851	6.856	6.856	6.924	6.924	6.849	6.849	6.925	6.925	6.893	6.972	6.854	6.933
Back. pH	6.864	6.864	6.864	6.864	6.857	6.857	6.995	6.995	6.965	6.965	6.965	6.965	6.876	6.876	6.863	6.804
Empty (g)	4.003	4.046	4.073	4.047	4.003	4.047	4.004	4.047	4.003	4.073	4.047	4.047	4.040	4.038	4.075	3.996
Packed (g)	4.262	4.308	4.317	4.297	4.273	4.295	4.272	4.292	4.252	4.329	4.307	4.304	4.299	4.301	4.360	4.278
PV (mL)	0.096	0.094	0.102	0.099	0.091	0.100	0.092	0.101	0.100	0.096	0.095	0.096	0.095	0.094	0.085	0.086
ε	0.478	0.472	0.508	0.494	0.455	0.499	0.458	0.505	0.498	0.482	0.475	0.479	0.477	0.469	0.423	0.431
mL/min	0.192	0.192	0.144	0.144	0.096	0.096	0.048	0.048	0.096	0.096	0.096	0.096	0.192	0.096	0.096	0.096
Susp. (mL)	3.822	3.777	4.068	3.953	3.640	3.995	3.664	4.037	3.984	3.859	3.803	3.835	11.442	11.253	20.315	3.447
Back. (mL)	2.162	2.151	2.224	2.195	2.116	2.205	2.123	2.216	2.203	2.171	2.157	2.165	2.160	2.144	2.053	2.068

Table A.2 Raw data for flow cell experiments using 210 nm particles

MEAN DIAMETER: 210 nm

Exp. #	**011a**	**011b**	**012a**	**012b**	**013a**	**013b**	**014a**	**014b**	**015a**	**015b**	**016a**	**016b**
% solids	0.0025	0.0025	0.0025	0.0025	0.0025	0.0025	0.0025	0.0025	0.005	0.005	0.0005	0.0005
mM NaCl	3	3	3	3	3	3	3	3	3	3	3	3
cm/s	0.08	0.08	0.06	0.06	0.04	0.04	0.02	0.02	0.04	0.04	0.04	0.04
Empty (g)	4.034	4.034	4.038	4.034	4.034	4.038	4.034	4.034	4.034	4.034	4.034	4.034
Packed (g)	4.305	4.312	4.287	4.299	4.316	4.318	4.313	4.312	4.300	4.311	4.297	4.300
PV (mL)	0.091	0.088	0.099	0.093	0.086	0.087	0.087	0.088	0.093	0.088	0.094	0.093
ε	0.453	0.439	0.496	0.465	0.432	0.434	0.437	0.438	0.463	0.441	0.469	0.464
mL/min	0.192	0.192	0.144	0.144	0.096	0.096	0.048	0.048	0.096	0.096	0.096	0.096
Susp. (mL)	3.622	3.512	3.969	3.717	3.454	3.472	3.496	3.505	3.706	3.530	3.751	3.709
Back. (mL)	2.112	2.085	2.199	2.136	2.070	2.074	2.081	2.083	2.133	2.089	2.144	2.134

Table A.3 Raw data for flow cell experiments using 57 nm particles

MEAN DIAMETER: 57 nm

Exp. #	**021a**	**021b**	**022a**	**022b**	**023a**	**023b**	**024a**	**024b**	**025a**	**025b**	**026a**	**026b**	**032a**	**034a**	**035a**
% solids	0.0025	0.0025	0.0025	0.0025	0.0025	0.0025	0.0025	0.0025	0.005	0.005	0.0005	0.0005	0.0025	0.0025	0.0025
mM NaCl	3	3	3	3	3	3	3	3	3	3	3	3	3	100	3
cm/s	0.08	0.08	0.06	0.06	0.04	0.04	0.02	0.02	0.04	0.04	0.04	0.04	0.08	0.04	0.08
Susp. pH	7.032	7.032	7.032	6.989	7.032	6.989	6.989	6.989	6.886	6.886	7.006	7.006	6.937	6.875	6.881
Back. pH	6.876	6.876	6.876	6.876	6.876	6.876	6.876	6.876	6.876	6.876	6.863	6.863	6.876	6.956	6.863
Empty (g)	4.050	4.075	4.065	4.050	4.043	4.043	4.065	4.043	4.065	4.043	4.065	4.075	4.043	4.065	4.065
Packed (g)	4.318	4.337	4.350	4.318	4.318	4.310	4.325	4.311	4.333	4.325	4.354	4.362	4.315	4.334	4.352
PV (mL)	0.092	0.094	0.085	0.092	0.089	0.092	0.095	0.092	0.092	0.086	0.083	0.084	0.090	0.091	0.084
ε	0.460	0.471	0.424	0.459	0.444	0.460	0.475	0.458	0.459	0.431	0.416	0.419	0.450	0.457	0.422
mL/min	0.192	0.192	0.144	0.144	0.096	0.096	0.048	0.048	0.096	0.096	0.096	0.096	0.192	0.096	0.192
Susp. (mL)	3.683	3.764	3.396	3.670	3.554	3.678	3.798	3.667	3.670	3.446	3.329	3.354	10.802	3.659	25.321
Back. (mL)	2.127	2.148	2.055	2.124	2.095	2.126	2.156	2.123	2.124	2.068	2.039	2.045	2.107	2.121	2.051